

Error correcting Bacon-Shor code with continuous measurement of noncommuting operators

Juan Atalaya,¹ Alexander N. Korotkov,^{2,3} and K. Birgitta Whaley¹

¹*Department of Chemistry, University of California, Berkeley, CA 94720, USA*

²*Google Inc., 340 Main Street, Venice, CA 90291, USA*

³*Department of Electrical and Computer Engineering,
University of California, Riverside, CA 92521, USA*

(Dated: August 25, 2020)

We analyze the continuous operation of the nine-qubit error correcting Bacon-Shor code with all noncommuting gauge operators measured at the same time. The error syndromes are continuously monitored using cross-correlations of sets of three measurement signals. We calculate the logical error rates due to X , Y and Z errors in the physical qubits and compare the continuous implementation with the discrete operation of the code. We find that both modes of operation exhibit similar performances when the measurement strength from continuous measurements is sufficiently strong. We also estimate the value of the crossover error rate of the physical qubits, below which continuous error correction gives smaller logical error rates. Continuous operation has the advantage of passive monitoring of errors and avoids the need for additional circuits involving ancilla qubits.

I. INTRODUCTION

Quantum error correction (QEC) is one of the most active research areas in the quantum computing field. Fault-tolerant quantum computing [1–6] features QEC as an essential ingredient to enable robust computation in noisy environments and to further achieve the system size scalability that is necessary to show the quantum advantage over classical algorithms. Significant experimental efforts have been devoted to implement quantum error correcting codes in current quantum computer hardwares [7–16]. In particular, surface codes [17–20] have recently drawn considerable attention because of their comparatively high noise threshold, while Bacon-Shor codes [21–23] have attracted study both on account of a favorable noise threshold [22] and because, regardless of the code distance, they only require measurement of two-qubit operators on neighboring qubits [24].

Continuous QEC has been theoretically investigated for a long time [25–35]. Recent work in this direction has focused on schemes in which the error syndrome operators of a QEC code that is defined for discrete error and recovery operations are monitored in real time using continuous quantum measurements [36–45] instead of the projective measurements that are used in conventional QEC. Most previous works have focused on the continuous operation of stabilizer quantum error correcting codes, where the measured operators commute with each other [3]. In contrast, continuous operation of subsystem codes such as the Bacon-Shor codes is a relatively unexplored subject [46]. Analysis of subsystem codes is complicated by the fact that the measured operators do not commute. Renewed interest in continuous QEC has been triggered by the rapid experimental progress in continuous quantum measurement in the context of circuit QED setups [47–54] together with the realization of quantum feedback technologies [55, 56] with superconducting qubits. These therefore constitute a promising testbed

for implementation of continuous QEC.

In this work we theoretically analyze the continuous operation of the nine-qubit Bacon-Shor code, which is the smallest quantum error correcting code from the family of Bacon-Shor codes [21, 57]. We extend here the previous work of two of us on the continuous operation of the four-qubit Bacon-Shor code [46], which is the smallest error detecting code from such family of codes.

The nine-qubit Bacon-Shor code encodes one logical qubit into nine physical qubits, which are conveniently arranged in a square lattice as shown in Fig. 1 (a). The error syndrome is defined in terms of the values of four stabilizer generators: $Z_1Z_4Z_2Z_5Z_3Z_6$, $Z_4Z_7Z_5Z_8Z_6Z_9$, $X_1X_2X_4X_5X_7X_8$ and $X_2X_3X_5X_6X_8X_9$. However, instead of directly measuring such multi-qubit Pauli operators, their values are obtained from the measurement of twelve noncommuting two-qubit operators (the so-called gauge operators): Z_1Z_4 , Z_2Z_5 , Z_3Z_6 , Z_4Z_7 , Z_5Z_8 , Z_6Z_9 , X_1X_2 , X_4X_5 , X_7X_8 , X_2X_3 , X_5X_6 and X_8X_9 . In the conventional operation, the gauge operators are projectively measured in two sequential steps—see Fig. 1 (b), since they do not commute. The values of the stabilizer generators and hence the error syndromes are then obtained from the product of three discrete measurement outcomes (e.g., the value of $Z_1Z_4Z_2Z_5Z_3Z_6$ is obtained from the product of outcomes ± 1 of Z_1Z_4 , Z_2Z_5 and Z_3Z_6). The value of the error syndrome determines the specific error correcting operation C_{op} that ought to be applied to a physical qubit at the end of each operation cycle.

The main question we address in this paper is how to achieve continuous operation of the nine-qubit Bacon-Shor code, where all noncommuting gauge operators are continuously measured at the same time. The quantum backaction induced by such noncommuting measurements makes the nine-qubit state evolve diffusively in the 512-dimensional Hilbert space. A useful description is achieved by parameterizing the nine-qubit state in terms of probability amplitudes of one logical qubit

and four effective qubits that we refer to as the gauge qubits [19]. In this description, state diffusion of the full state can be seen as state diffusion of the gauge qubits due to simultaneous continuous measurement of twelve (effective) noncommuting operators. The gauge qubits dynamics plays an important role in the error analysis of the continuous operation of the nine-qubit Bacon-Shor code [46]. A related measurement-induced state evolution has been theoretically studied in Refs. [58–60] and recently observed in Ref. [52] for a single qubit subject to simultaneous continuous measurement of the noncommuting observables σ_x and σ_z .

In our continuous QEC protocol, stabilizer generators are monitored in real time using time-averaged cross-correlators of three measurement signals (e.g., $Z_1Z_4Z_2Z_5Z_3Z_6$ is continuously monitored via the triple correlator of the measurement signals from continuous measurement of Z_1Z_4 , Z_2Z_5 and Z_3Z_6). Time averaging is necessary because the measurement signals are noisy and their product is even noisier [61]. In our protocol, active correction of errors is only performed at the end of the continuous operation and no realizations are discarded. In the presence of errors, the system state jumps from the code space to one of the error subspaces, or between error subspaces. This evolution over multiple subspaces is characterized by the *error syndrome path*, which is shown to uniquely determine the errors, modulo the action of gauge operators. This error syndrome path is the central object in our continuous QEC protocol, see Fig. 1 (c). We track this path using a simple two-error-threshold algorithm applied to the time-averaged cross-correlators. The path monitoring is, however, not perfect, since the cross-correlators are noisy and require time averaging, which slows down their response to errors. The discrepancy between the actual and the monitored error syndrome paths leads to finite logical error rates, which we calculate both analytically and numerically. We also find the optimal values of the four parameters for this continuous QEC protocol, namely two integration time parameters and two error threshold parameters.

Our main conclusion is that continuous operation of the nine-qubit Bacon-Shor code is indeed possible and that its performance can be comparable to that of the conventional QEC approach of discrete, projective measurements onto ancillas, followed by discrete state recovery operations at each operation cycle. The main advantage of the continuous operation is the passive monitoring of errors, with consequent avoidance of ancilla circuits. We also determine the crossover value of the physical qubit error rate below which the error rate of the corrected logical qubit is smaller than that of the physical qubits.

The remainder of the paper is organized as follows. In Section II, we briefly discuss the conventional operation of the nine-qubit Bacon-Shor code; we introduce the orthonormal bases for the code space and the error subspaces and derive formulas for the logical error rates that

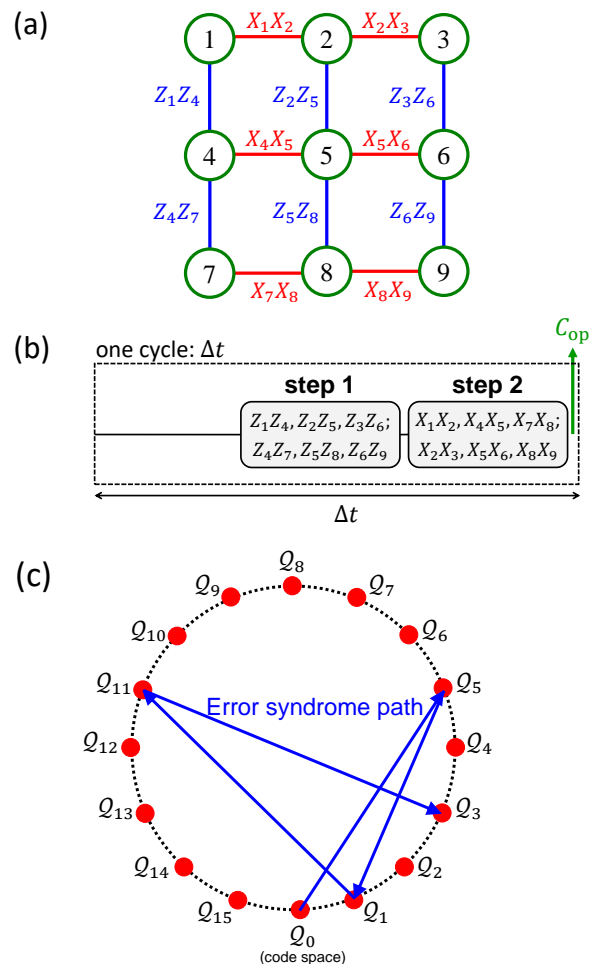


FIG. 1. (a) The nine-qubit Bacon-Shor code. The code operation is based on measurement of 12 gauge operators: Z_1Z_4 , Z_2Z_5 , Z_3Z_6 , Z_4Z_7 , Z_5Z_8 , Z_6Z_9 , X_1X_2 , X_4X_5 , X_7X_8 , X_2X_3 , X_5X_6 and X_8X_9 . Circles in this panel indicate the physical qubits. Panel (b) shows the conventional (discrete) operation of the code where the gauge operators are projectively measured in two steps. The cycle ends with the application of a discrete (instantaneous) error correcting operation C_{op} that depends on the error syndrome—see Table I. Cycle duration is Δt . Panel (c) shows the error syndrome path. Arrows indicate state transitions between subspaces (Q_ℓ) due to errors.

are later used to compare the conventional and continuous implementations. In Section III, we derive our main results for the continuous operation. We introduce the idea of the gauge and logical qubits in the code space and error subspaces. We present a continuous quantum measurement model for the evolution of the gauge qubits and discuss how to account for decoherence. We then present our continuous QEC protocol, which is based on continuous monitoring of the error syndrome path, and calculate the logical error rates for this protocol. In Section IV, we find the optimal parameters of the continuous QEC protocol, estimate the crossover error rate for the physical qubits, and compare the performances of the continuous and conventional operations. Section V presents a discussion and conclusions.

II. NINE-QUBIT BACON-SHOR CODE WITH PROJECTIVE MEASUREMENTS

A. System, code space, and discrete QEC protocol

The nine-qubit Bacon-Shor code encodes one logical qubit into nine physical qubits, labeled 1–9 in Fig. 1 (a). The conventional discrete operation of the code is based on projective measurement of two-qubit operators, which are referred to as gauge operators and are indicated in Fig. 1 (a) by the vertical and horizontal edges. These gauge operators are denoted by

$$\begin{aligned} Z_1 Z_4 &= Z_{14} = G_1, & Z_4 Z_7 &= Z_{47} = G_4, \\ Z_2 Z_5 &= Z_{25} = G_2, & Z_5 Z_8 &= Z_{58} = G_5, \\ Z_3 Z_6 &= Z_{36} = G_3, & Z_6 Z_9 &= Z_{69} = G_6, \end{aligned} \quad (1a)$$

and

$$\begin{aligned} X_1 X_2 &= X_{12} = G_7, & X_2 X_3 &= X_{23} = G_{10}, \\ X_4 X_5 &= X_{45} = G_8, & X_5 X_6 &= X_{56} = G_{11}, \\ X_7 X_8 &= X_{78} = G_9, & X_8 X_9 &= X_{89} = G_{12}, \end{aligned} \quad (1b)$$

where Z_j and X_j are Pauli operators that act on the j th physical qubit. For example, $Z_1 = \sigma_z \otimes \mathbb{1}_{256}$, $X_1 = \sigma_x \otimes \mathbb{1}_{256}$, etc., $\sigma_z = |0\rangle\langle 0| - |1\rangle\langle 1|$ and $\sigma_x = |0\rangle\langle 1| + |1\rangle\langle 0|$ are the conventional Pauli matrices, and $\mathbb{1}_{256}$ is the 256×256 identity matrix. The two-qubit operators (1a) and (1b) are referred to as the Z - and X -gauge operators, respectively. Since such groups of gauge operators do not commute with each other, they are sequentially measured in steps 1 and 2 respectively, using projective measurements—see Fig. 1 (b). The projective measurements are assumed to be instantaneous. A discrete (instantaneous) error correcting operation C_{op} (including

the identity if no error is detected) is then applied to a specific physical qubit whose identity is determined by the joint values of all step-1 and step-2 measurement outcomes, which are ± 1 since the gauge operators are Pauli operators.

The group generated by all gauge operators G_k has an Abelian subgroup, referred to as the ‘stabilizer’, with four generators that commute with each other:

$$\begin{aligned} S_z^{(1)} &= Z_{14} Z_{25} Z_{36} = G_1 G_2 G_3, \\ S_z^{(2)} &= Z_{47} Z_{58} Z_{69} = G_4 G_5 G_6, \\ S_x^{(1)} &= X_{12} X_{45} X_{78} = G_7 G_8 G_9, \\ S_x^{(2)} &= X_{23} X_{56} X_{89} = G_{10} G_{11} G_{12}, \end{aligned} \quad (2)$$

This property allows us to divide the full Hilbert space into 16 32-dimensional eigenspaces in which the stabilizer generators have definite values. The values of $S_x^{(1)}$, $S_z^{(1)}$, $S_x^{(2)}$ and $S_z^{(2)}$ determine the error syndrome pattern in each of these eigenspaces, as summarized in Table I. We shall employ this ordering throughout the remainder of the paper. As usual, the eigenspace where all stabilizer generator eigenvalues are $+1$ is referred to as the code space, which is denoted by \mathcal{Q}_0 . In the code space the product of the outcomes of $\{Z_{14}, Z_{25}, Z_{36}\}$ is $+1$, and the same holds for the product of the outcomes of $\{Z_{47}, Z_{58}, Z_{69}\}$, $\{X_{12}, X_{45}, X_{78}\}$, and $\{X_{23}, X_{56}, X_{89}\}$. If at least one of these products is -1 , the system state is in one of the other 15 eigenspaces that are referred to as the error subspaces and are denoted by \mathcal{Q}_ℓ with $\ell = 1$ to 15. Note that all gauge operators commute with the stabilizer generators, so step-1 and step-2 measurements do not change the error syndrome pattern.

We now introduce the following orthonormal basis for the 32-dimensional code space \mathcal{Q}_0 :

$$\begin{aligned} |\phi_1\rangle &= (|000\ 000\ 000\rangle + |110\ 110\ 110\rangle + |101\ 101\ 101\rangle + |011\ 011\ 011\rangle) / 2, \\ |\phi_2\rangle &= (|000\ 000\ 011\rangle + |110\ 110\ 101\rangle + |101\ 101\ 110\rangle + |011\ 011\ 000\rangle) / 2, \\ |\phi_3\rangle &= (|000\ 000\ 110\rangle + |110\ 110\ 000\rangle + |101\ 101\ 011\rangle + |011\ 011\ 101\rangle) / 2, \\ |\phi_4\rangle &= (|000\ 000\ 101\rangle + |110\ 110\ 011\rangle + |101\ 101\ 000\rangle + |011\ 011\ 110\rangle) / 2, \\ |\phi_5\rangle &= (|000\ 011\ 011\rangle + |110\ 101\ 101\rangle + |101\ 110\ 110\rangle + |011\ 000\ 000\rangle) / 2, \\ |\phi_6\rangle &= (|000\ 011\ 000\rangle + |110\ 101\ 110\rangle + |101\ 110\ 101\rangle + |011\ 000\ 011\rangle) / 2, \\ |\phi_7\rangle &= (|000\ 011\ 101\rangle + |110\ 101\ 011\rangle + |101\ 110\ 000\rangle + |011\ 000\ 110\rangle) / 2, \\ |\phi_8\rangle &= (|000\ 011\ 110\rangle + |110\ 101\ 000\rangle + |101\ 110\ 011\rangle + |011\ 000\ 101\rangle) / 2, \\ |\phi_9\rangle &= (|000\ 110\ 110\rangle + |110\ 000\ 000\rangle + |101\ 011\ 011\rangle + |011\ 101\ 101\rangle) / 2, \\ |\phi_{10}\rangle &= (|000\ 110\ 101\rangle + |110\ 000\ 011\rangle + |101\ 011\ 000\rangle + |011\ 101\ 110\rangle) / 2, \\ |\phi_{11}\rangle &= (|000\ 110\ 000\rangle + |110\ 000\ 110\rangle + |101\ 011\ 101\rangle + |011\ 101\ 011\rangle) / 2, \\ |\phi_{12}\rangle &= (|000\ 110\ 011\rangle + |110\ 000\ 101\rangle + |101\ 011\ 110\rangle + |011\ 101\ 000\rangle) / 2, \\ |\phi_{13}\rangle &= (|000\ 101\ 101\rangle + |110\ 011\ 011\rangle + |101\ 000\ 000\rangle + |011\ 110\ 110\rangle) / 2, \\ |\phi_{14}\rangle &= (|000\ 101\ 110\rangle + |110\ 011\ 000\rangle + |101\ 000\ 011\rangle + |011\ 110\ 101\rangle) / 2, \\ |\phi_{15}\rangle &= (|000\ 101\ 011\rangle + |110\ 011\ 101\rangle + |101\ 000\ 110\rangle + |011\ 110\ 000\rangle) / 2, \\ |\phi_{16}\rangle &= (|000\ 101\ 000\rangle + |110\ 011\ 110\rangle + |101\ 000\ 101\rangle + |011\ 110\ 011\rangle) / 2, \\ |\phi_{16+j}\rangle &= X_1 X_2 X_3 X_4 X_5 X_6 X_7 X_8 X_9 |\phi_j\rangle, \quad j = 1, 2, \dots, 16. \end{aligned} \quad (3)$$

It is straightforward to check that each of the nine-qubit states (3) is an eigenstate of all four stabilizer generators with eigenvalue +1. The procedure to obtain the states in the computational basis as written above is described in Appendix A. As we shall see below, analysis of the logical errors in the continuous operation is most conveniently performed in terms of the evolution of the system wavefunction due to errors and the continuous measurements. Therefore we need to specify a particular basis for the code and error subspaces.

An orthonormal basis for each error subspace can be constructed from the orthonormal basis vectors $|\phi_j\rangle$ of the code space. However, this construction is not unique. For instance, let us consider the orthonormal basis for \mathcal{Q}_1 , where the error syndrome values are $S_x^{(1)} = S_z^{(1)} = S_x^{(2)} = 1$ and $S_z^{(2)} = -1$ (see Table I). Indeed, we can choose orthonormal basis vectors for \mathcal{Q}_1 either as $X_7|\phi_j\rangle$ or $X_8|\phi_j\rangle$ or $X_9|\phi_j\rangle$ (with $j = 1$ to 32), since X_7, X_8 or X_9 anticommute with $S_z^{(2)}$ and commute with the other stabilizer generators. The reason for this freedom is that these orthonormal bases are equivalent modulo a gauge operator or product of gauge operators. For example, the orthonormal basis vectors $X_7|\phi_j\rangle$ and $X_8|\phi_j\rangle$ are equivalent modulo $G_9 = X_7X_8$. We will choose $Q_1|\phi_j\rangle$ with $Q_1 = X_9$ as the orthonormal basis vectors for the error subspace \mathcal{Q}_1 . There is also similar freedom in choosing the orthonormal basis for the other error subspaces. Our choice for the orthonormal bases used in this work for the error subspaces is specified in Table I. The ordering of the error syndrome in this table is not binary but set by the Pauli operators ($Q_\ell = X_9, Y_9, Z_9, X_1, X_9X_1$, etc.) that define the orthonormal basis vectors of subspaces \mathcal{Q}_ℓ .

The nine-qubit state is initially prepared in the code space at the beginning of the code operation. Then step-1 and step-2 measurements will not kick the state out of the code space and, in the absence of decoherence, the state will always remain in the code space. In this ideal situation, the measurement outcomes for $\{Z_{47}, Z_{58}, Z_{69}\}$ can be $\{+1, +1, +1\}$, $\{+1, -1, -1\}$, $\{-1, +1, -1\}$ or $\{-1, -1, +1\}$ (note that the product of the three numbers in each group is +1), and the same “good” outcomes can also be obtained for measurement of $\{Z_{14}, Z_{25}, Z_{36}\}$. There are thus $4 \times 4 = 16$ “good” outcome configurations for step-1 measurements. The same outcomes ($\{+1, +1, +1\}$, $\{+1, -1, -1\}$, $\{-1, +1, -1\}$, $\{-1, -1, +1\}$) can also be obtained for measurements of X_{12}, X_{45} and X_{78} as well as for X_{23}, X_{56} and X_{89} , so there are also 16 “good” outcome configurations for step-2 measurements.

If some of the values of the stabilizer generators are -1 , the conventional QEC protocol dictates that we apply an error correcting operation C_{op} at the end of the cycle [see Fig. 1 (b)]; the specific C_{op} depends on the error syndrome as indicated in Table I. After applying C_{op} , the system state is returned to the code space; however, the logical state can be degraded if several errors happen within a cycle (as discussed in Section II C).

TABLE I. Error syndrome, orthonormal basis vectors and error correcting operations for the error subspaces $\mathcal{Q}_{\ell \neq 0}$ (code space is denoted by \mathcal{Q}_0). The error syndrome is defined as the values of the stabilizer generators $S_x^{(1)}, S_z^{(1)}, S_x^{(2)}$ and $S_z^{(2)}$ (in this order) and the orthonormal basis vectors in the error subspaces are obtained by applying operators Q_ℓ to the basis vectors $|\phi_j\rangle$ of the code space, given in Eq. (3). $Q_0 = \mathbb{1}$.

sub-space	error syndrome				basis vectors $Q_\ell \phi_j\rangle$	error correcting operation (C_{op})
	$S_x^{(1)}$	$S_z^{(1)}$	$S_x^{(2)}$	$S_z^{(2)}$		
\mathcal{Q}_0	+1	+1	+1	+1	$ \phi_j\rangle$	$\mathbb{1}$ (identity)
\mathcal{Q}_1	+1	+1	+1	-1	$X_9 \phi_j\rangle$	X_7, X_8 or X_9
\mathcal{Q}_2	+1	+1	-1	-1	$Y_9 \phi_j\rangle$	Y_9
\mathcal{Q}_3	+1	+1	-1	+1	$Z_9 \phi_j\rangle$	Z_3, Z_6 or Z_9
\mathcal{Q}_4	+1	-1	+1	+1	$X_1 \phi_j\rangle$	X_1, X_2 or X_3
\mathcal{Q}_5	+1	-1	+1	-1	$X_9X_1 \phi_j\rangle$	X_4, X_5 or X_6
\mathcal{Q}_6	+1	-1	-1	-1	$Y_9X_1 \phi_j\rangle$	Y_6
\mathcal{Q}_7	+1	-1	-1	+1	$Z_9X_1 \phi_j\rangle$	Y_3
\mathcal{Q}_8	-1	-1	+1	+1	$Y_1 \phi_j\rangle$	Y_1
\mathcal{Q}_9	-1	-1	+1	-1	$X_9Y_1 \phi_j\rangle$	Y_4
\mathcal{Q}_{10}	-1	-1	-1	-1	$Y_9Y_1 \phi_j\rangle$	Y_5
\mathcal{Q}_{11}	-1	-1	-1	+1	$Z_9Y_1 \phi_j\rangle$	Y_2
\mathcal{Q}_{12}	-1	+1	+1	+1	$Z_1 \phi_j\rangle$	Z_1, Z_4 or Z_7
\mathcal{Q}_{13}	-1	+1	+1	-1	$X_9Z_1 \phi_j\rangle$	Y_7
\mathcal{Q}_{14}	-1	+1	-1	-1	$Y_9Z_1 \phi_j\rangle$	Y_8
\mathcal{Q}_{15}	-1	+1	-1	+1	$Z_9Z_1 \phi_j\rangle$	Z_2, Z_5 or Z_8

B. Operation without errors

In the absence of errors, step-1 measurements collapse the state to one of the following states (for simplicity of notation, we write step-1 measurement results ± 1 as \pm)

$$\begin{aligned}
|Z + + +, + + +\rangle &= \alpha|\phi_1\rangle + \beta|\phi_{17}\rangle, \\
|Z + + +, + - -\rangle &= \alpha|\phi_2\rangle + \beta|\phi_{18}\rangle, \\
|Z + + +, - - +\rangle &= \alpha|\phi_3\rangle + \beta|\phi_{19}\rangle, \\
|Z + + +, - + -\rangle &= \alpha|\phi_4\rangle + \beta|\phi_{20}\rangle, \\
|Z + - -, + + +\rangle &= \alpha|\phi_5\rangle + \beta|\phi_{21}\rangle, \\
|Z + - -, + - -\rangle &= \alpha|\phi_6\rangle + \beta|\phi_{22}\rangle, \\
|Z + - -, - - +\rangle &= \alpha|\phi_7\rangle + \beta|\phi_{23}\rangle, \\
|Z + - -, - + -\rangle &= \alpha|\phi_8\rangle + \beta|\phi_{24}\rangle, \\
|Z - - +, + + +\rangle &= \alpha|\phi_9\rangle + \beta|\phi_{25}\rangle, \\
|Z - - +, + - -\rangle &= \alpha|\phi_{10}\rangle + \beta|\phi_{26}\rangle, \\
|Z - - +, - - +\rangle &= \alpha|\phi_{11}\rangle + \beta|\phi_{27}\rangle, \\
|Z - - +, - + -\rangle &= \alpha|\phi_{12}\rangle + \beta|\phi_{28}\rangle, \\
|Z - + -, + + +\rangle &= \alpha|\phi_{13}\rangle + \beta|\phi_{29}\rangle, \\
|Z - + -, + - -\rangle &= \alpha|\phi_{14}\rangle + \beta|\phi_{30}\rangle, \\
|Z - + -, - - +\rangle &= \alpha|\phi_{15}\rangle + \beta|\phi_{31}\rangle, \\
|Z - + -, - + -\rangle &= \alpha|\phi_{16}\rangle + \beta|\phi_{32}\rangle, \tag{4}
\end{aligned}$$

where $|Z g_1g_2g_3, g_4g_5g_6\rangle$ denotes the nominal step-1 collapse state that corresponds to the “good” out-

come configuration g_1, g_2, \dots, g_6 for the Z -gauge operators G_1, \dots, G_6 , respectively. Each of these collapse states are parametrized by the complex-valued variables α and β that represent the probability amplitudes to be in the zero ($|0_L\rangle$) or one ($|1_L\rangle$) logical states, respectively. The state of the *logical qubit* is defined as

$$|\Psi_L\rangle = \alpha |0_L\rangle + \beta |1_L\rangle. \quad (5)$$

Similarly, step-2 measurements collapse the state to one of 16 possible states that are denoted by $|X g_7 g_8 g_9, g_{10} g_{11} g_{12}\rangle$ (with g_7, g_8, \dots, g_{12} being also a “good” outcome configuration). These nominal step-2 collapse states can be expressed as a linear combination of all 16 nominal step-1 collapse states of Eq. (4) (and *vice versa*) with coefficients $\pm 1/4$, so $|X g_7 g_8 g_9, g_{10} g_{11} g_{12}\rangle$ is parametrized by the same logical state (α, β) . Thus, the logical state is immune to measurement of the gauge operators. The probability that any of the nominal step-2 collapse states occurs after step-1 measurements is $1/16$. In the absence of errors, no error correction is needed so $C_{\text{op}} = \mathbb{1}$. Then, step-1 measurements of the next cycle collapse the state $|X g_7 g_8 g_9, g_{10} g_{11} g_{12}\rangle$ to any of the states of Eq. (4) with probability $1/16$, and so on. The real unitary matrix that relates the nominal step-1 and step-2 collapse states is given in Appendix A.

Since we focus here on the performance of the nine-qubit Bacon-Shor code against errors, we may assume that the encoding step (i.e., preparation of an initial wavefunction such as $|Z+++ , +++\rangle$ with a given logical state α, β) is perfect. At the end of the code operation there is also a decoding step to obtain the logical state from the code space; this decoding step is also assumed to be perfect.

The gauge qubits. A general nine-qubit state $|\Psi_{Q_0}\rangle$ in the code space can be written as

$$\begin{aligned} |\Psi_{Q_0}\rangle = & c_{0000} |Z+++ , +++\rangle + c_{0001} |Z+++ , +--\rangle \\ & + c_{0010} |Z+++ , --+\rangle + c_{0011} |Z+++ , -+-\rangle \\ & + c_{0100} |Z+-- , +++\rangle + c_{0101} |Z+-- , +--\rangle \\ & + c_{0110} |Z+-- , --+\rangle + c_{0111} |Z+-- , -+-\rangle \\ & + c_{1000} |Z--- , +++\rangle + c_{1001} |Z--- , +--\rangle \\ & + c_{1010} |Z--- , --+\rangle + c_{1011} |Z--- , -+-\rangle \\ & + c_{1100} |Z-+- , +++\rangle + c_{1101} |Z-+- , +--\rangle \\ & + c_{1110} |Z-+- , --+\rangle + c_{1111} |Z-+- , -+-\rangle, \quad (6) \end{aligned}$$

where the 16 coefficients $c_{q_1 q_2 q_3 q_4}$ ($q_j = \{0, 1\}$) together describe the state of *four gauge qubits*. The conventional operation of the nine-qubit Bacon-Shor code is characterized by the *discrete evolution* of the gauge qubits due to projective measurement of the gauge operators. Indeed, after step-1 measurements (Z -gauge operators), only one of the coefficients $c_{q_1 q_2 q_3 q_4}$ is 1 and all others are 0, while after step-2 measurements (X -gauge operators), all coefficients are non-zero and equal to $\pm 1/4$. However, the logical state (α, β) is not affected by the measurements.

In continuous operation of the code, this discrete evolution of the gauge qubits state is replaced

by diffusive evolution as we describe in Section III below.

C. Operation with errors

While environmental decoherence in physical qubit systems is typically a gradual process, we can model it as the average effect of discrete (instantaneous) X , Y and Z errors that occur at random times on the nine physical qubits. This is the jump/no-jump method [5, 62] that we use to describe decoherence—see Section IID for a brief description of this method and how it is used to calculate the logical error rates.

In contrast to errors on physical qubits, logical X , Y and Z errors are operations on the logical state (α, β) that are defined as

$$\begin{aligned} X_L(\alpha, \beta) &= (\beta, \alpha), \quad Z_L(\alpha, \beta) = (\alpha, -\beta), \\ Y_L(\alpha, \beta) &= i(\beta, -\alpha). \quad (7) \end{aligned}$$

Logical errors can only come from two or more physical errors happening in a faulty cycle, since all single-qubit errors are fully correctable after application of the error correcting operation C_{op} (the nine-qubit Bacon-Shor code is a full single-qubit quantum error correcting code [19, 21, 22].) For sufficiently small occurrence rate of errors, logical errors are mainly due to two physical qubit errors; three errors are much less probable, and higher order errors are increasingly less likely. We thus focus on two-qubit errors. In this section we shall also assume that errors occur at the same time. This assumption is allowed if we are only interested in changes of the logical state due to Pauli-type errors with trivial no-jump evolution. We also assume no errors occur between the measurement steps.

Two-qubit errors can be of two types. *Harmless* two-qubit errors are those that leave the logical qubit state (α, β) unperturbed after a faulty cycle, although the state of the computationally unimportant gauge qubits is usually affected. Examples of harmless two-qubit errors are the gauge operators. In contrast, *harmful* two-qubit errors are those that together with C_{op} create a logical error (the state of gauge qubits is usually also affected in this case.) That is, the two-qubit error combination E_1 and E_2 is harmful if

$$E_1 E_2 C_{\text{op}} \sim X_L, Y_L \text{ or } Z_L, \quad (8)$$

where “ \sim ” indicates equivalence modulo gauge operators. In Appendix B we explain how to obtain all the harmful two-qubit error combinations that are listed below in Eqs. (9)–(11).

1. Logical X errors

There are 90 harmful two-qubit errors that lead to a logical X error after a faulty cycle. We list these below:

$$\begin{aligned}
\mathcal{Q}_1 &: X_1X_4, X_1X_5, X_1X_6, X_2X_4, X_2X_5, X_2X_6, X_3X_4, X_3X_5, X_3X_6, Y_3Y_6, Y_1Y_4, Y_2Y_5, \\
\mathcal{Q}_2 &: X_1Y_6, X_2Y_6, X_3Y_6, X_4Y_3, X_5Y_3, X_6Y_3, \\
\mathcal{Q}_4 &: X_7X_4, X_7X_5, X_7X_6, X_8X_4, X_8X_5, X_8X_6, X_9X_4, X_9X_5, X_9X_6, Y_6Y_9, Y_4Y_7, Y_5Y_8, \\
\mathcal{Q}_5 &: X_1X_7, X_1X_8, X_1X_9, X_2X_7, X_2X_8, X_2X_9, X_3X_7, X_3X_8, X_3X_9, Y_3Y_9, Y_1Y_7, Y_2Y_8, \\
\mathcal{Q}_6 &: X_7Y_3, X_8Y_3, X_9Y_3, X_1Y_9, X_2Y_9, X_3Y_9, \\
\mathcal{Q}_7 &: X_7Y_6, X_8Y_6, X_9Y_6, X_4Y_9, X_5Y_9, X_6Y_9, \\
\mathcal{Q}_8 &: X_7Y_4, X_8Y_4, X_9Y_4, X_4Y_7, X_5Y_7, X_6Y_7, \\
\mathcal{Q}_9 &: X_7Y_1, X_8Y_1, X_9Y_1, X_1Y_7, X_2Y_7, X_3Y_7, \\
\mathcal{Q}_{10} &: X_7Y_2, X_8Y_2, X_9Y_2, X_1Y_8, X_2Y_8, X_3Y_8, \\
\mathcal{Q}_{11} &: X_7Y_5, X_8Y_5, X_9Y_5, X_4Y_8, X_5Y_8, X_6Y_8, \\
\mathcal{Q}_{13} &: X_1Y_4, X_2Y_4, X_3Y_4, X_4Y_1, X_5Y_1, X_6Y_1, \\
\mathcal{Q}_{14} &: X_1Y_5, X_2Y_5, X_3Y_5, X_4Y_2, X_5Y_2, X_6Y_2.
\end{aligned} \tag{9}$$

The top line in Eq. (9) shows the two-qubit errors that map code space states $|\Psi_{\mathcal{Q}_0}\rangle$ [see Eq. (6)] to the error subspace \mathcal{Q}_1 (before applying C_{op}), and the remaining lines show two-qubit errors that map $|\Psi_{\mathcal{Q}_0}\rangle$ to the error subspaces $\mathcal{Q}_2, \mathcal{Q}_4, \mathcal{Q}_5, \mathcal{Q}_6, \mathcal{Q}_7, \mathcal{Q}_8, \mathcal{Q}_9, \mathcal{Q}_{10}, \mathcal{Q}_{11}, \mathcal{Q}_{13}$ and \mathcal{Q}_{14} , respectively. (Note absence of harmful two-error combinations corresponding to subspaces $\mathcal{Q}_0, \mathcal{Q}_3, \mathcal{Q}_{12}$ and \mathcal{Q}_{15} .) Establishing which subspaces are reached after two-qubit errors is important, since it allows one to determine the appropriate error correcting operation C_{op} from Table I. After application of the appropriate C_{op} , the system state is returned to the code space. However, in all these cases the logical state suffers from a logical X error (i.e., α and β are exchanged). Note that there are no $X_iZ_{i'}$ combinations in the list (9), since these are equivalent to Y errors (modulo gauge operators), which are correctable and thus harmless, in our categorization. The combinations $Z_iZ_{i'}$ and $Z_iY_{i'}$ can only lead to logical Z errors, see below.

2. Logical Z errors

There are also 90 harmful two-qubit errors that lead to a logical Z error after a faulty cycle. These can be obtained from list (9) by applying exchange of $X \leftrightarrow Z$, as well as exchange of the qubit indices $2 \leftrightarrow 4, 3 \leftrightarrow 7$ and $6 \leftrightarrow 8$. We note that these exchanges are possible because of the symmetry properties of the nine-qubit Bacon-Shor code, specifically, the $X - Z$ symmetry and the square symmetry of the qubit layout (i.e., reflexion in the main diagonal of square of Fig. 1-(a)).

Logical Z error: list (9) with exchanges $X \leftrightarrow Z$,

$$2 \leftrightarrow 4, 3 \leftrightarrow 7 \text{ and } 6 \leftrightarrow 8. \tag{10}$$

The error combinations of the lines of list (9) with the changes indicated in Eq. (10) now provide the two-qubit errors that map $|\Psi_{\mathcal{Q}_0}\rangle$ to the error subspaces $\mathcal{Q}_3, \mathcal{Q}_2, \mathcal{Q}_{12}, \mathcal{Q}_{15}, \mathcal{Q}_{14}, \mathcal{Q}_{13}, \mathcal{Q}_8, \mathcal{Q}_{11}, \mathcal{Q}_{10}, \mathcal{Q}_9, \mathcal{Q}_7$, and \mathcal{Q}_6 , respectively.

3. Logical Y errors

We list below the 18 harmful two-qubit errors that lead to a logical Y error after a faulty cycle:

$$\begin{aligned}
\mathcal{Q}_2 &: Y_1Y_5, Y_2Y_4, \\
\mathcal{Q}_6 &: Y_1Y_8, Y_2Y_7, \\
\mathcal{Q}_7 &: Y_4Y_8, Y_5Y_7, \\
\mathcal{Q}_8 &: Y_5Y_9, Y_6Y_8, \\
\mathcal{Q}_9 &: Y_2Y_9, Y_3Y_8, \\
\mathcal{Q}_{10} &: Y_1Y_9, Y_3Y_7, \\
\mathcal{Q}_{11} &: Y_4Y_9, Y_6Y_7, \\
\mathcal{Q}_{13} &: Y_2Y_6, Y_3Y_5, \\
\mathcal{Q}_{14} &: Y_1Y_6, Y_3Y_4.
\end{aligned} \tag{11}$$

The lines of list (11) show the two-qubit errors that map $|\Psi_{\mathcal{Q}_0}\rangle$ to the error subspaces $\mathcal{Q}_2, \mathcal{Q}_6, \mathcal{Q}_7, \mathcal{Q}_8, \mathcal{Q}_9, \mathcal{Q}_{10}, \mathcal{Q}_{11}, \mathcal{Q}_{13}$ and \mathcal{Q}_{14} , respectively.

D. Logical error rates

We now calculate the logical error rates for the nine-qubit Bacon-Shor code operating under projective measurements.

We assume that the nine qubits are subject to 27 uncorrelated Markovian errors of X, Y and Z type, with occurrence rates $\Gamma_i^{(X)}, \Gamma_i^{(Y)}, \Gamma_i^{(Z)}$, respectively, where the index i denotes the physical qubit. We also assume that $\Gamma_i^{(X,Y,Z)}\Delta t \ll 1$, so that single-qubit errors are the most probable, followed by two-qubit errors, three-qubit errors, etc. The time duration for a full cycle of measurements is Δt —see Fig. 1 (b).

In the jump/no-jump method, the actual system evolution, which is characterized by a density matrix $\rho(t)$, is replaced by an ensemble of wavefunction trajectories $|\psi(t)\rangle$ that are conditional on the error-event realizations. The ensemble average of these trajectories $|\psi(t)\rangle\langle\psi(t)|$

produces the mixed state $\rho(t)$ that describes the actual decohering evolution, according to the standard Lindblad equation

$$\dot{\rho} = \sum_{i,E} \Gamma_i^{(E)} \mathcal{L}[E_i] \rho,$$

$$\mathcal{L}[A] \rho \equiv A \rho A^\dagger - \frac{1}{2} (A^\dagger A \rho + \rho A^\dagger A), \quad (12)$$

where E_i is the Kraus operator associated with error of type E acting on the i th qubit. At each infinitesimal timestep δt , the wavefunction $|\psi(t)\rangle$ can exhibit a jump that changes it to the value $|\psi(t + \delta t)\rangle = E_i |\psi(t)\rangle / \mathcal{N}_j$, where \mathcal{N}_j is a normalization factor (for Pauli errors $\mathcal{N}_j = 1$). The probability of a jump occurring in each δt is given by $(\Gamma_i^{(E)} \delta t) \langle \psi(t) | E_i^\dagger E_i | \psi(t) \rangle$. In the case of no jump, the wavefunction changes to $(\mathbb{1} - \sum_{i,E} E_i^\dagger E_i \delta t / 2) |\psi(t)\rangle / \mathcal{N}_{nj}$, with normalization factor \mathcal{N}_{nj} . In the particular case where the Kraus operators E_i are Pauli operators (i.e., $E_i^\dagger E_i = \mathbb{1}$), no-jump evolution is trivial (i.e., no evolution) while the jump probability is $\Gamma_i^{(E)} \delta t$, which is state-independent. In this paper we consider decoherence due to all possible single Pauli errors, i.e., X, Y or Z errors ($E_i = \{X_i, Y_i, Z_i\}$).

For a sufficiently small occurrence rate of errors, the probability of a logical error after M operation cycles is equal to $\sum_{\{E_i, E'_i\}} (T_{\text{op}} \Gamma_i^{(E)}) (\Gamma_i^{(E')} \Delta t)$, where $T_{\text{op}} = M \Delta t$ is the operation duration and the sum is over all harmful two-qubit errors $E_i E'_i$ [see Eqs. (9)–(11)] that lead to a logical X, Z or Y error. We then obtain the discrete-operation logical error rate γ_L^{disc} by dividing this probability by T_{op} ($L = X, Y$ or Z):

$$\gamma_L^{\text{disc}} = \sum_{\{E_i, E'_i\}} \Gamma_i^{(E)} \Gamma_i^{(E')} \Delta t. \quad (13)$$

Since we have in total 198 harmful two-qubit errors [Eqs. (9)–(11)], we shall for simplicity evaluate the logical error rate formula (13) for the depolarizing channel, for which all three Pauli error rates are equal:

$$\Gamma_i^{(X)} = \Gamma_i^{(Y)} = \Gamma_i^{(Z)} = \frac{\Gamma_d}{3}, \quad (14)$$

with Γ_d the depolarization error rate, which we assume to be the same for all qubits. Taking all of the error channels in Eqs. (9)–(11) into account, we find that the logical X, Z and Y error rates for the depolarizing channel are given by

$$\gamma_X^{\text{disc}} = \gamma_Z^{\text{disc}} = 10 \Gamma_d^2 \Delta t \quad \text{and} \quad \gamma_Y^{\text{disc}} = \frac{\gamma_X^{\text{disc}}}{5} = 2 \Gamma_d^2 \Delta t, \quad (15)$$

respectively. The total logical error rate is then equal to

$$\gamma_{\text{disc}} = \gamma_X^{\text{disc}} + \gamma_Y^{\text{disc}} + \gamma_Z^{\text{disc}} = 22 \Gamma_d^2 \Delta t. \quad (16)$$

The full formulae for the logical X, Y and Z error rates in the case of non-equivalent qubits and a general asymmetric error channel are given in Appendix C.

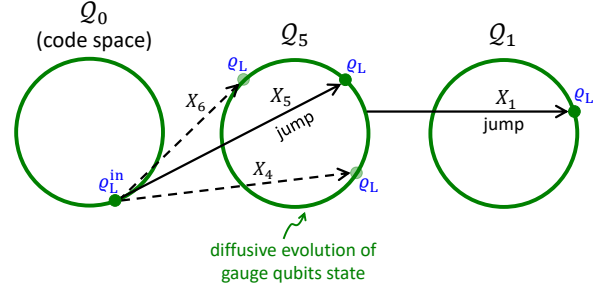


FIG. 2. Illustration of the state evolution due to continuous measurement and X_5 and X_1 errors. Green circles represent 16-dimensional spheres where diffusive evolution of the state of the four gauge qubits takes place. Before the first error (X_5) occurs, the gauge qubits diffusively evolve in the code space \mathcal{Q}_0 while the logical state, denoted by ϱ_L^{in} , is unaffected by the continuous measurement. Immediately after the first error occurs, the system state is in the error subspace \mathcal{Q}_5 with a new logical state ($\varrho_L = X_L \varrho_L^{\text{in}} X_L$) and a new state for the gauge qubits, symbolically indicated by the solid dot on the circle of \mathcal{Q}_5 . Note that the errors X_4 and X_6 are equivalent to X_5 up to X -gate operators so they map the system state to the same error subspace (\mathcal{Q}_5) with the same logical state (ϱ_L) but a different gauge qubits state; this is indicated by the dashed arrows pointing at different points on the circle of \mathcal{Q}_5 . During the time between the errors, there is diffusive evolution of the gauge qubits in \mathcal{Q}_5 due to measurement while the logical state is constant. The second error (X_1) makes the system state jump from \mathcal{Q}_5 to \mathcal{Q}_1 , and, according to Table II, this error does not affect the logical state nor the gauge qubits state, so the logical state in \mathcal{Q}_1 is also ϱ_L . The logical error in the code operation occurs if we misidentify two jumps $\mathcal{Q}_0 \rightarrow \mathcal{Q}_5 \rightarrow \mathcal{Q}_1$ with a single jump $\mathcal{Q}_0 \rightarrow \mathcal{Q}_1$.

III. NINE-QUBIT BACON-SHOR CODE WITH CONTINUOUS MEASUREMENTS

We now analyze the continuous operation of the nine-qubit Bacon-Shor code, in which the sequential projective measurements of gauge operators are replaced by simultaneous continuous quantum measurements. Before we present our model of the continuous quantum measurement, we first qualitatively discuss the evolution of the system state due to continuous measurement combined with physical qubit errors.

Continuous measurement of the noncommuting gauge operators changes the state of the gauge qubits in a diffusive fashion. This is characterized by the time evolution of the c -coefficients of Eq. (6) if the system state is in the code space, or, more generally, by the time evolution of the c -coefficients of Eq. (17) if the system state is in the subspace \mathcal{Q}_ℓ . A somewhat similar diffusive state evolution was discussed in Ref. [46], where continuous operation of the error detecting four-qubit Bacon-Shor code (with one logical qubit and one gauge qubit) was analyzed. It turns out that these c -coefficients can be regarded as real if they are initially set to real values.

We can then think of the measurement-induced diffusive evolution of the gauge qubits state as taking place on a 16-dimensional sphere (one for each subspace \mathcal{Q}_ℓ). These are represented in Fig. 2 by green circles; points on these circles denote different states of the gauge qubits and also carry a label (ϱ_L) that denotes the logical state, which is not affected by the continuous measurements. In our model, the diffusive state evolution of the gauge qubits will be given by a stochastic master equation that is described in the following subsection below.

Let us now consider the effect of errors. Errors cause jumps of the system state between two subspaces $\mathcal{Q}_{\ell_{\text{in}}}$ and \mathcal{Q}_ℓ . In general, the logical state is different immediately before the jump and immediately after the jump. The same holds for the state of the gauge qubits (any change of the logical state is not harmful as long as we know what this change is). Table II shows how errors affect the state of the logical and gauge qubits. In this Table we express all 27 possible errors as a product of three operations. For instance, the error X_5 is equivalent (up to a phase factor) to $Q_5 X_L X_{14}^g$, so this error changes the initial subspace (depending on the operator Q_5), also applies a logical X operation (α, β are exchanged), and also changes the c -coefficients as follows: $c_{q_1 q_2 q_3 q_4} \rightarrow X_4^g X_1^g c_{q_1 q_2 q_3 q_4}$, where X_j^g is an effective X operation on the j th gauge qubit—see Eq. (29). Table III provides the multiplication table for operators Q_ℓ that is necessary to find out which subspace the system state is mapped to after an error.

Tables II and III are then used to figure out to which subspace (\mathcal{Q}_ℓ) the system state jumps, after an error. For the example above, after the X_5 error, the system wavefunction can be spanned in the orthonormal basis $Q_\ell |\phi_j\rangle$ of the subspace \mathcal{Q}_ℓ , where the operator $Q_\ell = Q_5 \times Q_{\ell_{\text{in}}}$ is obtained from Table III and the operator $Q_{\ell_{\text{in}}}$ defines the orthonormal basis of the initial subspace $\mathcal{Q}_{\ell_{\text{in}}}$ (see

Table I). Assuming that the system state is initially in the code space (so that $Q_{\ell_{\text{in}}} = Q_0 = \mathbb{1}$ and $Q_\ell = Q_5$), the system state jumps from \mathcal{Q}_0 to \mathcal{Q}_5 , as illustrated in Fig. 2. (We point out that Q_ℓ operators play two roles in the continuous operation analysis, namely i) determination of transitions between subspaces due to errors, and ii) construction of basis transformations from the code space basis to the error subspace bases.) Note that, for Pauli-type errors, the no-jump evolution is trivial, so after a jump only the gauge qubits will evolve due to the measurement until the next jump, and so on. Note further that overall phase factors in the system wavefunction may be introduced by the errors; however, for Pauli-type errors we can disregard these, since phase factors affect neither the jump/no-jump probabilities nor the temporal correlations of the measurement signals. The c -coefficients can then be regarded as real even in the presence of errors. Figure 2 illustrates the effect of two errors X_5 and X_1 on a system state that is set initially in the code space (\mathcal{Q}_0).

A. Evolution due to measurement and errors

We first discuss the measurement-induced state dynamics in the code space and in the error subspaces, and then analyze the effect of errors using the jump/no-jump method. Analysis of the state dynamics in the error subspaces is important because our continuous QEC protocol does not correct errors at the moment when they are detected; instead, the correction is at the end of the code operation, as described in Section III B.

In both the code and error subspaces the system wavefunction can be parametrized as in Eq. (6). We rewrite this here as

$$\begin{aligned}
 |\Psi_{\mathcal{Q}_\ell}(t)\rangle = & c_{0000}(t) Q_\ell |Z+++ , +++\rangle + c_{0001}(t) Q_\ell |Z+++ , +- \rangle + c_{0010}(t) Q_\ell |Z+++ , - - \rangle + c_{0011}(t) Q_\ell |Z+++ , - + - \rangle + \\
 & c_{0100}(t) Q_\ell |Z+ - - , +++\rangle + c_{0101}(t) Q_\ell |Z+ - - , + - \rangle + c_{0110}(t) Q_\ell |Z+ - - , - - \rangle + c_{0111}(t) Q_\ell |Z+ - - , - + - \rangle + \\
 & c_{1000}(t) Q_\ell |Z- - + , +++\rangle + c_{1001}(t) Q_\ell |Z- - + , + - \rangle + c_{1010}(t) Q_\ell |Z- - + , - - \rangle + c_{1011}(t) Q_\ell |Z- - + , - + - \rangle + \\
 & c_{1100}(t) Q_\ell |Z- + - , +++\rangle + c_{1101}(t) Q_\ell |Z- + - , + - \rangle + c_{1110}(t) Q_\ell |Z- + - , - - \rangle + c_{1111}(t) Q_\ell |Z- + - , - + - \rangle, \quad (17)
 \end{aligned}$$

where the additional operator Q_ℓ now specifies that we are dealing with a wavefunction that belongs to the subspace \mathcal{Q}_ℓ —see Table I. The quantum backaction (see discussion below) from the simultaneous continuous measurement of the noncommuting gauge operators makes the coefficients $c_{q_1 q_2 q_3 q_4}(t)$ change in a diffusive fashion, while the logical state (α, β) that parametrizes $|Z \pm \pm \pm, \pm \pm \pm\rangle$ is unchanged by the continuous mea-

surements.

The 512×512 density matrix $\rho(t)$ that corresponds to the wavefunction Eq. (17) has only one nontrivial 32×32 diagonal submatrix $\varrho(t)$: this can be written in a direct-product form

$$\varrho(t) = \varrho_L \otimes \varrho_g(t) = \begin{pmatrix} |\alpha^2| \varrho_g(t) & \alpha \beta^* \varrho_g(t) \\ \alpha^* \beta \varrho_g(t) & |\beta^2| \varrho_g(t) \end{pmatrix}, \quad (18)$$

where ϱ_L represents the logical density matrix

$$\varrho_L = \begin{pmatrix} |\alpha^2| & \alpha\beta^* \\ \alpha^*\beta & |\beta^2| \end{pmatrix}, \quad (19)$$

and $\varrho_g(t)$ represents the 16×16 density matrix for the four gauge qubits, with matrix elements given by

$$\varrho_g(t)_{q_1 q_2 q_3 q_4, q'_1 q'_2 q'_3 q'_4} = c_{q_1 q_2 q_3 q_4}(t) c_{q'_1 q'_2 q'_3 q'_4}^*(t). \quad (20)$$

Since the gauge operators G_k do not cause transitions between the subspaces \mathcal{Q}_ℓ , they must have a block-diagonal matrix representation over these spaces. In the orthonormal basis of \mathcal{Q}_ℓ that is given in Table I, the 32×32 diagonal submatrices of G_k ($k = 1, 2, \dots, 12$) that correspond to the subspaces \mathcal{Q}_ℓ can be written as

$$[G_k]_{\mathcal{Q}_\ell} = \zeta_k^{(\ell)} \begin{pmatrix} \mathcal{G}_k & 0 \\ 0 & \mathcal{G}_k \end{pmatrix}, \quad (21)$$

where $\zeta_k^{(\ell)} = -1$ ($\zeta_k^{(\ell)} = 1$) if G_k anticommutes (commutes) with \mathcal{Q}_ℓ as given in Table I. In the code space we have $\zeta_k^{(0)} = 1$ for all k since $Q_0 = \mathbb{1}$. The 16×16 matrices \mathcal{G}_k in Eq. (21) read as

$$\begin{aligned} \mathcal{G}_1 &= Z_1^g, & \mathcal{G}_2 &= Z_{12}^g, & \mathcal{G}_3 &= Z_2^g, \\ \mathcal{G}_4 &= Z_3^g, & \mathcal{G}_5 &= Z_{34}^g, & \mathcal{G}_6 &= Z_4^g, \\ \mathcal{G}_7 &= X_1^g, & \mathcal{G}_8 &= X_{13}^g, & \mathcal{G}_9 &= X_3^g, \\ \mathcal{G}_{10} &= X_2^g, & \mathcal{G}_{11} &= X_{24}^g, & \mathcal{G}_{12} &= X_4^g, \end{aligned} \quad (22)$$

where Z_j^g and X_j^g respectively are the Z and X Pauli operators acting on the j th gauge qubit. Specifically, the action of Z_j^g and X_j^g on the c -coefficients is given below in Eqs. (29)–(30). Their matrix representations are $Z_1^g = \sigma_z \otimes \mathbb{1}_8$ ($\mathbb{1}_8$ is the 8×8 identity matrix), $X_1^g = \sigma_x \otimes \mathbb{1}_8$, etc. For simplicity of notation, we shall denote $Z_1^g Z_2^g = Z_{12}^g$, $X_1^g X_3^g = X_{13}^g$, etc.

The stochastic master equation that describes the measurement-induced evolution of the density matrix for the four gauge qubits, $\varrho_g(t)$, is given in Itô form [63] by [40, 58, 64]

$$\begin{aligned} \dot{\varrho}_g(t) &= \sum_k \left\{ \frac{\Gamma_k}{2} (\mathcal{G}_k \varrho_g \mathcal{G}_k - \varrho_g) + \frac{\xi_k(t)}{\sqrt{\tau_k}} \left(\frac{\mathcal{G}_k \varrho_g + \varrho_g \mathcal{G}_k}{2} \right. \right. \\ &\quad \left. \left. - \varrho_g \text{Tr}[\mathcal{G}_k \varrho_g] \right) \right\}, \end{aligned} \quad (23)$$

where Γ_k is the ensemble average dephasing rate due to measurement of G_k , and τ_k is the ‘‘measurement time’’ that is employed to distinguish between the two eigenvalues ± 1 of G_k . These two parameters are related through the quantum efficiency η_k of the k th detector as follows [45, 65]

$$\tau_k = \frac{1}{2\eta_k \Gamma_k}. \quad (24)$$

For ideal detectors $\eta_k = 1$, and for nonideal detectors $0 < \eta_k < 1$. In the Markovian approximation, the independent noises $\xi_k(t)$ in Eq. (23) are delta-correlated; their two-time correlation functions are

$$\langle \xi_k(t) \xi_{k'}(t') \rangle = \delta_{kk'} \delta(t - t'), \quad (25)$$

where $\langle \cdot \rangle$ indicates average over an ensemble of noise realizations. Equation (23) is valid for any subspace \mathcal{Q}_ℓ . The measurement signal from the k th detector is

$$I_{G_k}(t) = \zeta_k^{(\ell)} I_{\mathcal{G}_k}(t), \quad I_{\mathcal{G}_k}(t) = \text{Tr}[\mathcal{G}_k \varrho_g(t)] + \sqrt{\tau_k} \xi_k(t), \quad (26)$$

where $\zeta_k^{(\ell)} = \pm 1$ is the same sign factor that appears in Eq. (21).

Note that the evolution equation (23) keeps the gauge qubits density matrix $\varrho_g(t)$ real if it is initially set to a real density matrix at some earlier moment; this is so because the matrices (22) are real.

Equations (23) and (26) are not general. They are applicable only if i) the full density matrix $\rho(t)$ has support in only one of the subspaces \mathcal{Q}_ℓ , and ii) $\rho(t)$ can be written in a direct-product form that separates the logical and gauge degrees of freedom (this separation is referred to as the subsystem structure of subsystem codes.) If these conditions cannot be fulfilled, we have to use the evolution equation for full $\rho(t)$: this reads as (in Itô form)

$$\begin{aligned} \dot{\rho}(t) &= \\ &= \sum_k \frac{\Gamma_k}{2} (G_k \rho G_k - \rho) + \frac{\xi_k(t)}{\sqrt{\tau_k}} \left(\frac{G_k \rho + \rho G_k}{2} - \rho \text{Tr}[G_k \rho] \right), \end{aligned} \quad (27)$$

with the detector output signals given by

$$I_{G_k}(t) = \text{Tr}[\rho(t) G_k] + \sqrt{\tau_k} \xi_k(t). \quad (28)$$

Although Eqs. (27)–(28) hold for any physical density matrix $\rho(t)$, Eqs. (23) and (26) are more convenient for the analysis of the continuous operation of the nine-qubit Bacon-Shor code, because they allow us to effectively reduce the problem complexity from nine to four qubits. Note that the subsystem structure of $\rho(t)$ is preserved by Eq. (27) because of the block-diagonal form of G_k —see Eq. (21). We also point out that in deriving Eqs. (23) and (26) from Eqs. (27)–(28), we have used the trick of replacing $\xi_k(t)$ by $\zeta_k^{(\ell)} \xi_k(t)$ [46]. This is done to make Eq. (23) applicable to any subspace \mathcal{Q}_ℓ , and not only to the code space. A consequence of this trick is that $\zeta_k^{(\ell)} = \pm 1$ appears as an overall sign factor in the formulas for the actual measurement signals $I_{G_k}(t)$ in Eq. (26). In this way, we still preserve the sign of the temporal cross-correlations of $I_{G_k}(t)$, which is important to determine the error syndromes in the continuous operation, as described in Section III C.

Let us now discuss how errors X_i , Y_i and Z_i act on wavefunctions that are parametrized as in Eq. (17). Such

TABLE II. Equivalence relations for the 27 Pauli errors in terms of subspace-basis-transformation operators Q_ℓ , given in Table I, logical operations X_L , Y_L and Z_L , defined in Eq. (7), and gauge qubit operations X_j^g , Y_j^g and Z_j^g , defined in Eqs. (29)–(31). Phase factors are not included.

$X_1 \leftrightarrow Q_4$	$Z_1 \leftrightarrow Q_{12}$	$Y_1 \leftrightarrow Q_8$
$X_2 \leftrightarrow Q_4 X_1^g$	$Z_2 \leftrightarrow Q_{15} Z_L Z_{24}^g$	$Y_2 \leftrightarrow Q_{11} Z_L Z_{24}^g X_1^g$
$X_3 \leftrightarrow Q_4 X_{12}^g$	$Z_3 \leftrightarrow Q_3 Z_{24}^g$	$Y_3 \leftrightarrow Q_7 X_1^g Y_2^g Z_4^g$
$X_4 \leftrightarrow Q_5 X_L X_{34}^g$	$Z_4 \leftrightarrow Q_{12} Z_1^g$	$Y_4 \leftrightarrow Q_9 X_L X_{34}^g Z_1^g$
$X_5 \leftrightarrow Q_5 X_L X_{14}^g$	$Z_5 \leftrightarrow Q_{15} Z_L Z_{14}^g$	$Y_5 \leftrightarrow Q_{10} Y_L Y_{14}^g$
$X_6 \leftrightarrow Q_5 X_L X_{12}^g$	$Z_6 \leftrightarrow Q_3 Z_4^g$	$Y_6 \leftrightarrow Q_6 X_L X_{12}^g Z_4^g$
$X_7 \leftrightarrow Q_1 X_{34}^g$	$Z_7 \leftrightarrow Q_{12} Z_{13}^g$	$Y_7 \leftrightarrow Q_{13} X_4^g Y_3^g Z_1^g$
$X_8 \leftrightarrow Q_1 X_4^g$	$Z_8 \leftrightarrow Q_{15} Z_L Z_{13}^g$	$Y_8 \leftrightarrow Q_{14} Z_L X_4^g Z_{13}^g$
$X_9 \leftrightarrow Q_1$	$Z_9 \leftrightarrow Q_3$	$Y_9 \leftrightarrow Q_2$

errors preserve this parametrization and map the system state from subspace \mathcal{Q}_ℓ to one of the error subspaces $\mathcal{Q}_{\ell'}$. In addition, just as discussed above for the discrete operation, the errors can change the logical state (α, β) , the state of the gauge qubits (the c -coefficients $c_{q_1 q_2 q_3 q_4}$), and introduce an overall phase factor. As noted earlier, the latter is actually not important for Pauli-type errors, since no-jump evolution is trivial and the probability of jump is state-independent, so we may disregard overall phase factors in the wavefunctions. These phase factors are, however, important for other types of errors such as energy relaxation [46]. For reference, these factors are explicitly written in Appendix B.

Table II shows the representation of all 27 Pauli-type errors in terms of operators Q_ℓ , the logical operations X_L , Y_L and Z_L [defined in Eq. (7)] and gauge-qubit operations X_j^g , Y_j^g and Z_j^g . The latter perform the following linear transformations on the c -coefficients

$$\begin{aligned} X_1^g c_{q_1 q_2 q_3 q_4} &= c_{\bar{q}_1 q_2 q_3 q_4}, & X_2^g c_{q_1 q_2 q_3 q_4} &= c_{q_1 \bar{q}_2 q_3 q_4}, \\ X_3^g c_{q_1 q_2 q_3 q_4} &= c_{q_1 q_2 \bar{q}_3 q_4}, & X_4^g c_{q_1 q_2 q_3 q_4} &= c_{q_1 q_2 q_3 \bar{q}_4}, \end{aligned} \quad (29)$$

where $\bar{0} = 1$ and $\bar{1} = 0$, and

$$Z_j^g c_{q_1 q_2 q_3 q_4} = (-1)^{q_j} c_{q_1 q_2 q_3 q_4}, \quad (30)$$

$$Y_j^g c_{q_1 q_2 q_3 q_4} = \iota X_j^g Z_j^g c_{q_1 q_2 q_3 q_4}. \quad (31)$$

The imaginary phase factor ι in Eq. (31) is actually not necessary since we are dropping out phase factors.

We now have all the necessary elements to describe the dynamics of the code operation. At $t = 0$ there is an encoding step, after which the system state is initially set in the code space \mathcal{Q}_0 and parametrized according to Eq. (18), with some intended logical state ϱ_L^{in} [corresponding to Eq. (5)] and some arbitrary initial density matrix ϱ_g^{in} for the gauge qubits. Subsequently, simultaneous continuous measurement of the gauge operators induces diffusive evolution of $\varrho_g(t)$ according to Eq. (23), with initial condition $\varrho_g(0) = \varrho_g^{\text{in}}$ (see left green circle of Fig. 2), while the logical state remains constant.

TABLE III. Multiplication table for error-subspace basis operators Q_{ℓ_1} and Q_{ℓ_2} . The table is symmetric (i.e., $Q_{\ell_1} \times Q_{\ell_2} = Q_{\ell_2} \times Q_{\ell_1}$) if phase factors are disregarded (the table that includes phase factors is given in Appendix B.)

\times	Q_0	Q_1	Q_2	Q_3	Q_4	Q_5	Q_6	Q_7	Q_8	Q_9	Q_{10}	Q_{11}	Q_{12}	Q_{13}	Q_{14}	Q_{15}
Q_0	$\mathbb{1}$															
Q_1	Q_1	$\mathbb{1}$														
Q_2	Q_2	Q_3	$\mathbb{1}$													
Q_3	Q_3	Q_2	Q_1	$\mathbb{1}$												
Q_4	Q_4	Q_5	Q_6	Q_7	$\mathbb{1}$											
Q_5	Q_5	Q_4	Q_7	Q_6	Q_1	$\mathbb{1}$										
Q_6	Q_6	Q_7	Q_4	Q_5	Q_2	Q_3	$\mathbb{1}$									
Q_7	Q_7	Q_6	Q_5	Q_4	Q_3	Q_2	Q_1	$\mathbb{1}$								
Q_8	Q_8	Q_9	Q_{10}	Q_{11}	Q_{12}	Q_{13}	Q_{14}	Q_{15}	$\mathbb{1}$							
Q_9	Q_9	Q_8	Q_{11}	Q_{10}	Q_{13}	Q_{12}	Q_{15}	Q_{14}	Q_1	$\mathbb{1}$						
Q_{10}	Q_{10}	Q_{11}	Q_8	Q_9	Q_{14}	Q_{15}	Q_{12}	Q_{13}	Q_2	Q_3	$\mathbb{1}$					
Q_{11}	Q_{11}	Q_{10}	Q_9	Q_8	Q_{15}	Q_{14}	Q_{13}	Q_{12}	Q_3	Q_2	Q_1	$\mathbb{1}$				
Q_{12}	Q_{12}	Q_{13}	Q_{14}	Q_{15}	Q_8	Q_9	Q_{10}	Q_{11}	Q_4	Q_5	Q_6	Q_7	$\mathbb{1}$			
Q_{13}	Q_{13}	Q_{12}	Q_{15}	Q_{14}	Q_9	Q_8	Q_{11}	Q_{10}	Q_5	Q_4	Q_7	Q_6	Q_1	$\mathbb{1}$		
Q_{14}	Q_{14}	Q_{15}	Q_{12}	Q_{13}	Q_{10}	Q_{11}	Q_8	Q_9	Q_6	Q_7	Q_4	Q_5	Q_2	Q_3	$\mathbb{1}$	
Q_{15}	Q_{15}	Q_{14}	Q_{13}	Q_{12}	Q_{11}	Q_{10}	Q_9	Q_8	Q_7	Q_6	Q_5	Q_4	Q_3	Q_2	Q_1	$\mathbb{1}$

As an example, suppose the first error is X_5 (bit-flip in physical qubit 5) and occurs at the moment $t_{\text{err}}^{(1)}$. From Table II, we find that X_5 is equivalent to $Q_5 X_L X_{14}^g$. This means that immediately after this error the system state is in the error subspace \mathcal{Q}_5 , the logical state is $\varrho_L = X_L \varrho_L^{\text{in}} X_L$ (i.e., the logical state undergoes a logical X operation), and the state of the gauge qubits changes to $X_{14}^g \varrho_g(t_{\text{err}}^{(1)} - 0) X_{14}^g$, where we have explicitly displayed the elapsed time interval. We then again have diffusive evolution of $\varrho_g(t)$ according to Eq. (23) with new initial condition $\varrho_g(t_{\text{err}}^{(1)} + 0) = X_{14}^g \varrho_g(t_{\text{err}}^{(1)} - 0) X_{14}^g$, until the next error occurs. Suppose the second error is X_1 and occurs at moment $t_{\text{err}}^{(2)}$. From Table II, we see that X_1 is equivalent to Q_4 and affects neither the logical state nor the state of the gauge qubits. We use Table III to find out to which error subspace the system state jumps. From this table we see that $Q_4 \times Q_5 = Q_1$. This means that immediately after the second error, the system state is in the error subspace \mathcal{Q}_1 , while the state of the logical and gauge qubits are the same as before the occurrence of the X_1 error. Then we again have diffusion of the $\varrho_g(t)$ state but now in subspace \mathcal{Q}_1 until the next error occurs, and so on.

From this example, it is clear that the jump/no-jump method is an efficient method to describe decoherence due to Pauli-type errors in subsystem QEC codes, because it allows us to describe measurement-induced state diffusion using the reduced stochastic master equation Eq. (23) for $\varrho_g(t)$. It would be much more expensive computationally to solve the full evolution equation, Eq. (27). However, we point out that decoherence due to energy-relaxation (or any other non Pauli-type errors) requires the use of the full stochastic master equation [Eq. (27)].

The reason is that in this case the nontrivial no-jump evolution does not preserve the subsystem structure evident in Eqs. (17) or (18). Nevertheless, we can still use the jump/no-jump method to approximately calculate the logical error rates as undertaken in Ref. [46]. In this case, it is important to keep track of the overall phase factors that errors introduce to the wavefunctions. For this reason, in Appendix B, we present the modified versions of Tables II and III that include the phase factors.

For simplicity, from now on we shall assume that all detectors have the same measurement strength (symmetric case); i.e.,

$$\tau_k = \tau_m, \quad \Gamma_k = \Gamma_m, \quad \text{and} \quad \eta_k = \eta, \quad \forall k. \quad (32)$$

B. Continuous QEC protocol and the error syndrome path

In this section we discuss the QEC protocol that we use in the continuous operation of the nine-qubit Bacon-Shor code. The spirit of this protocol is somewhat similar to that of Mabuchi's QEC protocol for stabilizer codes [33], in the sense that we do not correct errors during the code operation, so the system state can explore all 16 subspaces \mathcal{Q}_ℓ in the presence of errors. However, in contrast to Ref. [33], we do not estimate the probability that the system state is in the subspaces \mathcal{Q}_ℓ during the code operation; instead, we monitor in real time the stabilizer generators $S_x^{(1)}, S_z^{(1)}, S_x^{(2)}$ and $S_z^{(2)}$, as explained below. The values of these in a given realization of our protocol determine what we refer to as the *error syndrome path*, denoted by $\mathcal{S}(t)$. The latter has values $\mathcal{S}(t) = \ell = 0, 1, \dots, 15$ depending on the error syndrome pattern at a given moment t —see Table I. For a given realization, $\mathcal{S}(t)$ is a piece-wise function of time. Knowledge of $\mathcal{S}(t)$ is sufficient to determine the logical state at the end of the code operation and to restore it before we return it to the user.

From the error syndrome path $\mathcal{S}(t)$ we can determine the (single-qubit) errors E_i that may have occurred, modulo gauge operators. Indeed, every time that $\mathcal{S}(t)$ jumps from, say, ℓ_1 to ℓ_2 , an error has occurred that causes the system state to jump from subspace \mathcal{Q}_{ℓ_1} to subspace \mathcal{Q}_{ℓ_2} . To figure out which errors E_i have caused this transition, we use Table III to find the Q_ℓ operator satisfying $Q_\ell \times Q_{\ell_1} = Q_{\ell_2}$, and then we use Table II to determine all errors E_i that are “proportional” to Q_ℓ . Although this procedure does not tell us the specific error that has actually happened (as noted above, it gives E_i modulo gauge operators), it does *uniquely* identify the logical operation (if any) that is induced by all the possible errors E_i . For instance, for $Q_\ell = Q_5$, Table II indicates that E_i could be X_3, X_4 or X_5 , which are all equivalent modulo X -gauge operators and which all introduce a logical X operation. The main idea of our continuous QEC algorithm is to continuously monitor $\mathcal{S}(t)$ as accurately as possible (see below), take note of all logical operations induced by the errors, and undo them at the end of the

code operation.

Let us denote the product of all inferred logical operations from the jumps of $\mathcal{S}(t)$ as \mathcal{O} (the total logical operation in a single realization of the continuous QEC protocol). For each realization, we can restore the logical state by applying the multi-qubit Pauli operations $X_1X_4X_7, Z_1Z_2Z_3$, or $X_1X_4X_7Z_1Z_2Z_3$ to the physical system if the total logical operation is $\mathcal{O} = X_L, Z_L$, or Y_L , respectively. Finally, we apply a decoding step to obtain the restored logical state from the final subspace, where the system state is at the end of each realization; this is the final logical state.

C. The monitored error syndrome path $\mathcal{S}_m(t)$

In this section we discuss how to monitor the error syndrome path in real time. To do this, we introduce the following triple cross-correlators

$$\mathcal{C}_z^{(1)}(t) = \int_0^t dt' \frac{e^{-\frac{t-t'}{T_c}}}{T_c} \mathcal{I}_{Z_{14}}(t') \mathcal{I}_{Z_{25}}(t') \mathcal{I}_{Z_{36}}(t'), \quad (33a)$$

$$\mathcal{C}_z^{(2)}(t) = \int_0^t dt' \frac{e^{-\frac{t-t'}{T_c}}}{T_c} \mathcal{I}_{Z_{47}}(t') \mathcal{I}_{Z_{58}}(t') \mathcal{I}_{Z_{69}}(t'), \quad (33b)$$

$$\mathcal{C}_x^{(1)}(t) = \int_0^t dt' \frac{e^{-\frac{t-t'}{T_c}}}{T_c} \mathcal{I}_{X_{12}}(t') \mathcal{I}_{X_{45}}(t') \mathcal{I}_{X_{78}}(t'), \quad (33c)$$

$$\mathcal{C}_x^{(2)}(t) = \int_0^t dt' \frac{e^{-\frac{t-t'}{T_c}}}{T_c} \mathcal{I}_{X_{23}}(t') \mathcal{I}_{X_{56}}(t') \mathcal{I}_{X_{89}}(t'), \quad (33d)$$

where T_c is an integration time parameter whose optimal value will be determined later, and $\mathcal{I}_{G_k}(t)$ is the measurement signal from continuous measurement of G_k , smoothed out by time averaging as follows:

$$\mathcal{I}_{G_k}(t) = \int_0^t dt' \frac{e^{-\frac{t-t'}{\tau_c}}}{\tau_c} I_{G_k}(t'), \quad (34)$$

Here τ_c is another integration time parameter that can also be optimized. We point out that, for detectors with different measurement strengths, the bare output signals $I_{G_k}(t)$ should be smoothed out using different integration time parameters; similarly, different integration time parameters should also be used in Eqs. (33a)–(33d). In this work, we carry out the time averaging with exponential weighting functions. Other functions (e.g., uniform weighting functions over a specified time window [46]) may also be used. Choosing the optimal weighting function is a topic for future work.

The cross-correlators $\mathcal{C}_z^{(1)}(t), \mathcal{C}_z^{(2)}(t), \mathcal{C}_x^{(1)}(t)$ and $\mathcal{C}_x^{(2)}(t)$ are constructed to continuously monitor the stabilizers $S_z^{(1)}, S_z^{(2)}, S_x^{(1)}$ and $S_x^{(2)}$ in real time, respectively. This monitoring is, however, not perfect since the cross-correlators are noisy even when the system state is in

a fixed subspace \mathcal{Q}_ℓ and they cannot immediately follow abrupt changes of the values of the stabilizers after occurrence of errors—Eq. (33) shows that the response time of cross-correlators is determined by the integration time parameter T_c . These imperfections render the jumps in the monitored error syndrome path, $\mathcal{S}_m(t)$, different from those of the actual error syndrome path, $\mathcal{S}(t)$, potentially leading to logical errors since the series of logical operations inferred from the monitored path $\mathcal{S}_m(t)$ is not the same as the actual one, obtained from the real error syndrome path $\mathcal{S}(t)$. Note that, in principle, continuous monitoring of the error syndrome path could be performed via simultaneous measurement of the four commuting stabilizer generators, Eq. (2), at the same time. However, this operation mode would require measurement of six-qubit operators, which is much more difficult to realize than measurement of two-qubit operators. Moreover, this is not necessary. We emphasize that the main implementation advantage of Bacon-Shor codes is that they can be operated with *only* two-qubit measurements.

To determine the monitored error syndrome path we use the following two-error-threshold algorithm. At $t = 0$, we set $\mathcal{S}_m(0) = \mathcal{S}(0) = 0$ because the initial encoding step is assumed perfect and the initial system state is in the code space. We *do not update* the monitored error syndrome path at the moment t if at least one of the following four inequalities holds ($q = x, z$ and $n = 1, 2$):

$$1 - \Theta_2 < \tilde{S}_q^{(n)}(t - \delta t) \frac{\mathcal{C}_q^{(n)}(t)}{\langle |\mathcal{C}_q^{(n)}| \rangle} < 1 - \Theta_1, \quad (35)$$

where Θ_1 and Θ_2 are the error threshold parameters that are fixed beforehand such that $0 \leq \Theta_1 \leq 1$ and $1 \leq \Theta_2 \leq 2$, and $\tilde{S}_q^{(n)}(t - \delta t) = \pm 1$ is the estimated value of the stabilizer generator $S_q^{(n)}$ that corresponds to the monitored error syndrome path at the moment $t - \delta t$ (δt is a small timestep). The denominator in Eq. (35) is used for normalization of the cross-correlators (33). The two threshold parameters (Θ_1 and Θ_2) will be optimized later. This strategy essentially says that if we are not sure about the values of the stabilizer generators, we hold the previous value of the monitored error syndrome path; i.e., $\mathcal{S}_m(t) = \mathcal{S}_m(t - \delta t)$. The error threshold parameters determine what we refer to as the “syndrome uncertainty region”. For detectors with the same measurement strength, the denominators of Eq. (35) are equal and depend on the integration time parameter τ_c as follows,

$$\langle |\mathcal{C}_q^{(n)}| \rangle = \frac{1}{3} \left[\frac{1}{(1 + \Gamma_m \tau_c)(1 + 2\Gamma_m \tau_c)} + \frac{1}{(1 + 2\Gamma_m \tau_c)^2} + \frac{1}{(1 + \Gamma_m \tau_c)(1 + 4\Gamma_m \tau_c)} \right]. \quad (36)$$

Equation (36) gives the magnitude of the ensemble average value of the cross-correlators in any subspace \mathcal{Q}_ℓ ; this

result is derived in the next subsection. The last component is to update the value of the monitored error syndrome path when all cross-correlators are outside of the “syndrome uncertainty region”. We do this as follows. We first digitize the cross-correlators, assigning them values of $+1$ or -1 if $\mathcal{C}_q^{(n)}(t)$ is larger than $(1 - \Theta_1)\langle |\mathcal{C}_q^{(n)}| \rangle$ or smaller than $(1 - \Theta_2)\langle |\mathcal{C}_q^{(n)}| \rangle$, respectively. The digitized values of $\mathcal{C}_x^{(1)}(t)$, $\mathcal{C}_z^{(1)}(t)$, $\mathcal{C}_x^{(2)}(t)$ and $\mathcal{C}_z^{(2)}(t)$ in this order constitute the estimated error syndrome pattern at moment t . We then use Table I to read out the subspace \mathcal{Q}_ℓ that agrees with that error syndrome pattern and update the monitored error syndrome path to $\mathcal{S}_m(t) = \ell$, where $\ell = 0, 1, \dots, 15$.

The QEC protocol discussed in Section III B works perfectly if we have access to the true error syndrome path, $\mathcal{S}(t)$. However, we actually have at our disposal only the monitored path $\mathcal{S}_m(t)$ that generally differs from $\mathcal{S}(t)$ because of the time averaging and the noise in the cross-correlators, $\mathcal{C}_q^{(n)}(t)$. This discrepancy can lead to different inferred total logical operations for the individual realizations and hence to logical errors. Indeed, let us assume that \mathcal{O} and \mathcal{O}_m are, respectively, the total logical operations inferred from $\mathcal{S}(t)$ and $\mathcal{S}_m(t)$ for a given realization. The final logical state at the end of this realization is $\mathcal{O}|\Psi_L\rangle$; however, the logical state that is returned to the user is $\mathcal{O}_m\mathcal{O}|\Psi_L\rangle$. Therefore, if $\mathcal{O}_m\mathcal{O} = X_L, Y_L$ or Z_L , such a realization contributes to the probability of a logical X, Y , or Z error, respectively. Assuming that the error rates of the physical qubits are sufficiently small, averaging over realizations then leads to a probability for logical errors of the form ($L = X, Y$ or Z)

$$P_L(T_{\text{op}}) = \gamma_L^{\text{cont}} T_{\text{op}} + \Delta P_L, \quad (37)$$

where $\gamma_L^{\text{cont}} = \gamma_X^{\text{cont}}$, γ_Y^{cont} or γ_Z^{cont} is the logical X, Y or Z error rate for the continuous operation of duration T_{op} and ΔP_L is a small probability offset. The logical error rates are calculated in Section III D. The probability offsets are due primarily to single-qubit errors that occur so close to the end of the continuous operation that there is no enough time for the cross-correlators to switch sign. Such errors therefore remain undetected and their associated logical operations (given by Table II) are not accounted for in the total logical operation \mathcal{O}_m , obtained from the monitored error syndrome path. These undetected errors also make $\mathcal{S}(T_{\text{op}}) \neq \mathcal{S}_m(T_{\text{op}})$; that is, the final system state is in subspace $\mathcal{Q}_{\mathcal{S}(T_{\text{op}})}$, while, from the monitored error syndrome path, we infer it is in subspace $\mathcal{Q}_{\mathcal{S}_m(T_{\text{op}})}$. We estimate the probability offsets as

$$\Delta P_X \approx \left(\Gamma_X^{(4)} + \Gamma_X^{(5)} + \Gamma_X^{(6)} + \Gamma_Y^{(4)} + \Gamma_Y^{(6)} \right) T_c \quad (38a)$$

$$\Delta P_Z \approx \left(\Gamma_Z^{(2)} + \Gamma_Z^{(5)} + \Gamma_Z^{(8)} + \Gamma_Y^{(2)} + \Gamma_Y^{(8)} \right) T_c \quad (38b)$$

$$\Delta P_Y \approx \Gamma_Y^{(5)} T_c \quad (38c)$$

if $T_{\text{op}} \gtrsim T_c$. The single-qubit errors, whose occurrence rates enter in Eqs. (38a)–(38c), are, respectively, those that affect the logical state by a single logical X_L , Z_L and Y_L operation, according to Table II. For $T_{\text{op}} \lesssim T_c$, we can approximate ΔP_L by Eq. (38) with T_c replaced by T_{op} . It is, however, possible to significantly reduce the probability offsets by measuring the gauge operators immediately after the end of the continuous operation (e.g., with projective measurements). This additional step would give us the actual value of the error syndrome path at the end of the continuous operation [i.e., $\mathcal{S}(T_{\text{op}})$], and then we can infer (from Tables II and III) the undetected single-qubit error $E \sim Q_{\ell'} O'$ (here $O' = X_L, Y_L$ or Z_L , and “ \sim ” indicates equivalence modulo gauge operators) that induces the jump from the subspace $\mathcal{Q}_{\mathcal{S}_m(T_{\text{op}})}$ to the subspace $\mathcal{Q}_{\mathcal{S}(T_{\text{op}})}$ near the end of the continuous operation. By adjusting \mathcal{O}_m to $\mathcal{O}_m O'$, the probability of logical errors is approximately given by Eq. (37) with ΔP_L set to zero, i.e., $P_L(T_{\text{op}}) \approx \gamma_L^{\text{cont}} T_{\text{op}}$.

Before concluding this section, we discuss the difficulty of using a one-error-threshold protocol to extract the monitored error syndrome path. For example, we might regard the digitized values of cross-correlators as -1 ($+1$) if they are below (above) a certain error threshold, and then update $\mathcal{S}_m(t)$ when some of such digitized cross-correlators changes sign, as described above. Unfortunately, such a one-error-threshold algorithm does not work, leading to logical error rates that scale linearly on the error rates of the physical qubits. Consequently, for sufficiently small values of $\Gamma_i^{(X,Y,Z)}$, continuous operation would perform worse than the discrete operation, for which the logical error rates scale quadratically with $\Gamma_i^{(X,Y,Z)}$, see Eq. (13). The reason for the failure of such one-error-threshold protocol is the noise in the cross-correlators: this makes a single-qubit error event that affects several cross-correlators induce several false jumps in $\mathcal{S}_m(t)$, thereby increasing the logical error probabilities. Figure 3 shows an example where the one-error-threshold algorithm leads to $\mathcal{S}_m(t)$ with two jumps instead of just one jump.

1. Optimal integration time τ_c

In this section we discuss the statistical properties of the cross-correlators of interest in the absence of errors, assuming that the system state is in the code space. We specifically consider $\mathcal{C}_x^{(1)}(t)$ since all cross-correlators have the same statistical properties in the case of detectors with the same measurement strength Γ_m . We are particularly interested in the limit where the integration time parameter T_c is much larger than the collapse time τ_{coll} due to measurement, which is defined as

$$\tau_{\text{coll}} = \frac{1}{\Gamma_m} = 2\eta\tau_m. \quad (39)$$

This limit is relevant for us because we shall find that the optimal continuous operation of the nine-qubit Bacon-

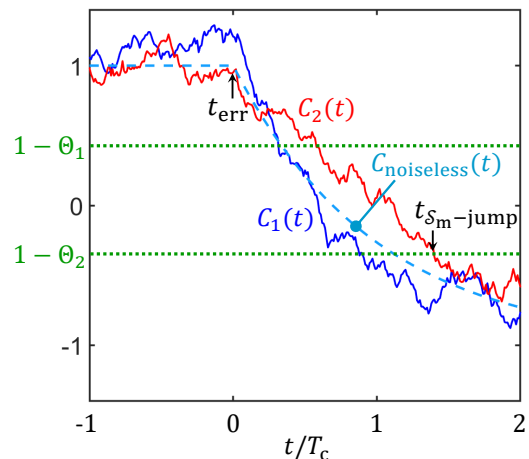


FIG. 3. Importance of using two error thresholds ($1 - \Theta_1$ and $1 - \Theta_2$) to determine the monitored error syndrome path $\mathcal{S}_m(t)$. The blue and red wiggly curves depict two normalized cross-correlators that change sign due to an error happening at moment t_{err} (the other two cross-correlators are assumed not to be affected by the error and not shown). In this scenario, the two-error-threshold algorithm of Section III C generates a $\mathcal{S}_m(t)$ with just one jump at the first moment $t_{\mathcal{S}_m\text{-jump}}$ (at this instant, the error is actually detected) when both cross-correlators are below the lower error threshold. This jump in $\mathcal{S}_m(t)$ indicates that the error syndrome pattern changes from $+++$ to $--++$, which is the actual error syndrome change due to the error. In contrast, the one-error-threshold algorithm discussed in the main text (with error threshold at, say, $1 - \Theta_2$) would lead to $\mathcal{S}_m(t)$ with two false jumps since the cross-correlators cross the error threshold at different moments. These false jumps would indicate the error syndrome pattern changing from $+++$ to $-+++$ (at the moment when the blue cross-correlator crosses the error threshold) and then from $-+++$ to $--++$ (at the moment when the red cross-correlator crosses the error threshold); consequently, two false errors would be detected instead of just one error.

Shor code requires T_c much larger than τ_{coll} —see Section IV.

In the large T_c limit, the fluctuations of the cross-correlator $\mathcal{C}_x^{(1)}(t)$ are approximately Gaussian because the integrand in Eq. (33c) has a comparatively short correlation time of order of $\tau_{\text{coll}} \ll T_c$ —see Eq. (65) below. The approximate Gaussian statistics of the cross-correlators of interest can be justified by the central-limit theorem if we consider the integration of Eq. (33c) as a sum of contributions from small nonoverlapping intervals of duration much larger than τ_{coll} and much shorter than T_c . These contributions are random and approximately statistically independent, so, in this limit, their sum equal to $\mathcal{C}_x^{(1)}(t)$ can be regarded as a Gaussian random number, characterized by its mean $\langle \mathcal{C}_x^{(1)}(t) \rangle$ and its variance

$$\text{Var}[\mathcal{C}_x^{(1)}(t)] = \langle [\mathcal{C}_x^{(1)}(t)]^2 \rangle - \langle \mathcal{C}_x^{(1)}(t) \rangle^2. \quad (40)$$

We actually characterize the relative size of the fluctua-

tions of $\mathcal{C}_x^{(1)}(t)$ by their Signal-to-Noise Ratio (SNR),

$$\text{SNR} = \frac{\langle \mathcal{C}_x^{(1)}(t) \rangle^2}{\text{Var}[\mathcal{C}_x^{(1)}(t)]}. \quad (41)$$

We find analytically and confirm numerically that the SNR of the cross-correlators is proportional to T_c for sufficiently large T_c , and it is a nonmonotonic function of the integration time parameter τ_c . We can then determine the optimal value of τ_c that maximizes the SNR.

We are going to calculate the SNR in the stationary regime $t \gg T_c$, where the statistical properties of the cross-correlator $\mathcal{C}_x^{(1)}(t)$ are time-independent. It is convenient to introduce the unfiltered correlator

$$\tilde{\mathcal{C}}_x^{(1)}(t) = \mathcal{I}_{X_{12}}(t) \mathcal{I}_{X_{45}}(t) \mathcal{I}_{X_{78}}(t). \quad (42)$$

In the large T_c limit, we can approximate the unfiltered correlator as

$$\tilde{\mathcal{C}}_x^{(1)}(t) \approx \langle \tilde{\mathcal{C}}_x^{(1)}(t) \rangle + \sqrt{\mathcal{D}_c} \tilde{\xi}_c(t), \quad (43)$$

where $\tilde{\xi}_c(t)$ is white noise with a two-time correlation function given by [its actual correlation function is given by Eq. (65)]

$$\langle \tilde{\xi}_c(t) \tilde{\xi}_c(t') \rangle = \delta(t - t'), \quad (44)$$

and \mathcal{D}_c is an effective diffusion coefficient for the cross-correlator fluctuations, given by

$$\mathcal{D}_c = 2 \int_0^\infty dt \langle [\tilde{\mathcal{C}}_x^{(1)}(t) - \langle \tilde{\mathcal{C}}_x^{(1)}(t) \rangle] [\tilde{\mathcal{C}}_x^{(1)}(0) - \langle \tilde{\mathcal{C}}_x^{(1)}(0) \rangle] \rangle. \quad (45)$$

Using Eq. (33c) and Eqs. (42)–(44), we find that the variance of the cross-correlator $\mathcal{C}_x^{(1)}(t)$ is equal to $\mathcal{D}_c/2T_c$, so in the large T_c limit, the SNR of the cross-correlators of interest is equal to

$$\text{SNR} = T_c \frac{2 \langle \mathcal{C}_x^{(1)}(t) \rangle^2}{\mathcal{D}_c}. \quad (46)$$

In the stationary regime, it is easy to further see that $\langle \mathcal{C}_x^{(1)}(t) \rangle$ is equal to $\langle \tilde{\mathcal{C}}_x^{(1)}(t) \rangle$, since the latter is time-independent in this regime and then the integral of Eq. (33c) is trivial. Combining Eqs. (34) and (42), we find that the averaged value of the unfiltered correlators is

$$\langle \tilde{\mathcal{C}}_x^{(1)}(t) \rangle = \int_{-\infty}^t dt_1 \int_{-\infty}^t dt_2 \int_{-\infty}^t dt_3 \langle I_{X_{12}}(t_1) I_{X_{45}}(t_2) \times I_{X_{78}}(t_3) \rangle \frac{e^{-\frac{t-t_1}{\tau_c} - \frac{t-t_2}{\tau_c} - \frac{t-t_3}{\tau_c}}}{\tau_c^3}, \quad (47)$$

where we have set the lower integration limits to $-\infty$, which is allowed in the stationary regime. As discussed in Section III A, the actual measurement signals, $I_{G_k}(t)$,

are the same (up to a sign factor) as the measurement signals $I_{G_k}(t)$ [see Eq. (26)] from simultaneous continuous measurement of the noncommuting operators \mathcal{G}_k that only act on the gauge qubits—see Eq. (22). The three-time correlator in the integrand of Eq. (47) becomes

$$\begin{aligned} K_3(t_1, t_2, t_3) &= \langle I_{X_3^g}(t_3) I_{X_{13}^g}(t_2) I_{X_1^g}(t_1) \rangle, \\ &= \langle I_{X_{78}}(t_3) I_{X_{45}}(t_2) I_{X_{12}}(t_1) \rangle, \end{aligned} \quad (48)$$

since $X_{12}(t) = X_1^g(t)$, $X_{45}(t) = X_{13}^g(t)$ and $X_{78}(t) = X_3^g(t)$; we assume that the system state is in the code space so the sign factors in Eq. (26) are one.

We shall use the following result (shown in the Supplemental Material of Ref. [61], see also Ref. [66])

$$\begin{aligned} K_{v_1 v_2 \dots v_N}(t_1, t_2, \dots, t_N) &= \langle I_{v_N}(t_N) \dots I_{v_2}(t_2) I_{v_1}(t_1) \rangle = \\ \text{Tr}[\mathcal{M}_{t_N} \mathcal{E}(t_N | t_{N-1}) \mathcal{M}_{t_{N-1}} \dots \mathcal{M}_{t_2} \mathcal{E}(t_2 | t_1) \mathcal{M}_{t_1} \mathcal{E}(t_1 | t_0) \rho_0], \end{aligned} \quad (49)$$

with $t_1 < t_2 < \dots < t_N$. Equation (49) is a general formula for N -time correlators of measurement signals $I_v(t)$ from simultaneous continuous measurement of an arbitrary number of (commuting or noncommuting) observables A_v of a quantum system. Here, $\mathcal{E}(t|t')$ is the trace-preserving ensemble-averaged evolution from time t' to t due to Lindblad term $\dot{\rho}_{\text{ens}} = \mathcal{L}[\rho_{\text{ens}}]$, while $\mathcal{M}_{t_k} \rho = (A_{v_k} \rho + \rho A_{v_k})/2$ is a trace-changing operation, related to the measurement of observables A_{v_k} .

In our problem, the ensemble-averaged evolution operation \mathcal{E} is determined by Eq. (23) without the noises:

$$\dot{\varrho}_{g,\text{ens}}(t) = \sum_k \frac{\Gamma_m}{2} [\mathcal{G}_k \varrho_{g,\text{ens}}(t) \mathcal{G}_k - \varrho_{g,\text{ens}}(t)], \quad (50)$$

where $\varrho_{g,\text{ens}}(t) = \langle \varrho_g(t) \rangle$. Expanding formula (49) with $N = 3$, $t_0 = t_1$, so that $\mathcal{E}(t_1|t_0)$ is the identity, and taking into account that A_v are Hermitian operators, we obtain

$$\begin{aligned} K_{v_1 v_2 v_3}(t_1, t_2, t_3) &= \frac{1}{2} \text{Tr}[A_{v_3} \mathcal{E}(t_3|t_2) A_{v_2} \mathcal{E}(t_2|t_1) A_{v_1} \times \\ &\varrho_g(t_1)] + \frac{1}{2} \text{Tr}[A_{v_3} \mathcal{E}(t_3|t_2) A_{v_2} \mathcal{E}(t_2|t_1) \varrho_g(t_1) A_{v_1}]. \end{aligned} \quad (51)$$

The trace terms of Eq. (51) can be easily calculated from the ensemble-averaged evolution Eq. (50). We show below that they are actually independent of $\varrho_g(t_1)$ for our cases of interest where $A_{v_3} A_{v_2} = A_{v_1}$ and A_{v_1}, A_{v_2} and A_{v_3} are Pauli operators.

Let us calculate Eq. (51) for $t_1 < t_2 < t_3$, so $A_{v_1} = X_1^g$, $A_{v_2} = X_{13}^g$ and $A_{v_3} = X_3^g$. We write the first trace term of this equation as

$$a(t_3) = \frac{1}{2} \text{Tr}[X_3^g \mathcal{E}(t_3|t_2) \tilde{\varrho}_{g,\text{ens}}(t_2)], \quad (52)$$

with

$$\tilde{\varrho}_{g,\text{ens}}(t_2) = X_{13}^g \mathcal{E}(t_2|t_1) X_1^g \varrho_g(t_1). \quad (53)$$

By multiplying both sides of Eq. (50) by X_3^g and then taking trace operations, we obtain

$$\dot{a}(t_3) = -2\Gamma_m a(t_3), \quad (54)$$

with the initial condition: $a(t_2) = \text{Tr}[X_3^g \tilde{\rho}_{g,\text{ens}}(t_2)]/2$. The decay rate $2\Gamma_m$ in Eq. (54) is due to the anticommutation of X_3^g with two gauge qubit operations \mathcal{G}_k ; namely, Z_3^g and Z_{34}^g , see Eq. (22). We then obtain the solution

$$a(t_3) = \frac{1}{2} e^{-2\Gamma_m(t_3-t_2)} \text{Tr}[X_3^g \tilde{\rho}_{g,\text{ens}}(t_2)]. \quad (55)$$

The trace factor of Eq. (55) can be written as

$$b(t_2) = \text{Tr}[X_3^g \tilde{\rho}_{g,\text{ens}}(t_2)] = \text{Tr}[X_1^g \mathcal{E}(t_2|t_1) X_1^g \rho_g(t_1)]. \quad (56)$$

We then derive the evolution equation for $b(t_2)$ from Eq. (50) by multiplying both sides of this equation by X_1 and then taking trace operations. We obtain

$$\dot{b}(t_2) = -2\Gamma_m b(t_2), \quad (57)$$

where the decay rate $2\Gamma_m$ is now due to the anticommutation of X_1^g with $\mathcal{G}_k = Z_1^g$ and Z_{12}^g . The initial condition for Eq. (57) is $b(t_1) = \text{Tr}[X_1^g X_1^g \rho_g(t_1)] = 1$. Note that the first trace term of Eq. (51) is independent of $\rho_g(t_1)$ because $A_{v_3} A_{v_2} = A_{v_1}$ and $A_{v_1} = X_1^g$ is a Pauli operator; the same holds for the second trace term of Eq. (51). We obtain from Eq. (57)

$$b(t_2) = e^{-2\Gamma_m(t_2-t_1)}. \quad (58)$$

The first trace term of Eq. (51) is therefore equal to

$$a(t_3) = \frac{1}{2} e^{-2\Gamma_m(t_3-t_2)} e^{-2\Gamma_m(t_2-t_1)}. \quad (59)$$

The calculation of the second trace term of Eq. (51) is similar, giving the same contribution (59) to K_3 . The sought three-time correlator (48) is then equal to

$$K_3(t_1, t_2, t_3) = e^{-2\Gamma_m(t_3-t_2)} e^{-2\Gamma_m(t_2-t_1)}, \text{ for } t_1 < t_2 < t_3. \quad (60)$$

We can proceed by similar means to obtain

$$\begin{aligned} K_3(t_1, t_2, t_3) &= e^{-4\Gamma_m(t_2-t_3)} e^{-2\Gamma_m(t_3-t_1)}, \text{ for } t_1 < t_3 < t_2, \\ &= e^{-2\Gamma_m(t_3-t_1)} e^{-4\Gamma_m(t_1-t_2)}, \text{ for } t_2 < t_1 < t_3, \\ &= e^{-2\Gamma_m(t_1-t_3)} e^{-4\Gamma_m(t_3-t_2)}, \text{ for } t_2 < t_3 < t_1, \\ &= e^{-4\Gamma_m(t_2-t_1)} e^{-2\Gamma_m(t_1-t_3)}, \text{ for } t_3 < t_1 < t_2, \\ &= e^{-2\Gamma_m(t_1-t_2)} e^{-2\Gamma_m(t_2-t_3)}, \text{ for } t_3 < t_2 < t_1. \end{aligned} \quad (61)$$

Inserting the expressions (60)–(61) in Eq. (47), and performing the integrals, we arrive at

$$\langle \tilde{\mathcal{C}}_x^{(1)}(t) \rangle = \langle \mathcal{C}_x^{(1)}(t) \rangle = \frac{1}{3} \left[\frac{1}{(1 + \Gamma_m \tau_c)(1 + 2\Gamma_m \tau_c)} + \frac{1}{(1 + 2\Gamma_m \tau_c)^2} + \frac{1}{(1 + \Gamma_m \tau_c)(1 + 4\Gamma_m \tau_c)} \right] \zeta_7^{(\ell)} \zeta_8^{(\ell)} \zeta_9^{(\ell)}, \quad (62)$$

where we have included the sign factor $\zeta_7^{(\ell)} \zeta_8^{(\ell)} \zeta_9^{(\ell)}$ from Eq. (26), which can be nontrivial in some error subspaces. However, this sign factor does not change the SNR.

Next, we proceed to calculate \mathcal{D}_c given in Eq. (45). To do this, we first need to calculate the two-time correlator of the unfiltered correlator $\tilde{\mathcal{C}}_x^{(1)}(t)$, given by

$$\begin{aligned} \langle \tilde{\mathcal{C}}_x^{(1)}(t) \tilde{\mathcal{C}}_x^{(1)}(0) \rangle &= \int_{-\infty}^t dt_1 \int_{-\infty}^t dt_2 \int_{-\infty}^t dt_3 \\ &\int_{-\infty}^0 dt'_1 \int_{-\infty}^0 dt'_2 \int_{-\infty}^0 dt'_3 K_6(t_1, t'_1, t_2, t'_2, t_3, t'_3) \\ &\times \frac{e^{-\frac{t-t_1}{\tau_c} - \frac{t-t_2}{\tau_c} - \frac{t-t_3}{\tau_c} + \frac{t'_1}{\tau_c} + \frac{t'_2}{\tau_c} + \frac{t'_3}{\tau_c}}}{\tau_c^6}, \end{aligned} \quad (63)$$

where

$$\begin{aligned} &K_6(t_1, t'_1, t_2, t'_2, t_3, t'_3) = \\ &\langle I_{X_3^g}(t_3) I_{X_3^g}(t'_3) I_{X_{13}^g}(t_2) I_{X_{13}^g}(t'_2) I_{X_1^g}(t_1) I_{X_1^g}(t'_1) \rangle \end{aligned} \quad (64)$$

is a six-time correlator that we evaluate using formula (49). The calculation of Eq. (63) is cumbersome because of the time ordering, needed to evaluate the integrand of this equation using the result (49). We also have to take into account singular contributions to K_6 that occur when $t_1 = t'_1$, $t_2 = t'_2$ or $t_3 = t'_3$, see Appendix D. The final result reads as

$$\begin{aligned} \langle \tilde{\mathcal{C}}_x^{(1)}(t) \tilde{\mathcal{C}}_x^{(1)}(0) \rangle - \langle \tilde{\mathcal{C}}_x^{(1)}(t) \rangle^2 &= \left[\frac{1}{8s^3 \eta^3} + R_1 \right] e^{-\frac{3|t|}{\tau_c}} + \\ &R_2 e^{-\frac{|t|}{\tau_c} - \frac{2|t|}{\tau_{\text{coll}}}} + R_3 e^{-\frac{2|t|}{\tau_c} - \frac{2|t|}{\tau_{\text{coll}}}} + R_4 e^{-\frac{|t|}{\tau_c} - \frac{4|t|}{\tau_{\text{coll}}}} + \\ &R_5 e^{-\frac{2|t|}{\tau_c} - \frac{4|t|}{\tau_{\text{coll}}}}, \end{aligned} \quad (65)$$

where $s = 2\tau_c \tau_{\text{coll}}^{-1}$, $R_l = R_l(s, \eta)$ is a rational function of s and the quantum efficiency parameter η , see Appendix D, and $\langle \tilde{\mathcal{C}}_x^{(1)}(t) \rangle$ is given explicitly in Eq. (62). Note that the correlation time of the unfiltered correlator $\tilde{\mathcal{C}}_x^{(1)}(t)$ in Eq. (65) is only determined by the integration time parameter τ_c and the collapse time τ_{coll} due to continuous measurement. We shall see below that the optimal integration time parameter τ_c is of the order of τ_{coll} , so our earlier assumption that the fluctuations $\tilde{\xi}_c(t)$ of the unfiltered correlators can be regarded as white, i.e., unstructured, is justified in the limit of interest where $T_c/\tau_{\text{coll}} \gg 1$.

We can now evaluate the effective diffusion coefficient \mathcal{D}_c from Eqs. (65) and (45), and hence obtain the SNR of the cross-correlators of interest, Eq. (46), in the large T_c limit as

$$\text{SNR} = \frac{16 (T_c/\tau_{\text{coll}}) \eta^3 s^2 (s+1)(s+2)(s+3)(s+4)(2s+1)(2s+3)(8s^2+15s+6)^2}{\left[864 + 216(55+36\eta)s + 12(6145+7902\eta+2592\eta^2)s^2 + 18(15211+28710\eta+18512\eta^2)s^3 \right.}$$

$$+ 3(226437+555214\eta+522576\eta^2+13824\eta^3)s^4 + 3(397086+1180221\eta+1426120\eta^2+116992\eta^3)s^5$$

$$+ (1522503+5239407\eta+7535364\eta^2+1272544\eta^3)s^6 + 6(240069+925035\eta+1502502\eta^2+430792\eta^3)s^7$$

$$+ (1013421+4259496\eta+7504140\eta^2+3235624\eta^3)s^8 + 3(175818+789057\eta+1458060\eta^2+863636\eta^3)s^9$$

$$+ (199809+940479\eta+1770048\eta^2+1331548\eta^3)s^{10} + 4(13347+64890\eta+121128\eta^2+106744\eta^3)s^{11}$$

$$\left. + 24(396+1963\eta+3548\eta^2+3308\eta^3)s^{12} + 16(63+315\eta+540\eta^2+452\eta^3)s^{13} + 48(1+\eta)(1+2\eta)^2s^{14} \right]. \quad (66)$$

Figure 4 plots the value of the SNR Eq. (66) as function of the integration time parameter τ_c for two different values of the measurement efficiency η . We note that the SNR decreases as τ_c gets smaller. This is expected since the “signal part” of $\mathcal{C}_x^{(1)}(t)$ converges to one as $\tau_c \rightarrow 0$ (see Eq. (62)), while the variance of the fluctuations of $\mathcal{C}_x^{(1)}(t)$ increases as τ_c^{-2} . Indeed, in the small τ_c limit, the leading term of $\langle \tilde{\mathcal{C}}_x^{(1)}(t) \tilde{\mathcal{C}}_x^{(1)}(0) \rangle - \langle \tilde{\mathcal{C}}_x^{(1)}(t) \rangle^2$ is $\exp(-3|t|/\tau_c) \tau_{\text{coll}}^3/64\eta^3\tau_c^3$, so $\mathcal{D}_c \approx \tau_{\text{coll}}^3/96\eta^3\tau_c^2$ and $\text{SNR} \approx 192\eta^3\tau_c^2 T_c/\tau_{\text{coll}}^3$. In the large τ_c limit, the SNR decreases as τ_c^{-2} because the “signal part” decreases as $(\tau_c^{-2})^2$, see Eq. (62), while the variance of the fluctuations of $\mathcal{C}_x^{(1)}(t)$ decreases as τ_c^{-2} . In Fig. 4, we have also plotted the exact analytical values of SNR (dashed lines), obtained without taking the large T_c limit. We see that, for an integration time $T_c = 30\tau_{\text{coll}}$, the difference between the estimates of the SNR with and without taking the large T_c limit is small. We do not provide the analytical formula for the SNR at an arbitrary integration time T_c . However, this can be readily obtained from the result (65) when it is used to calculate $\text{Var}[\mathcal{C}_x^{(1)}(t)]$ in

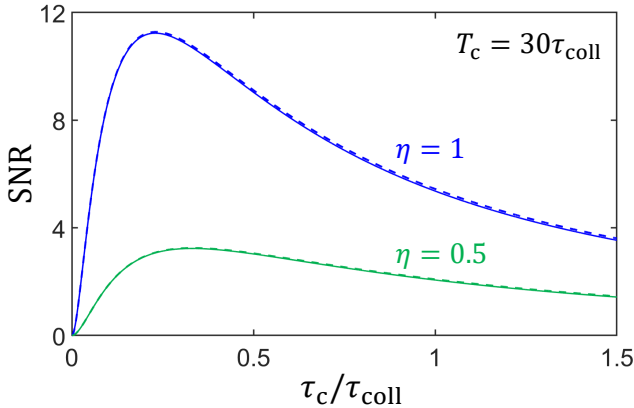


FIG. 4. SNR of cross-correlators as function of the integration time parameter τ_c . Solid lines plot formula (66) that is valid in the large T_c limit for two values of quantum efficiency η . Dashed lines plot the analytical result that is valid for any value of T_c (not given).

Eq. (41).

By maximizing the SNR with fixed values of T_c and η , we arrive at the optimal value of the integration time parameter τ_c

$$\tau_c^{\text{opt}} \approx 0.229\tau_{\text{coll}} \quad (\eta = 1), \quad \tau_c^{\text{opt}} \approx 0.331\tau_{\text{coll}} \quad (\eta = 0.5). \quad (67)$$

The optimal value of the second integration time parameter T_c is presented in Section IV.

D. Logical error rates for continuous operation of nine-qubit Bacon-Shor code

1. Large T_c limit

In this section we calculate the logical error rates for continuous operation of the nine-qubit Bacon-Shor code in the large T_c limit. In this limit all fluctuations of the cross-correlators $\mathcal{C}_q^{(n)}(t)$ can be neglected ($q = x, z$ and $n = 1, 2$). The evolution of the normalized cross-correlators (the normalization factor is given by Eq. (36); sometimes we shall omit reference to the normalization) due to occurrence of a single error at moment t_{err} is given by (for $t > t_{\text{err}}$)

$$C_{\text{noiseless}}(t) = -1 + 2e^{-\frac{t-t_{\text{err}}}{T_c}}. \quad (68)$$

Note that previous to the occurrence of the error, $C_{\text{noiseless}}(t)$ has the value of +1, and after the error it asymptotically approaches -1 at large times—see Fig 3. The exponential form of $C_{\text{noiseless}}(t)$ comes from the exponential weighting function used in the definition of the cross-correlators—see Eq. (33).

In the large T_c limit and for sufficiently small physical error rates $\Gamma_i^{(X,Y,Z)}$, logical errors are due primarily to two error combinations (E_1 and E_2) that are incorrectly diagnosed as a single error (E_{false}) by our QEC protocol. This happens when the two errors occur sufficiently close in time, a situation similar to that in the discrete operation, where logical errors derive from harmful two-qubit errors that occur within the same cycle. We denote the

time window in which two errors are diagnosed as one error as Δt_{cont} . This means that if the first and second errors occur at moments $t_{\text{err}}^{(1)}$ and $t_{\text{err}}^{(2)}$, respectively, they are not individually diagnosed when $t_{\text{err}}^{(2)} - t_{\text{err}}^{(1)} < \Delta t_{\text{cont}}$. We shall determine the time window Δt_{cont} that is specific to our continuous QEC protocol and use it to calculate the corresponding logical error rates. We will see that the resulting formulas for the logical error rates in the continuous operation are similar to those of the discrete operation [Eqs. (C1)–(C2)], with Δt_{cont} playing the role of the cycle time Δt .

Detailed analysis shows that the time window Δt_{cont} can take two possible values, namely,

$$\Delta t_{\text{cont}}^{(1)} = T_c \ln \left[\frac{2 - \Theta_1}{2 - \Theta_2} \right], \quad (69a)$$

$$\Delta t_{\text{cont}}^{(2)} = T_c \ln \left[\frac{2}{2 - \Theta_2} \right], \quad (69b)$$

where $\Delta t_{\text{cont}}^{(1)}$ is the time that $C_{\text{noiseless}}(t)$ spends in the “syndrome uncertainty region” (i.e., in between the error thresholds $1 - \Theta_1$ and $1 - \Theta_2$), and $\Delta t_{\text{cont}}^{(2)}$ is the time that $C_{\text{noiseless}}(t)$ takes to reach the lower error threshold ($1 - \Theta_2$) after the error occurs.

To see why Δt_{cont} has the values given in Eq. (69), we analyze the scenarios depicted in Fig. 5. This figure shows the nontrivial noiseless cross-correlators that are affected by the two errors (trivial cross-correlators unchanged by the errors are constant and equal to +1). We assume that the first error (E_1) occurs at moment $t_{\text{err}}^{(1)} = 0$ and affects, for simplicity, only one cross-correlator, denoted by $C_1(t)$, and the second error (E_2) also affects only one cross-correlator, denoted by $C_2(t)$. In Fig. 5 (a), the first error changes the error syndrome pattern, say, from ++++ to -+++ and then the second error changes the error syndrome pattern from -+++ to --++. To detect both of these changes in the error syndrome pattern using our continuous QEC protocol, $C_2(t)$ has to cross the upper error threshold ($1 - \Theta_1$) later than the moment at which $C_1(t)$ exits the “syndrome uncertainty region”. Otherwise, our algorithm would detect only one error syndrome transition from ++++ to --++. It is easy to see from Fig. 5 (a) and Eq. (68) that errors E_1 and E_2 are not individually detectable if $t_{\text{err}}^{(2)} - t_{\text{err}}^{(1)} < \Delta t_{\text{cont}}^{(1)}$, with $\Delta t_{\text{cont}}^{(1)}$ given in Eq. (69a).

The scenarios shown in Fig. 5 (b)–(c) are similar, in the sense that both lead to the time window $\Delta t_{\text{cont}}^{(2)}$. However, the error syndrome transitions are different in the two scenarios. In Fig. 5 (b), the first error E_1 changes the error syndrome pattern from ++++ to --++ and then the second error E_2 changes it from --++ to -+ ++. In Fig. 5 (c), E_1 changes the error syndrome pattern from ++++ to -+ ++ and then E_2 changes it from -+ ++ to +- ++. Each of these transitions between error syndromes values are individually detectable if the second error occurs after the cross-correlator $C_1(t)$ exits the “syndrome uncertainty region”. This condition

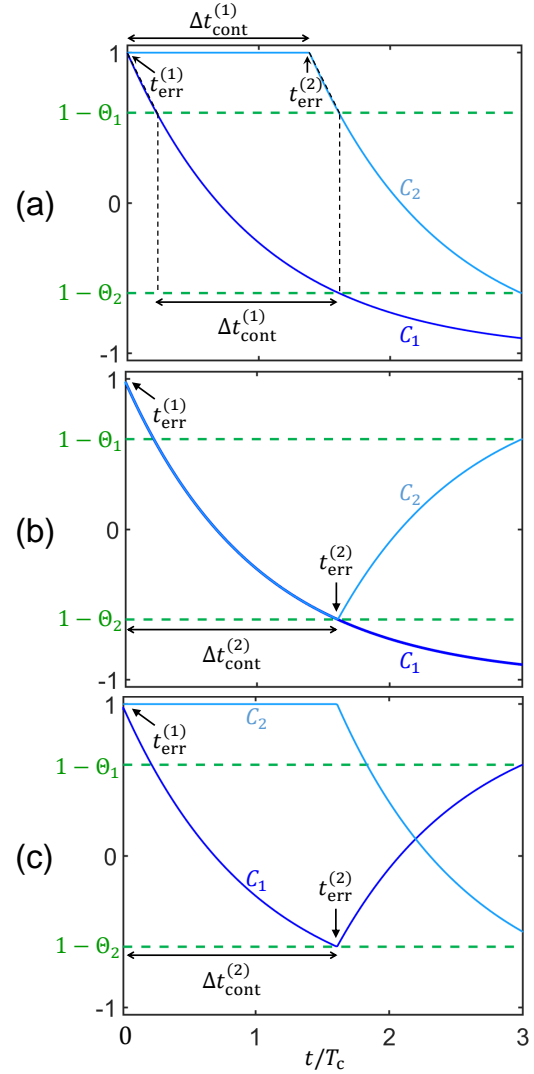


FIG. 5. Evolution of normalized cross-correlators in the large integration time T_c (noiseless) limit after occurrence of two errors. Cross-correlators not affected by errors are constant and equal to +1 (not shown). Panel (a) shows the evolution of two nontrivial cross-correlators C_1 and C_2 in the case where the first error changes the error syndrome pattern from ++++ to -+++ at moment $t_{\text{err}}^{(1)}$ (so only C_1 is affected by the first error) and the second error changes the error syndrome pattern from -+++ to --++ at moment $t_{\text{err}}^{(2)}$ (so only C_2 is affected by the second error). Both cross-correlators approach -1 at large times. Panel (b) shows the cross-correlators after the errors change the error syndrome pattern from ++++ to --++ and then from --++ to -+ ++, so first error affects both correlators and then second error affects only C_2 . Cross-correlators C_1 and C_2 approach -1 and $+1$ at larger times, respectively. Panel (c) shows the cross-correlators for the case where the error syndrome pattern changes from ++++ to -+ ++ and then from -+ ++ to +- ++. At large times, the correlators C_1 and C_2 approach $+1$ and -1 , respectively.

leads to the time window $\Delta t_{\text{cont}} = \Delta t_{\text{cont}}^{(2)}$ that is given in Eq. (69b).

To get a logical error, the misdiagnosed two error combination E_1E_2 has to be one of the harmful two-qubit errors given in Eqs. (9)–(11)—see also Appendix B 3. Indeed, for E_{false} (the incorrectly diagnosed single-qubit error) and E_1E_2 to produce the same jump of the system state from the code space to the some fixed error subspace, the product $E_1E_2E_{\text{false}}$ has to be trivial (i.e., a product of gauge operators) or equivalent (modulo gauge operators) to a logical operation (X_L , Y_L , or Z_L). The latter possibility is the condition for a harmful two-qubit error that is given in Eq. (B7) with E_{false} playing the role of the error correcting operation C_{op} —see also Appendix B 3. The probability that the harmful two-qubit error E_1E_2 is misdiagnosed is given by $(\Gamma_{E_1}T_{\text{op}})(\Gamma_{E_2}\Delta t_{\text{cont}})$, where the first factor is the probability that first error occurs during the operation duration T_{op} and the second factor is the probability that the second error occurs within the time window Δt_{cont} . The corresponding logical error rate is obtained by dividing this probability by T_{op} .

To find the contributions to the logical X , Z and Y error rates from scenario Fig. 5 (a), we look for all harmful two-qubit error combinations from Eqs. (9)–(11) that lead to cross-correlators evolving as shown in Fig. 5 (a). (Note that we also have to include harmful two-qubit errors where each error affects two or more cross-correlators at the same time; in this case, the blue and cyan curves in Fig. 5 (a) correspond to cross-correlators that evolve in the same fashion without noise.) We obtain

$$\Delta_1\gamma_X = 2\Delta t_{\text{cont}}^{(1)} \left[(\Gamma_1^{(X)} + \Gamma_2^{(X)} + \Gamma_3^{(X)}) (\Gamma_7^{(X)} + \Gamma_8^{(X)} + \Gamma_9^{(X)}) + (\Gamma_1^{(Y)} + \Gamma_2^{(Y)} + \Gamma_3^{(Y)}) (\Gamma_7^{(X)} + \Gamma_8^{(X)} + \Gamma_9^{(X)}) + (\Gamma_1^{(X)} + \Gamma_2^{(X)} + \Gamma_3^{(X)}) (\Gamma_7^{(Y)} + \Gamma_8^{(Y)} + \Gamma_9^{(Y)}) \right], \quad (70a)$$

$$\Delta_1\gamma_Z = 2\Delta t_{\text{cont}}^{(1)} \left[(\Gamma_1^{(Z)} + \Gamma_4^{(Z)} + \Gamma_7^{(Z)}) (\Gamma_3^{(Z)} + \Gamma_6^{(Z)} + \Gamma_9^{(Z)}) + (\Gamma_1^{(Y)} + \Gamma_4^{(Y)} + \Gamma_7^{(Y)}) (\Gamma_3^{(Z)} + \Gamma_6^{(Z)} + \Gamma_9^{(Z)}) + (\Gamma_1^{(Z)} + \Gamma_4^{(Z)} + \Gamma_7^{(Z)}) (\Gamma_3^{(Y)} + \Gamma_6^{(Y)} + \Gamma_9^{(Y)}) \right], \quad (70b)$$

$$\Delta_1\gamma_Y = 2\Delta t_{\text{cont}}^{(1)} \left[\Gamma_1^{(Y)}\Gamma_9^{(Y)} + \Gamma_3^{(Y)}\Gamma_7^{(Y)} \right], \quad (70c)$$

where the factor of two in Eqs. (70a)–(70c) is related to the order of the occurrence of errors E_1 and E_2 (two-qubit error combinations (E_1, E_2) and (E_2, E_1) give the same contribution for the logical X , Y or Z error rates). We proceed in a similar manner to obtain the contributions to the logical error rates from the scenarios shown

in Fig. 5 (b)–(c). We obtain

$$\begin{aligned} \Delta_2\gamma_X = 2\Delta t_{\text{cont}}^{(2)} & \left[(\Gamma_1^{(X)} + \Gamma_2^{(X)} + \Gamma_3^{(X)} + \Gamma_7^{(X)} + \Gamma_8^{(X)} \right. \\ & + \Gamma_9^{(X)}) (\Gamma_4^{(X)} + \Gamma_5^{(X)} + \Gamma_6^{(X)} + \Gamma_4^{(Y)} + \Gamma_5^{(Y)} + \Gamma_6^{(Y)}) + \\ & (\Gamma_1^{(Y)} + \Gamma_2^{(Y)} + \Gamma_3^{(Y)} + \Gamma_7^{(Y)} + \Gamma_8^{(Y)} + \Gamma_9^{(Y)}) (\Gamma_4^{(X)} + \Gamma_5^{(X)} \\ & + \Gamma_6^{(X)}) + \Gamma_4^{(Y)}\Gamma_7^{(Y)} + \Gamma_1^{(Y)}(\Gamma_4^{(Y)} + \Gamma_7^{(Y)}) + \Gamma_5^{(Y)}\Gamma_8^{(Y)} \\ & \left. + \Gamma_2^{(Y)}(\Gamma_5^{(Y)} + \Gamma_8^{(Y)}) + \Gamma_6^{(Y)}\Gamma_9^{(Y)} + \Gamma_3^{(Y)}(\Gamma_6^{(Y)} + \Gamma_9^{(Y)}) \right], \quad (71a) \end{aligned}$$

$$\begin{aligned} \Delta_2\gamma_Z = 2\Delta t_{\text{cont}}^{(2)} & \left[(\Gamma_1^{(Z)} + \Gamma_4^{(Z)} + \Gamma_7^{(Z)} + \Gamma_3^{(Z)} + \Gamma_6^{(Z)} \right. \\ & + \Gamma_9^{(Z)}) (\Gamma_2^{(Z)} + \Gamma_5^{(Z)} + \Gamma_8^{(Z)} + \Gamma_2^{(Y)} + \Gamma_5^{(Y)} + \Gamma_8^{(Y)}) + \\ & (\Gamma_1^{(Y)} + \Gamma_4^{(Y)} + \Gamma_7^{(Y)} + \Gamma_3^{(Y)} + \Gamma_6^{(Y)} + \Gamma_9^{(Y)}) (\Gamma_2^{(Z)} + \Gamma_5^{(Z)} \\ & + \Gamma_8^{(Z)}) + \Gamma_2^{(Y)}\Gamma_3^{(Y)} + \Gamma_1^{(Y)}(\Gamma_2^{(Y)} + \Gamma_3^{(Y)}) + \Gamma_5^{(Y)}\Gamma_6^{(Y)} \\ & \left. + \Gamma_4^{(Y)}(\Gamma_5^{(Y)} + \Gamma_6^{(Y)}) + \Gamma_8^{(Y)}\Gamma_9^{(Y)} + \Gamma_7^{(Y)}(\Gamma_8^{(Y)} + \Gamma_9^{(Y)}) \right], \quad (71b) \end{aligned}$$

$$\begin{aligned} \Delta_2\gamma_Y = 2\Delta t_{\text{cont}}^{(2)} & \left[\Gamma_2^{(Y)}(\Gamma_4^{(Y)} + \Gamma_7^{(Y)} + \Gamma_6^{(Y)} + \Gamma_9^{(Y)}) + \right. \\ & \Gamma_1^{(Y)}(\Gamma_5^{(Y)} + \Gamma_8^{(Y)} + \Gamma_6^{(Y)}) + \Gamma_3^{(Y)}(\Gamma_4^{(Y)} + \Gamma_5^{(Y)} + \Gamma_8^{(Y)}) \\ & + (\Gamma_5^{(Y)} + \Gamma_6^{(Y)})\Gamma_7^{(Y)} + (\Gamma_4^{(Y)} + \Gamma_6^{(Y)})\Gamma_8^{(Y)} \\ & \left. + (\Gamma_4^{(Y)} + \Gamma_5^{(Y)})\Gamma_9^{(Y)} \right]. \quad (71c) \end{aligned}$$

The logical X , Z and Y error rates are then obtained from the sum of the corresponding contributions given in Eqs. (70)–(71), e.g., $\Delta_1\gamma_X + \Delta_2\gamma_X = \gamma_X^{\text{cont}}$. We evaluate the logical error rates for the depolarizing channel of Eq. (14). For this large T_c limit we then obtain

$$\gamma_X^{\text{cont}} = \gamma_Z^{\text{cont}} = 6T_c\Gamma_d^2 \ln \left[\frac{2 - \Theta_1}{2 - \Theta_2} \right] + 14T_c\Gamma_d^2 \ln \left[\frac{2}{2 - \Theta_2} \right], \quad (72a)$$

$$\gamma_Y^{\text{cont}} = \frac{4}{9}T_c\Gamma_d^2 \ln \left[\frac{2 - \Theta_1}{2 - \Theta_2} \right] + \frac{32}{9}T_c\Gamma_d^2 \ln \left[\frac{2}{2 - \Theta_2} \right]. \quad (72b)$$

The total logical error rate, $\gamma_{\text{cont}} = \gamma_X^{\text{cont}} + \gamma_Y^{\text{cont}} + \gamma_Z^{\text{cont}}$, reads as

$$\gamma_{\text{cont}} = \frac{112}{9}T_c\Gamma_d^2 \ln \left[\frac{2 - \Theta_1}{2 - \Theta_2} \right] + \frac{284}{9}T_c\Gamma_d^2 \ln \left[\frac{2}{2 - \Theta_2} \right], \quad (73)$$

in the large T_c limit. We thus find that our continuous QEC protocol leads to logical error rates that scale quadratically on the error rates of the physical qubits (Γ_d in Eq. (73)). This scaling shows that our QEC protocol can successfully detect and correct single-qubit errors if they occur sufficiently far apart in time. A somewhat

similar condition also applies in the discrete operation for single-qubit errors to be correctable, namely, that they have to occur in different cycles. Note also the similarity between formulas Eq. (72) and Eq. (15); this indicates that the integration time parameter T_c (up to a proportionality factor) plays the role of the cycle time Δt in the discrete operation of the nine-qubit Bacon-Shor code.

2. Small T_c limit

In this limit we cannot neglect fluctuations in the cross-correlators $\mathcal{C}_q^{(n)}(t)$ since they can make single-qubit errors appear as two-qubit errors to our continuous QEC protocol, potentially leading to logical errors. That is, the measurement noise present in the continuous operation can render single-qubit errors uncorrectable. We shall assume that fluctuations of the cross-correlators are Gaussian; this assumption is justified in Section III C 1.

We now discuss the two most probable scenarios in which large fluctuations in the cross-correlators lead to logical errors.

Scenario 1: In scenario one, a single-qubit error E flips the sign of two stabilizer generators at the same time (so error syndrome changes from, e.g., ++++ to --++). If the affected (normalized) cross-correlators, referred to for simplicity here as $C_1(t)$ and $C_2(t)$, do not undergo large fluctuations, they should follow trajectories like those shown in Fig. 3 and then our continuous QEC protocol will detect the actual single-qubit error without problems at the first moment when both cross-correlators are below the lower error threshold. However, our continuous QEC protocol will detect two errors (instead of one error) if one of the cross-correlators crosses the upper error threshold due to a positive large fluctuation while the other is below the lower error threshold without undergoing large fluctuations. This situation is somewhat similar to the one depicted in Fig. 5 (b), except that the rise of $C_2(t)$ is now due not to a second error but to a large fluctuation. Naively speaking, the probability that this scenario occurs in one experimental realization is given by

$$P_{\text{scn-1}} = 2\Gamma_E T_{\text{op}} P_1(\Delta C \geq \Theta_2 - \Theta_1), \quad (74)$$

where the last factor is the probability that the correlator difference $\Delta C(t) = C_2(t) - C_1(t)$ is larger than the difference of the error thresholds that is equal to $\Theta_2 - \Theta_1$ and Γ_E is the occurrence rate of the actual error. The factor of two in Eq. (74) is due to the fact that a logical error can come from a large fluctuation in either $C_1(t)$ or $C_2(t)$. The corresponding logical error rate is $P_{\text{scn-1}}/T_{\text{op}}$.

To find the probability factor in Eq. (74), we consider the following evolution equations for the two normalized cross-correlators $C_1(t)$ and $C_2(t)$ that are affected by the

actual error

$$\dot{C}_1(t) = -\frac{C_1(t) - s_1}{T_c} + \frac{\sqrt{\mathcal{D}_c/\langle \mathcal{C} \rangle^2}}{T_c} \tilde{\xi}_c^{(1)}(t), \quad (75)$$

$$\dot{C}_2(t) = -\frac{C_2(t) - s_2}{T_c} + \frac{\sqrt{\mathcal{D}_c/\langle \mathcal{C} \rangle^2}}{T_c} \tilde{\xi}_c^{(2)}(t), \quad (76)$$

where $s_k = \pm 1$ are the values of the corresponding stabilizer generators, the diffusion coefficient \mathcal{D}_c can be obtained from Eqs. (46) and (66) with $\langle \mathcal{C} \rangle = \langle \mathcal{C}_x^{(1)} \rangle$ given in Eq. (62), and the uncorrelated white noises $\tilde{\xi}_c^{(1,2)}(t)$ have a two-time correlation function given by ($m, n = 1, 2$)

$$\langle \tilde{\xi}_c^{(m)}(t) \tilde{\xi}_c^{(n)}(t') \rangle = \delta_{mn} \delta(t - t'). \quad (77)$$

Note that the factors in front of the noises in Eqs. (75)–(76) are inversely proportional to T_c : thus the smaller T_c , the larger the fluctuations of the cross-correlators. Since we consider errors that simultaneously flip the sign of two stabilizer generators, we set $s_1 = s_2 = -1$. Before the actual error happens, the normalized cross-correlators fluctuate around +1 with a typical standard deviation of $[\mathcal{D}_c/2T_c\langle \mathcal{C} \rangle^2]^{1/2} = \text{SNR}^{-1/2}$, where the signal-to-noise ratio SNR is given in Eq. (66). The following evolution equation for the correlator difference $\Delta C(t)$ is obtained from Eqs. (75)–(76):

$$\Delta \dot{C}(t) = -\frac{\Delta C(t)}{T_c} + \frac{\sqrt{2\mathcal{D}_c/\langle \mathcal{C} \rangle^2}}{T_c} \Delta \tilde{\xi}_c(t), \quad (78)$$

where the white noise $\Delta \tilde{\xi}_c(t) = [\tilde{\xi}_c^{(2)}(t) - \tilde{\xi}_c^{(1)}(t)]/\sqrt{2}$ has the same two-time correlation function as $\tilde{\xi}_c^{(1)}(t)$ or $\tilde{\xi}_c^{(2)}(t)$. Note that $\langle \Delta C(t) \rangle = 0$ before and after the occurrence of the error, so the stochastic process $\Delta C(t)$ is actually stationary and not affected by the error. The stationary probability distribution function of the correlator difference ΔC can be obtained from Eq. (78) as:

$$P_{1,\text{st}}(\Delta C) = \left[\frac{\text{SNR}}{4\pi} \right]^{1/2} \exp\left(-\frac{\text{SNR}}{4} \Delta C^2\right), \quad (79)$$

which can be exponentially small as we increase the integration time parameter T_c since $\text{SNR} \propto T_c$, for sufficiently large T_c , see Eq. (66). Furthermore, the probability that $\Delta C(t) \geq \Theta_2 - \Theta_1$ is time-independent and can be obtained from Eq. (79) and expressed in terms of the error function Erf as follows ($\Delta\Theta = \Theta_2 - \Theta_1$):

$$P_1(\Delta C \geq \Theta_2 - \Theta_1) = \frac{1}{2} \left[1 - \text{Erf} \left(\frac{\sqrt{\text{SNR}}}{2} \Delta\Theta \right) \right]. \quad (80)$$

Next, to determine the logical X , Z and Y error rates for small T_c , we need to find those harmful two-qubit errors where the first error only affects two stabilizer generators and the second error only changes one of those affected stabilizer generators. Using Eq. (9), we find that

the single-qubit errors that can produce logical errors according to scenario one are $E = X_4, X_5$ and X_6 , so the logical X error rate is given by (from Eqs. (74) and (80))

$$\gamma_X^{\text{scn-1}} = \left(\Gamma_X^{(4)} + \Gamma_X^{(5)} + \Gamma_X^{(6)} \right) \left[1 - \text{Erf} \left(\frac{\sqrt{\text{SNR}}}{2} \Delta\Theta \right) \right]. \quad (81)$$

The X_4, X_5 and X_6 errors simultaneously affect the cross-correlators $\mathcal{C}_z^{(1)}(t)$ and $\mathcal{C}_z^{(2)}(t)$. A sufficiently large positive fluctuation in either of them will make our continuous QEC algorithm detect two false errors: first X_1, X_2 or X_3 (if the large fluctuation occurs in $\mathcal{C}_z^{(1)}$), followed by X_7, X_8 or X_9 (when the large fluctuation disappears and both Z cross-correlators fluctuate around -1), or *vice versa*. From Table II we see that the product of two false errors, e.g., $X_1 X_7 \sim Q_5$ (here “ \sim ” indicates equivalence modulo gauge operators), maps the system state from the code space to the error subspace (in this example, \mathcal{Q}_5) and does not affect the logical state (α, β) . However, the actual error, in this example $E \sim Q_5 X_L$, includes a logical X operation. This discrepancy is the source of logical errors in the small T_c limit. The above analysis shows that this is due to the noise from the continuous measurements.

From the $X - Z$ symmetry of the nine-qubit Bacon-Shor code, the logical Z error rate due to large fluctuations, according to scenario one, is then given by

$$\gamma_Z^{\text{scn-1}} = \left(\Gamma_Z^{(2)} + \Gamma_Z^{(5)} + \Gamma_Z^{(8)} \right) \left[1 - \text{Erf} \left(\frac{\sqrt{\text{SNR}}}{2} \Delta\Theta \right) \right]. \quad (82)$$

There are no harmful two-qubit errors that can be enacted by the combination of a Y error and a large fluctuation in one of the affected cross-correlators by such Y error, so for scenario one we have

$$\gamma_Y^{\text{scn-1}} = 0. \quad (83)$$

Scenario 2: We now discuss the second likely scenario in which large fluctuations in the cross-correlators lead to logical errors. In this scenario, we have a single-qubit error E that affects one, two or three stabilizer generators at the same time and the cross-correlators that are affected by the error do not undergo large fluctuations. A logical error can occur if, at the moment when these cross-correlators cross the lower error threshold $(1 - \Theta_2)$, some of the other cross-correlators (unaffected by the error E) are below this error threshold, due to a negative large fluctuation of magnitude larger than Θ_2 . We consider below the situation where a large fluctuation only occurs in one cross-correlator, since this situation is the most likely. This scenario is somewhat similar to the situation shown in Fig. 5 (a), with the important difference that now the drop of $C_2(t)$ is due to a large fluctuation and not due to a physical error.

Naively speaking, the probability that this scenario occurs in an experimental realization is given by

$$P_{\text{scn-2}} = \Gamma_E T_{\text{op}} P_2(C_2 \leq 1 - \Theta_2), \quad (84)$$

where the last factor is the probability that $C_2(t) \leq 1 - \Theta_2$. The stochastic process $C_2(t)$ is stationary since it is not affected by the actual error; its probability distribution function is obtained from Eq. (76) with $s_2 = 1$, and reads as

$$P_{2,\text{st}}(C_2) = \left[\frac{\text{SNR}}{2\pi} \right]^{1/2} \exp \left(-\frac{\text{SNR}}{2} (C_2 - 1)^2 \right). \quad (85)$$

The probability that C_2 is below the lower error threshold can then be expressed as

$$P_2(C_2 \leq 1 - \Theta_2) = \frac{1}{2} \left[1 - \text{Erf} \left(\sqrt{\frac{\text{SNR}}{2}} \Theta_2 \right) \right]. \quad (86)$$

The logical error rates for this scenario are now given by (from Eqs. (84) and (86))

$$\begin{aligned} \gamma_X^{\text{scn-2}} = & \frac{1}{2} \left(\Gamma_X^{(1)} + \Gamma_X^{(2)} + \Gamma_X^{(3)} + \Gamma_X^{(7)} + \Gamma_X^{(8)} + \Gamma_X^{(9)} + \right. \\ & \left. \Gamma_Y^{(1)} + \Gamma_Y^{(2)} + \Gamma_Y^{(3)} + \Gamma_Y^{(7)} + \Gamma_Y^{(8)} + \Gamma_Y^{(9)} \right) \times \\ & \left[1 - \text{Erf} \left(\sqrt{\frac{\text{SNR}}{2}} \Theta_2 \right) \right], \end{aligned} \quad (87)$$

$$\begin{aligned} \gamma_Z^{\text{scn-2}} = & \frac{1}{2} \left(\Gamma_Z^{(1)} + \Gamma_Z^{(4)} + \Gamma_Z^{(7)} + \Gamma_Z^{(3)} + \Gamma_Z^{(6)} + \Gamma_Z^{(9)} + \right. \\ & \left. \Gamma_Y^{(1)} + \Gamma_Y^{(4)} + \Gamma_Y^{(7)} + \Gamma_Y^{(3)} + \Gamma_Y^{(6)} + \Gamma_Y^{(9)} \right) \times \\ & \left[1 - \text{Erf} \left(\sqrt{\frac{\text{SNR}}{2}} \Theta_2 \right) \right], \end{aligned} \quad (88)$$

$$\gamma_Y^{\text{scn-2}} = 0. \quad (89)$$

The errors that contribute to the logical X error rate are $E = \{X_1, X_2, X_3, X_7, X_8, X_9, Y_1, Y_2, Y_3, Y_7, Y_8, Y_9\}$. From these errors, the X errors only affect one stabilizer generator: this is (i) $S_z^{(1)}$ if $E = \{X_1, X_2, X_3\}$, or (ii) $S_z^{(2)}$ if $E = \{X_7, X_8, X_9\}$. Then a large fluctuation in the cross-correlator $\mathcal{C}_z^{(2)}(t)$ or $\mathcal{C}_z^{(1)}(t)$, respectively, leads to a logical X error, see Fig. 6. The two false errors detected by our QEC protocol are (i) $E_{1,\text{false}} = \{X_4, X_5$ or $X_6\}$ (when both Z cross-correlators are below the lower error threshold) and $E_{2,\text{false}} = \{X_7, X_8$ or $X_9\}$ (when large fluctuation disappears) if the error that has actually occurred is $E = \{X_1, X_2, X_3\}$, or (ii) $E_{1,\text{false}} = \{X_4, X_5$ or $X_6\}$ and $E_{2,\text{false}} = \{X_1, X_2$ or $X_3\}$ if $E = \{X_7, X_8$ and $X_9\}$. For $E = \{X_1, X_2, X_3\}$, a logical X error arises due to the discrepancy between the actual error $E \sim Q_4$, which does not include a logical X operation, while the product of the two false errors is, e.g., $E_{1,\text{false}} E_{2,\text{false}} = X_4 X_7 \sim Q_4 X_L$ (obtained from Tables II and III), which does include a logical X operation. A

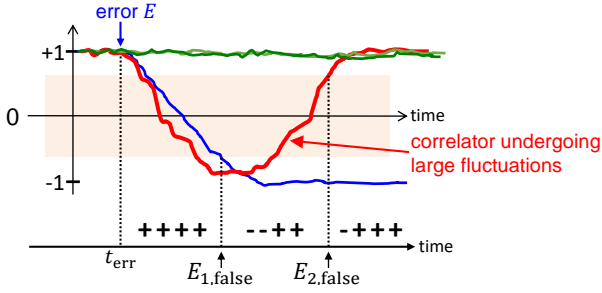


FIG. 6. Large fluctuations in cross-correlators leading to logical errors. This situation corresponds to scenario 2 of the main text. Actual error E only affects the blue cross-correlator and large fluctuations are only present in the red cross-correlator. The other cross-correlators are depicted by the green lines. Our QEC protocol detects two false errors ($E_{1,\text{false}}$ and $E_{2,\text{false}}$) from the indicated error syndrome patterns. Shaded area is the “syndrome uncertainty region”.

similar discrepancy exists for the other errors $E = \{X_7, X_8, X_9\}$ that also lead to logical X errors.

In contrast, the Y errors that contribute to the logical X error rate (87) affect two [if the error that has occurred is $E = Y_1, Y_3, Y_7, Y_9$] or three [if actual error is $E = Y_2, Y_8$] stabilizer generators at the same time. In this situation, a large fluctuation in $\mathcal{C}_z^{(2)}(t)$ when $E = \{Y_1, Y_2, Y_3\}$ or in $\mathcal{C}_z^{(1)}(t)$ when $E = \{Y_7, Y_8, Y_9\}$, leads to a logical X error as well. For example, let us consider the case where the actual error is $E = Y_2$, which affects three cross-correlators; specifically, $\mathcal{C}_x^{(1)}(t)$, $\mathcal{C}_x^{(2)}(t)$ and $\mathcal{C}_z^{(1)}(t)$. A sufficiently large negative fluctuation in $\mathcal{C}_z^{(2)}(t)$ will make our continuous QEC algorithm detect two false errors: first Y_5 and second X_7, X_8 or X_9 . The product of the two false errors is equivalent to $\sim Q_{11}Y_L$ (however, the

actual error is $Y_2 \sim Q_{11}Z_L$). Our continuous QEC protocol then says that the system state is in error subspace \mathcal{Q}_{11} and the logical state suffers from a logical Y operation. Before extracting the logical state (with initial probability amplitudes α, β) from this error subspace we apply the multi-qubit operation $X_1X_4X_7Z_1Z_2Z_3$ to the nine-qubit system to undo such apparent logical Y operation; however, this procedure changes the actual logical state from $Z_L(\alpha, \beta)$ to $Y_LZ_L(\alpha, \beta) = \iota X_L(\alpha, \beta) = \iota(\beta, \alpha)$. The extracted logical state from the error subspace \mathcal{Q}_{11} is then $(\alpha_f, \beta_f) = (\beta, \alpha)$, dropping overall phase factors. A logical X error has therefore arisen. Similarly, the other Y errors lead to a logical X error as well.

The logical X error rate in the small T_c limit is given by $\gamma_X^{\text{cont}} = \gamma_X^{\text{scn-1}} + \gamma_X^{\text{scn-2}}$, with a similar relation for the logical Z error rate. The scenarios discussed above do not contribute to the logical Y error rate in this limit. This does not mean that the latter error vanishes. However, it is exponentially smaller than the logical X and Z error rates so it can be neglected. The total logical error rate γ_{cont} for the depolarizing channel in the small T_c regime is then equal to

$$\gamma_{\text{cont}} \approx 2\gamma_X^{\text{cont}} = 2\gamma_Z^{\text{cont}} = 2\Gamma_d \left[1 - \text{Erf} \left(\frac{\sqrt{\text{SNR}}}{2} \Delta\Theta \right) \right] + 4\Gamma_d \left[1 - \text{Erf} \left(\sqrt{\frac{\text{SNR}}{2}} \Theta_2 \right) \right]. \quad (90)$$

IV. OPTIMAL CONTINUOUS QEC PROTOCOL

Our analytical result for the total logical error rate γ_{cont} is now obtained from the sum of Eqs. (73) and (90). This yields ($\Delta\Theta = \Theta_2 - \Theta_1$)

$$\gamma_{\text{cont}} = \frac{112}{9} T_c \Gamma_d^2 \ln \left[\frac{2 - \Theta_1}{2 - \Theta_2} \right] + \frac{284}{9} T_c \Gamma_d^2 \ln \left[\frac{2}{2 - \Theta_2} \right] + 2\Gamma_d \left[1 - \text{Erf} \left(\frac{\sqrt{\text{SNR}}}{2} \Delta\Theta \right) \right] + 4\Gamma_d \left[1 - \text{Erf} \left(\sqrt{\frac{\text{SNR}}{2}} \Theta_2 \right) \right]. \quad (91)$$

Figure 7 compares our analytical formula of Eq. (91) against Monte Carlo simulations for the continuous operation of the nine-qubit Bacon-Shor code under perfect measurement efficiency $\eta = 1$. In these simulations, the continuous measurements were described using Eq. (23) for the evolution of the gauge qubits and Eq. (26) to obtain the measurement signals $I_{G_k}(t)$. Decoherence due to X, Y and Z errors was accounted for using the jump/no-jump method (Section II C), with the action of errors on the system state specified by Tables II and III. We employ the following parameter values: depolarization error rate $\Gamma_d = 3 \times 10^{-5} \tau_{\text{coll}}^{-1}$ (the same for all qubits), error thresholds at $1 - \Theta_1 = 0.56$ and $1 - \Theta_2 = -0.56$, and

$\eta = 1$ (ideal detectors).

We find that the total logical X and Z error rates are quite similar (we show only the average and not the individual values), which agrees with the theoretical prediction that $\gamma_X^{\text{cont}} = \gamma_Z^{\text{cont}}$. This is due to the $X - Z$ symmetry of the nine-qubit Bacon-Shor code and the fact that all qubits have the same error rates. The logical Y error rate is roughly five times smaller than the logical X and Z error rates for large values of T_c (it was not possible to reliably obtain γ_Y^{cont} for $T_c \leq 15\tau_{\text{coll}}$ because the value was too small). In general, we find good agreement, without any fitting parameters, between analytics and numerics for the range $T_c \geq 10\tau_{\text{coll}}$. Most impor-

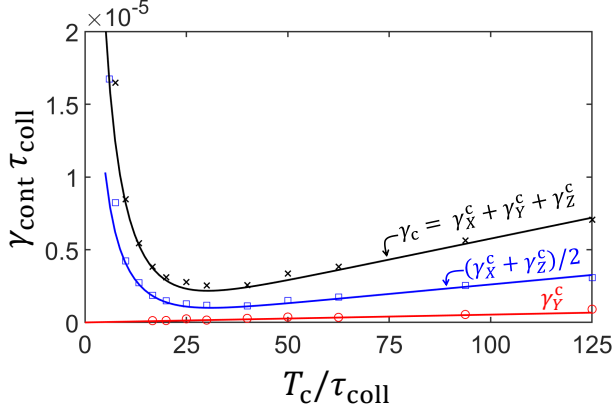


FIG. 7. Analytical *vs.* numerical results for the logical error rates as function of the integration time parameter T_c . Circles indicate the numerical results for the logical Y error rates; squares show numerical results for the average of the logical X and Z error rates; and crosses indicate the numerical results for the total logical error rate γ_{cont} . Solid lines show the analytical results. Parameters: $1 - \Theta_1 = 0.56$, $1 - \Theta_2 = -0.56$, $\Gamma_d = 3 \times 10^{-5} \tau_{\text{coll}}^{-1}$, $\eta = 1$ and $\tau_c = 0.25 \tau_{\text{coll}} \approx \tau_c^{\text{opt}}$. There are no fitting parameters.

tantly, our analytical result Eq. (91) is able to estimate the optimal value of the integration time parameter T_c : for the assumed parameters in the simulations we find $T_c \simeq 30 \tau_{\text{coll}}$.

Next, we use Eq. (91) to find the optimal operation point $(\Theta_1^{\text{opt}}, \Theta_2^{\text{opt}}, T_c^{\text{opt}})$ for the continuous operation of the nine-qubit Bacon-Shor code by minimizing the total logical error rate γ_{cont} . In this minimization we impose the constraint $\Theta_1 \geq \Theta_{1,\text{min}}$ (i.e., the upper error threshold should not be too close to +1) and choose $\Theta_{1,\text{min}} = 1.5 \text{SNR}^{-1/2}$, where $\text{SNR}^{-1/2}$ is the standard deviation of the (normalized) cross-correlator fluctuations in the absence of errors. Equation (86) then implies that the probability that a cross-correlator is within the “syndrome uncertainty region” is roughly 6.68%. This constraint guarantees that single-qubit errors are efficiently detected, since their detection requires that the cross-correlators that are unaffected by the errors are above the upper error threshold (i.e., outside the “syndrome uncertainty region”). Moreover, it also guarantees that the window time intervals $\Delta t_{\text{cont}}^{(n)}$, $n = 1, 2$ that were obtained in the noiseless limit in Section III D 1, are approximately correct.

Minimization of the total logical error rate formula (91) with the above constraint for Θ_1 is carried out numerically. We first discuss our results for the case of ideal detectors ($\eta = 1$). We find that $\Theta_1^{\text{opt}} = \Theta_{1,\text{min}}$ (i.e., the optimal position of the upper error threshold is as high as allowed by the above constraint), $\Theta_2^{\text{opt}} \approx 1.40$ (so the optimal position of the lower error threshold is $1 - \Theta_2^{\text{opt}} \approx -0.40$ and is weakly dependent on Γ_d with deviations ± 0.0075 from this constant value). Fig. 8 shows plots of the values of T_c^{opt} and $\gamma_{\text{cont}}^{\text{opt}}$ as a function of

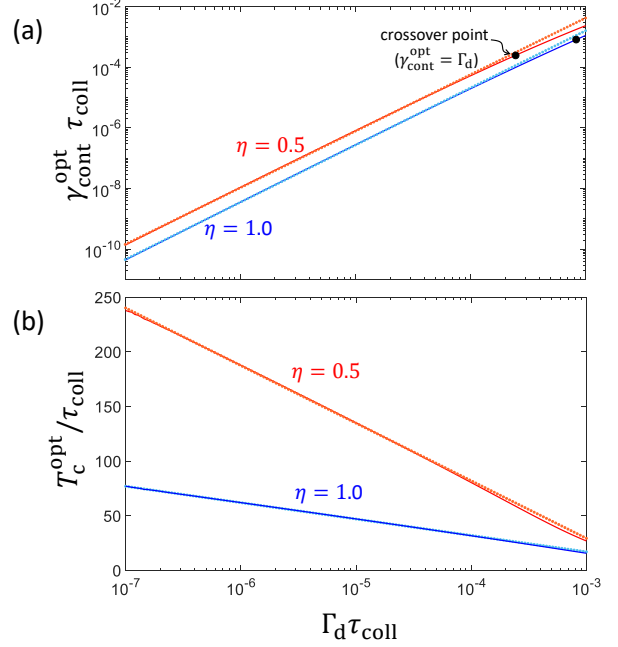


FIG. 8. Optimized logical error rate $\gamma_{\text{cont}}^{\text{opt}}$ for the continuous operation and optimal integration time parameter T_c^{opt} as function of the depolarization error rate Γ_d and for two values of quantum efficiency $\eta = 0.5$ and $\eta = 1.0$. Solid lines are obtained from minimization of the total logical error rate formula (91) and dotted lines show the fitting formulas Eqs. (93) and (97) (top panel) and Eqs. (92) and (96) (bottom panel). The small circles in panel (a) indicate the crossover points for Γ_d , cf. Eqs. (94) and (98).

$\Gamma_d \tau_{\text{coll}} \in [10^{-7}, 10^{-4}]$ for the optimal values $\Theta_1^{\text{opt}}, \Theta_2^{\text{opt}}$, where the blue lines refer to the ideal detector $\eta = 1$. Fitting these two functions to a simple log function (T_c^{opt}) or power law ($\gamma_{\text{cont}}^{\text{opt}}$), results in the fully optimized formulae

$$T_c^{\text{opt}} \approx -6.51 \ln(72.71 \Gamma_d \tau_{\text{coll}}) \tau_{\text{coll}}, \quad (92)$$

$$\gamma_{\text{cont}}^{\text{opt}} \approx \frac{739.60}{\tau_{\text{coll}}} (\Gamma_d \tau_{\text{coll}})^\nu, \quad \text{with } \nu = 1.88. \quad (93)$$

We find that these fitting formulae also work well for smaller values of Γ_d .

The fact that the optimized logical error rate, $\gamma_{\text{cont}}^{\text{opt}}$, for the continuous operation exhibits a power law scaling on Γ_d (for sufficiently small Γ_d) with exponent $\nu = 1.88$ close to 2, which is the expected exponent for a distance-three quantum error correcting code, suggests that our continuous QEC protocol performs well. By equating $\gamma_{\text{cont}}^{\text{opt}}$ and Γ_d , we estimate the crossover value of the depolarization error rate, $\Gamma_d^{\text{crossover}}$, below which implementation of the nine-qubit Bacon-Shor code is advantageous. This results in the value

$$\Gamma_d^{\text{crossover}} \approx 10^{-3} \tau_{\text{coll}}^{-1} \quad (\eta = 1). \quad (94)$$

Moreover, from Eqs. (16) and (93), we find the relationship between the cycle time Δt and the collapse time

τ_{coll} such that the continuous and discrete QEC operations have the same performances, i.e., $\gamma_{\text{cont}}^{\text{opt}} = \gamma_{\text{discrete}}$. This yields

$$\Delta t \approx \frac{33.61\tau_{\text{coll}}}{(\Gamma_{\text{d}}\tau_{\text{coll}})^{2-\nu}} \quad (\eta = 1). \quad (95)$$

We now discuss the case of nonideal detectors with $\eta = 0.5$. Numerical optimization of Eq. (91) yields the optimal parameters $\Theta_1^{\text{opt}} = \Theta_{1,\text{min}}$, $\Theta_2^{\text{opt}} \approx 1.40$ (this is weakly dependent on Γ_{d} with deviations ± 0.012 from this constant value). Similarly fitting the corresponding results over the range $\Gamma_{\text{d}}\tau_{\text{coll}} \in [10^{-7}, 10^{-4}]$ (red lines in Fig. 8) results in the corresponding formulae for the optimal integration time and logical error rate for $\eta = 0.5$:

$$T_{\text{c}}^{\text{opt}} \approx -22.88 \ln(277.27 \Gamma_{\text{d}}\tau_{\text{coll}}) \tau_{\text{coll}}, \quad (96)$$

$$\gamma_{\text{cont}}^{\text{opt}} \approx \frac{1690.4}{\tau_{\text{coll}}} (\Gamma_{\text{d}}\tau_{\text{coll}})^{\tilde{\nu}} \quad \text{with } \tilde{\nu} = 1.86. \quad (97)$$

The scaling of the logical error result in Eq. (97) shows that our continuous QEC protocol also performs well in the case of nonideal detectors, since the exponent $\tilde{\nu}$ is still close to the ideal value of 2. The crossover value of the depolarization error rate is now smaller than that of the ideal case, which is not surprising given the effect of the measurement inefficiency. Specifically, for $\eta = 0.5$, we find

$$\Gamma_{\text{d}}^{\text{crossover}} \approx 0.2 \times 10^{-3} \tau_{\text{coll}}^{-1} \quad (\eta = 0.5). \quad (98)$$

Moreover, continuous and discrete operations exhibit the same performances for inefficiency $\eta = 0.5$ if the cycle time Δt from discrete operation and the collapse time τ_{coll} from continuous measurements are related by Eq. (95) with the numerical pre-factor equal to 76.83 and ν replaced by $\tilde{\nu}$. We conclude that discrete and continuous operation performances of the nine-qubit Bacon-Shor code can indeed be comparable.

V. SUMMARY AND CONCLUSIONS

We have analyzed the continuous operation of the error correcting nine-qubit Bacon Shor code, in which all non-commuting gauge operators are continuously measured at the same time. Our analysis has shown that continuous operation of the nine-qubit Bacon-Shor code is not only possible, but that it can have a performance that is comparable to that of the conventional operation, i.e., enforcing a near quadratic scaling of logical errors, while avoiding the use of ancilla qubits and associated circuits to transfer and diagnose errors. Instead, the errors are passively monitored, e.g., by probe electromagnetic fields as is commonly implemented for superconducting qubits in microwave cavities.

Our approach exploits the subsystem structure of the nine-qubit Bacon-Shor code to parametrize the full quantum state in terms of the probability amplitudes of one

logical qubit and four gauge qubits. This parametrization is very useful in the analysis of the continuous operation, because it enables us to describe the measurement-induced evolution of the nine-qubit state in terms of an effective evolution of only the gauge qubits. The latter are subject to simultaneous continuous measurement of the effective noncommuting operators \mathcal{G}_k that act only on these qubits). The effective quantum measurement model for the gauge qubits is also useful to describe the temporal correlations of the actual measurement signals from simultaneous continuous measurement of the gauge operators G_k . In this way, our approach reduces the complexity of the problem from nine physical to four effective qubits.

Due to the continuous measurement of noncommuting operators, the gauge qubits undergo diffusive state evolution in both the code space and the error subspaces. Occurrence of an error interrupts the evolution of the gauge qubits in one of these subspaces and moves it to another one, where diffusion continues until the next error occurs. We developed a general procedure to figure out which subspace the logical and gauge qubits jump to after an error (Tables II and III) and also to describe how the logical state and the state of the gauge qubits are affected by the errors at the moment of the jump (Table II). This procedure can be easily extended to the error analysis of other subsystem codes.

Our continuous QEC protocol for quantum memory consists of passively monitoring errors while also diagnosing their associated logical operations (obtained from Table II) and recording these, followed by a set of discrete recovery operations that undo the series of logical operations that have occurred during a single realization at the end of the continuous operation, before the logical state is returned to the user. We showed that the single qubit errors (modulo gauge operators) can be inferred from the error syndrome path $\mathcal{S}(t)$, which is defined by the measured values of the stabilizer generators, and that knowledge of $\mathcal{S}(t)$ is sufficient to determine the entire series of logical operations in a single realization, and hence the required final sequence of recovery operations. To monitor the stabilizer generators in real time, we introduced cross-correlators of three measurement signals, defined using time averaging with two integration time parameters τ_{c} and T_{c} . Analytic estimates of the size of the fluctuations of the cross-correlators, characterized by their SNR, were used to find the optimal value of the filter integration time τ_{c} that maximizes the SNR.

In order to realize this protocol, it will be necessary to implement continuous measurements of both XX and ZZ operators either simultaneously or with fast alternation. Continuous measurement of ZZ operators has been experimentally demonstrated with superconducting (SC) qubits in Ref. [51], where the two qubits were dispersively coupled with a single mode of a cavity to generate an interaction Hamiltonian $H_{\text{int}} = \chi(Z_1 + Z_2)n$, where χ is the dispersive coupling parameter and n the intracavity photon number operator. Under suitable conditions

($\chi \ll \kappa$, with κ the cavity decay rate, and the cavity drive frequency set at the average of the resonance frequencies of the four two-qubit states), this results in an effective measurement of ZZ . Such dispersive multi-qubit measurements are now being made in multiple laboratories [67–69]. In principle, continuous measurement of XX could be made by combining this approach with that of Vool *et al.* in Ref. [70], which shows how to engineer continuous measurements of X for a single qubit. Combining these two approaches would allow a continuous measurement of XX to be made. Implementing both of these simultaneously could be realized by generalization of the single quadrature measurement scheme of Ref. [52], which implemented simultaneous X and Z measurements on a single qubit. This will require coupling to two cavity modes and driving of sideband transitions on the two-qubit levels. Analysis of the details of this scheme present an interesting challenge for future work.

A key feature of our QEC protocol is a double error-threshold protocol (with error threshold parameters Θ_1 and Θ_2) that is employed to obtain the monitored error syndrome path $\mathcal{S}_m(t)$ from the measured stabilizer cross-correlators. We showed how, in general, $\mathcal{S}_m(t)$ can differ from the actual error syndrome path $\mathcal{S}(t)$ by the occurrence of jumps in $\mathcal{S}(t)$ that are missing in $\mathcal{S}_m(t)$ or *vice versa*, resulting in inference of a different series of logical operations from the measured $\mathcal{S}_m(t)$ than from the true $\mathcal{S}(t)$, and identified this discrepancy as the source of logical errors in the continuous QEC protocol.

We derived analytical expressions for the logical X , Y and Z error rates in the continuous QEC protocol for the limiting situations of small and large correlator integration times T_c . The analytical results are used to find the optimal values of the parameters (T_c , Θ_1 and Θ_2) for the continuous QEC protocol by minimization of the total logical error rate. The analytical formulae for the logical error rates are seen to agree well with Monte Carlo simulations undertaken with the optimized parameters. This analysis also allowed us to identify the most likely processes contributing to logical errors in these two limits. In the small T_c limit, we have identified the most likely process for logical errors to be the misinterpretation of a single jump in $\mathcal{S}(t)$ produced by an actual error as two false jumps in $\mathcal{S}_m(t)$ that are diagnosed as two false errors. This particular mechanism of logical errors is unique to the continuous operation; it does not arise in the conventional operation of the Bacon-Shor code with ideal projective measurements because of the absence of measurement noise. In the large T_c limit, fluctuations in the correlators can be neglected and the main mechanism of logical errors derives then from two errors that are misdiagnosed as a single error by the protocol. This can happen when two errors occur sufficiently close in time, which is now similar to the mechanism for logical errors in the conventional discrete operation of the Bacon-Shor code, in which two errors occurring within the same operation cycle produce a logical error.

A primary result of this work is the determination of

the optimized total logical error rate, $\gamma_{\text{cont}}^{\text{opt}}$, for the continuous operation of a nine-qubit Bacon-Shor code. We found that $\gamma_{\text{cont}}^{\text{opt}}$ exhibits a power-law dependence on the depolarization error rate Γ_d , with an exponent ≈ 1.9 that only weakly depends on the quantum efficiency. The fact that this exponent is close to the expected value of 2 for a distance-three quantum error correcting code shows that the continuous QEC protocol performs well.

By comparing $\gamma_{\text{cont}}^{\text{opt}}$ with γ_{discrete} (total logical error rate for the discrete operation), we find that the discrete and continuous operations exhibit comparable performances when the discrete cycle time Δt is approximately 30 times (if $\eta = 1$) or 80 times (if $\eta = 0.5$) the collapse time τ_{coll} of the continuous operation. This does not indicate that the discrete operation is faster or better than the continuous operation if we take into account that “projective measurements” actually take time to realize, require additional overhead (e.g., application of relatively strong pulses to read out the ancillary qubits) and introduce non-correctable errors at the ancillary qubits. We point out that the value of the ratio $\Delta t/\tau_{\text{coll}}$ that is necessary for comparable performance of the discrete and continuous operations is generally larger when the triple cross-correlator signals, Eq. (33), are noisier, for example, due to inefficient detectors.

Finally, we have estimated the crossover value of the qubit error rate Γ_d , below which implementation of the nine-qubit Bacon-Shor code is advantageous in terms of effectiveness, i.e., $\gamma_{\text{cont}}^{\text{opt}} < \Gamma_d$. For ideal detectors, we found $\Gamma_d^{\text{crossover}} \approx 10^{-3}\tau_{\text{coll}}^{-1}$, while for nonideal detectors $\Gamma_d^{\text{crossover}}$ is approximately five times smaller. Assuming $\Gamma_d^{\text{crossover}} = (500 \mu\text{s})^{-1}$ [71], we then obtain that the collapse time of the continuous operation should be $\tau_{\text{coll}} \approx 0.5 \mu\text{s}$ in the ideal case or smaller in the nonideal case ($\eta < 1$).

VI. ACKNOWLEDGMENTS

The research is based upon work supported by the Office of the Director of National Intelligence (ODNI), Intelligence Advanced Research Projects Activity (IARPA), via the U.S. Army Research Office contract W911NF-17-C-0050. The views and conclusions contained herein are those of the authors and should not be interpreted as necessarily representing the official policies or endorsements, either expressed or implied, of the ODNI, IARPA, or the U.S. Government. The U.S. Government is authorized to reproduce and distribute reprints for Governmental purposes notwithstanding any copyright annotation thereon.

Appendix A: Code space orthonormal basis and nominal collapse states for X gauge operators

1. Code space orthonormal basis

In this section we describe the procedure to obtain the 32 orthonormal basis vectors $|\phi_j\rangle$, explicitly given in Eq. (3), that span the code space. The first 16 basis vectors can be obtained as follows. We start with the initial state $|000\,000\,000\rangle$ and apply the projector

$$\begin{aligned} \Pi_{\text{step1}}^{(g_1 g_2 g_3, g_4 g_5 g_6)} &= \left(\frac{\mathbb{1} + g_1 G_1}{2}\right) \left(\frac{\mathbb{1} + g_2 G_2}{2}\right) \left(\frac{\mathbb{1} + g_3 G_3}{2}\right) \\ &\quad \times \left(\frac{\mathbb{1} + g_4 G_4}{2}\right) \left(\frac{\mathbb{1} + g_5 G_5}{2}\right) \left(\frac{\mathbb{1} + g_6 G_6}{2}\right), \quad (\text{A1}) \end{aligned}$$

where g_1, g_2, \dots, g_6 are outcomes of the Z gauge operators G_1, G_2, \dots, G_6 , respectively, and then apply the projector

$$\begin{aligned} \Pi_{\text{step2}}^{(g_7 g_8 g_9, g_{10} g_{11} g_{12})} &= \left(\frac{\mathbb{1} + g_7 G_7}{2}\right) \left(\frac{\mathbb{1} + g_8 G_8}{2}\right) \left(\frac{\mathbb{1} + g_9 G_9}{2}\right) \\ &\quad \times \left(\frac{\mathbb{1} + g_{10} G_{10}}{2}\right) \left(\frac{\mathbb{1} + g_{11} G_{11}}{2}\right) \left(\frac{\mathbb{1} + g_{12} G_{12}}{2}\right), \quad (\text{A2}) \end{aligned}$$

where g_7, g_8, \dots, g_{12} are the outcomes of the X gauge operators G_7, G_8, \dots, G_{12} , respectively. The outcomes g_i that should be used in Eqs. (A1)–(A2) correspond to any “good” outcome configuration that satisfy $g_1 g_2 g_3 = g_4 g_5 g_6 = 1$ or $g_7 g_8 g_9 = g_{10} g_{11} g_{12} = 1$; we will use $g_1, \dots, g_{12} = 1$. Next, the sought basis vectors are obtained by applying the step-1 projectors that correspond to all 16 “good” outcome configurations (\pm indicates ± 1)

$$\begin{aligned} |\phi_1\rangle &= \mathcal{N}_1^{-1} \Pi_{\text{step1}}^{(++++,++++)} |000\,000\,000\rangle_{++}, \\ |\phi_2\rangle &= \mathcal{N}_2^{-1} \Pi_{\text{step1}}^{(++++,+---)} |000\,000\,000\rangle_{++}, \\ |\phi_3\rangle &= \mathcal{N}_3^{-1} \Pi_{\text{step1}}^{(++++,---+)} |000\,000\,000\rangle_{++}, \\ |\phi_4\rangle &= \mathcal{N}_4^{-1} \Pi_{\text{step1}}^{(++++,-+-+)} |000\,000\,000\rangle_{++}, \end{aligned}$$

$$\begin{aligned} |\phi_5\rangle &= \mathcal{N}_5^{-1} \Pi_{\text{step1}}^{(+---,++++)} |000\,000\,000\rangle_{++}, \\ |\phi_6\rangle &= \mathcal{N}_6^{-1} \Pi_{\text{step1}}^{(+---,+---)} |000\,000\,000\rangle_{++}, \\ |\phi_7\rangle &= \mathcal{N}_7^{-1} \Pi_{\text{step1}}^{(+---,---+)} |000\,000\,000\rangle_{++}, \\ |\phi_8\rangle &= \mathcal{N}_8^{-1} \Pi_{\text{step1}}^{(+---,-+-+)} |000\,000\,000\rangle_{++}, \\ |\phi_9\rangle &= \mathcal{N}_9^{-1} \Pi_{\text{step1}}^{(----,++++)} |000\,000\,000\rangle_{++}, \\ |\phi_{10}\rangle &= \mathcal{N}_{10}^{-1} \Pi_{\text{step1}}^{(----,+---)} |000\,000\,000\rangle_{++}, \\ |\phi_{11}\rangle &= \mathcal{N}_{11}^{-1} \Pi_{\text{step1}}^{(----,---+)} |000\,000\,000\rangle_{++}, \\ |\phi_{12}\rangle &= \mathcal{N}_{12}^{-1} \Pi_{\text{step1}}^{(----,-+-+)} |000\,000\,000\rangle_{++}, \\ |\phi_{13}\rangle &= \mathcal{N}_{13}^{-1} \Pi_{\text{step1}}^{(----,++++)} |000\,000\,000\rangle_{++}, \\ |\phi_{14}\rangle &= \mathcal{N}_{14}^{-1} \Pi_{\text{step1}}^{(---+,+---)} |000\,000\,000\rangle_{++}, \\ |\phi_{15}\rangle &= \mathcal{N}_{15}^{-1} \Pi_{\text{step1}}^{(---+,---+)} |000\,000\,000\rangle_{++}, \\ |\phi_{16}\rangle &= \mathcal{N}_{16}^{-1} \Pi_{\text{step1}}^{(---+,-+-+)} |000\,000\,000\rangle_{++}, \quad (\text{A3}) \end{aligned}$$

where \mathcal{N}_j are normalization factors and

$$|000\,000\,000\rangle_{++} = \Pi_{\text{step2}}^{(++++,++++)} \Pi_{\text{step1}}^{(++++,++++)} |000\,000\,000\rangle. \quad (\text{A4})$$

The remaining basis vectors $|\phi_{17}\rangle, \dots, |\phi_{32}\rangle$ are obtained from Eqs. (A3)–(A4) with initial state $|000\,000\,000\rangle$ replaced by $|111\,111\,111\rangle$.

2. Nominal collapse states after projective measurement of X gauge operators

In Section II B we introduced $|X g_7 g_8 g_9, g_{10} g_{11} g_{12}\rangle$ as the nominal collapse states after step-2 measurements with “good” outcomes, satisfying $g_7 g_8 g_9 = g_{10} g_{11} g_{12} = +1$. These collapse states can be written as a linear combination of all nominal step-1 collapse states, given in Eq. (4), with coefficients $\pm 1/4$. The unitary transformation U that relates them reads as

$$U = \frac{1}{4} \begin{bmatrix} 1 & 1 & 1 & 1 & 1 & 1 & 1 & 1 & 1 & 1 & 1 & 1 & 1 & 1 & 1 \\ 1 & -1 & 1 & -1 & 1 & -1 & 1 & -1 & 1 & -1 & 1 & -1 & 1 & -1 & 1 \\ 1 & 1 & 1 & 1 & -1 & -1 & -1 & -1 & 1 & 1 & 1 & 1 & -1 & -1 & -1 \\ 1 & -1 & 1 & -1 & -1 & 1 & -1 & 1 & 1 & -1 & 1 & -1 & -1 & 1 & -1 \\ 1 & 1 & -1 & -1 & 1 & 1 & -1 & -1 & 1 & 1 & -1 & -1 & 1 & 1 & -1 \\ 1 & -1 & -1 & 1 & 1 & -1 & -1 & 1 & 1 & -1 & -1 & 1 & 1 & -1 & -1 \\ 1 & 1 & -1 & -1 & -1 & -1 & 1 & 1 & 1 & 1 & -1 & -1 & -1 & 1 & 1 \\ 1 & -1 & -1 & 1 & -1 & 1 & 1 & -1 & 1 & -1 & -1 & 1 & -1 & 1 & -1 \\ 1 & 1 & 1 & 1 & 1 & 1 & 1 & 1 & -1 & -1 & -1 & -1 & -1 & -1 & -1 \\ 1 & -1 & 1 & -1 & 1 & -1 & 1 & -1 & -1 & 1 & -1 & 1 & -1 & 1 & -1 \\ 1 & 1 & 1 & 1 & -1 & -1 & -1 & -1 & -1 & -1 & -1 & 1 & 1 & 1 & 1 \\ 1 & -1 & 1 & -1 & -1 & 1 & -1 & 1 & -1 & 1 & -1 & 1 & 1 & -1 & 1 \\ 1 & 1 & -1 & -1 & 1 & 1 & -1 & -1 & -1 & -1 & 1 & 1 & -1 & -1 & 1 \\ 1 & -1 & -1 & 1 & 1 & -1 & -1 & 1 & -1 & 1 & 1 & -1 & -1 & 1 & -1 \\ 1 & 1 & -1 & -1 & -1 & -1 & 1 & 1 & -1 & -1 & 1 & 1 & 1 & 1 & -1 \\ 1 & -1 & -1 & 1 & -1 & 1 & 1 & -1 & -1 & 1 & 1 & -1 & -1 & 1 & 1 \\ 1 & 1 & -1 & -1 & -1 & -1 & 1 & 1 & -1 & -1 & 1 & 1 & 1 & 1 & -1 \\ 1 & -1 & -1 & 1 & -1 & 1 & 1 & -1 & -1 & 1 & 1 & -1 & 1 & -1 & 1 \end{bmatrix}. \quad (\text{A5})$$

From Eq. (A5), we obtain, e.g., $|X+++ , +++\rangle = [|Z+ , +++ , +++\rangle + |Z+ , +++ , +- -\rangle + |Z+ , +++ , - - +\rangle + |Z+ , +++ , - + -\rangle + |Z+ , - - , +++\rangle + |Z+ , - - , +- -\rangle + |Z+ , - - , - - +\rangle + |Z+ , - - , - + -\rangle + |Z- , - + , +++\rangle + |Z- , - + , +- -\rangle + |Z- , - + , - - +\rangle + |Z- , - + , - + -\rangle]/4$. Note that the unitary matrix U is symmetric.

Appendix B: Harmful two-qubit errors

Here we describe the error analysis including the phase factors $\zeta_k^{(\ell)} = \pm 1$, $\zeta_X^{(\ell)} = \pm 1$ and $\zeta_Z^{(\ell)} = \pm 1$.

1. Single-qubit errors on wavefunction $|\Psi_{Q_\ell}\rangle$

Let us consider a wavefunction $|\Psi_{Q_\ell}\rangle$ parametrized according to Eq. (17). We are interested to know how the 27 single-qubit errors change the parameters of such wavefunction. The results of this section are used later to determine the harmful two-qubit errors for discrete and continuous QEC protocols of the nine-qubit Bacon-Shor code.

We start by writing the following identities for the X ,

Z and Y errors. For the former we have

$$X_1 = Q_4, \quad (\text{B1a})$$

$$X_2 = Q_4 X_{12}, \quad (\text{B1b})$$

$$X_3 = Q_4 X_{12} X_{23}, \quad (\text{B1c})$$

$$X_4 = Q_5 X_{147} X_{78} X_{89}, \quad (\text{B1d})$$

$$X_5 = Q_5 X_{147} X_{12} X_{89} S_x^{(1)}, \quad (\text{B1e})$$

$$X_6 = Q_5 X_{147} X_{12} X_{23} S_x^{(1)} S_x^{(2)}, \quad (\text{B1f})$$

$$X_7 = Q_1 X_{78} X_{89}, \quad (\text{B1g})$$

$$X_8 = Q_1 X_{89}, \quad (\text{B1h})$$

$$X_9 = Q_1, \quad (\text{B1i})$$

where $Q_1 = X_9$, $Q_4 = X_1$ and $Q_5 = X_{19}$, cf. Table I. For Z errors we have the following identities

$$Z_1 = Q_{12}, \quad (\text{B2a})$$

$$Z_2 = Q_{15} Z_{123} Z_{36} Z_{69}, \quad (\text{B2b})$$

$$Z_3 = Q_3 Z_{36} Z_{69}, \quad (\text{B2c})$$

$$Z_4 = Q_{12} Z_{14}, \quad (\text{B2d})$$

$$Z_5 = Q_{15} Z_{123} Z_{14} Z_{69} S_z^{(1)}, \quad (\text{B2e})$$

$$Z_6 = Q_3 Z_{69}, \quad (\text{B2f})$$

$$Z_7 = Q_{12} Z_{14} Z_{47}, \quad (\text{B2g})$$

$$Z_8 = Q_{15} Z_{123} Z_{14} Z_{47} S_z^{(1)} S_z^{(2)}, \quad (\text{B2h})$$

$$Z_9 = Q_3, \quad (\text{B2i})$$

where $Q_3 = Z_9$, $Q_{12} = Z_1$ and $Q_{15} = Z_{19}$, cf. Table I.

For Y errors we have

$$Y_1 = Q_8, \quad (\text{B3a})$$

$$Y_2 = -Q_{11} Z_{123} Z_{36} Z_{69} X_{12}, \quad (\text{B3b})$$

$$Y_3 = Q_7 X_{12} (iX_{23} Z_{36}) Z_{69}, \quad (\text{B3c})$$

$$Y_4 = -Q_9 X_{147} X_{78} X_{89} Z_{14}, \quad (\text{B3d})$$

$$Y_5 = Q_{10} (iX_{147} Z_{123}) (iX_{12} Z_{14}) (iX_{89} Z_{69}) S_x^{(1)} S_z^{(1)}, \quad (\text{B3e})$$

$$Y_6 = -Q_6 X_{147} X_{12} X_{23} Z_{69} S_x^{(1)} S_x^{(2)}, \quad (\text{B3f})$$

$$Y_7 = Q_{13} X_{89} (iX_{78} Z_{47}) Z_{14}, \quad (\text{B3g})$$

$$Y_8 = -Q_{14} Z_{123} Z_{14} Z_{47} X_{89} S_z^{(1)} S_z^{(2)}, \quad (\text{B3h})$$

$$Y_9 = Q_2, \quad (\text{B3i})$$

where $Q_7 = X_1 Z_9$, $Q_8 = Y_1$, $Q_9 = Y_1 X_9$, $Q_{10} = Y_{19}$, $Q_{11} = Y_1 Z_9$, $Q_{13} = Z_1 X_9$, and $Q_{14} = Z_1 Y_9$, cf. Table I.

The above identities express single-qubit errors in terms of the operators Q_ℓ , which define the orthonormal bases of the error subspaces (given in Table I), the operators X_{147} and Z_{123} , the gauge operators G_k and the stabilizer generators $S_q^{(n)}$, $q = x, z$ and $n = 1, 2$. The operators X_{147} and Z_{123} respectively perform logical X ($\alpha \leftrightarrow \beta$) and Z ($\alpha \rightarrow \alpha, \beta \rightarrow -\beta$) operations on the logical state (α, β) if $\ell = 0$ (i.e., when the wavefunction Eq. (17) belongs to the code space). For $\ell = 1, 2, \dots, 15$, the operators X_{147} and Z_{123} additionally introduce an overall sign factor, denoted by $\zeta_X^{(\ell)}$ and $\zeta_Z^{(\ell)}$ (respectively), if they anticommute with Q_ℓ .

For $\ell = 0$, we replace $G_k \rightarrow \mathcal{G}_k$ [since $\zeta_k^{(0)} = 1$ in Eq. (21)], $X_{147} \rightarrow X_L$, $Z_{123} \rightarrow Z_L$, and $S_q^{(n)} \rightarrow 1$ (by definition of code space, see Table I) in Eqs. (B1)–(B3). Then, X errors can be rewritten as

$$X_1 \xleftrightarrow{Q_0} Q_4, \quad (\text{B4a})$$

$$X_2 \xleftrightarrow{Q_0} Q_4 X_1^g, \quad (\text{B4b})$$

$$X_3 \xleftrightarrow{Q_0} Q_4 X_{12}^g, \quad (\text{B4c})$$

$$X_4 \xleftrightarrow{Q_0} Q_5 X_L X_{34}^g, \quad (\text{B4d})$$

$$X_5 \xleftrightarrow{Q_0} Q_5 X_L X_{14}^g, \quad (\text{B4e})$$

$$X_6 \xleftrightarrow{Q_0} Q_5 X_L X_{12}^g, \quad (\text{B4f})$$

$$X_7 \xleftrightarrow{Q_0} Q_1 X_{34}^g, \quad (\text{B4g})$$

$$X_8 \xleftrightarrow{Q_0} Q_1 X_4^g, \quad (\text{B4h})$$

$$X_9 \xleftrightarrow{Q_0} Q_1, \quad (\text{B4i})$$

where $\xleftrightarrow{Q_0}$ indicates that the equivalence relations (B4) applies to wavefunctions of the form of Eq. (17) with

$\ell = 0$. Similarly, for Z and Y errors we have

$$Z_1 \xleftrightarrow{Q_0} Q_{12}, \quad (\text{B5a})$$

$$Z_2 \xleftrightarrow{Q_0} Q_{15} Z_L Z_{24}^g, \quad (\text{B5b})$$

$$Z_3 \xleftrightarrow{Q_0} Q_3 Z_{24}^g, \quad (\text{B5c})$$

$$Z_4 \xleftrightarrow{Q_0} Q_{12} Z_1^g, \quad (\text{B5d})$$

$$Z_5 \xleftrightarrow{Q_0} Q_{15} Z_L Z_{14}^g, \quad (\text{B5e})$$

$$Z_6 \xleftrightarrow{Q_0} Q_3 Z_4^g, \quad (\text{B5f})$$

$$Z_7 \xleftrightarrow{Q_0} Q_{12} Z_{13}^g, \quad (\text{B5g})$$

$$Z_8 \xleftrightarrow{Q_0} Q_{15} Z_L Z_{13}^g, \quad (\text{B5h})$$

$$Z_9 \xleftrightarrow{Q_0} Q_3, \quad (\text{B5i})$$

and

$$Y_1 \xleftrightarrow{Q_0} Q_8, \quad (\text{B6a})$$

$$Y_2 \xleftrightarrow{Q_0} -Q_{11} Z_L Z_{24}^g X_1^g, \quad (\text{B6b})$$

$$Y_3 \xleftrightarrow{Q_0} Q_7 X_1^g Y_2^g Z_4^g, \quad (\text{B6c})$$

$$Y_4 \xleftrightarrow{Q_0} -Q_9 X_L X_{34}^g Z_1^g, \quad (\text{B6d})$$

$$Y_5 \xleftrightarrow{Q_0} Q_{10} Y_L Y_{14}^g, \quad (\text{B6e})$$

$$Y_6 \xleftrightarrow{Q_0} -Q_6 X_L X_{12}^g Z_4^g, \quad (\text{B6f})$$

$$Y_7 \xleftrightarrow{Q_0} Q_{13} X_4^g Y_3^g Z_1^g, \quad (\text{B6g})$$

$$Y_8 \xleftrightarrow{Q_0} -Q_{14} Z_L X_4^g Z_{13}^g, \quad (\text{B6h})$$

$$Y_9 \xleftrightarrow{Q_0} Q_2, \quad (\text{B6i})$$

where $Y_j^g = iX_j^g Z_j^g$.

To get the above equivalence relations for the error subspaces ($\ell = 1, 2, \dots, 15$), we replace $G_k \rightarrow \zeta_k^{(\ell)} \mathcal{G}_k$, $X_{147} \rightarrow \zeta_X^{(\ell)} X_L$, $Z_{123} \rightarrow \zeta_Z^{(\ell)} Z_L$, and $S_q^{(n)} \rightarrow \pm 1$ (according to Table I) in Eqs. (B1)–(B3). As mentioned above, $\zeta_k^{(\ell)} = -1 (+1)$ if G_k anticommutes (commutes) with operator Q_ℓ , and $\zeta_X^{(\ell)} = -1 (+1)$ and $\zeta_Z^{(\ell)} = -1 (+1)$ if X_{147} and Z_{123} anticommute (commute) with operator Q_ℓ , respectively.

There is one more thing that we need to know to fully determine the effect of single-qubit errors on the wavefunction $|\Psi_{Q_\ell}\rangle$. This is the multiplication Table IV between two operators Q_{ℓ_1} and Q_{ℓ_2} (Table II is a simplified version of this table that does not include phase factors.) Note that such a table is nonsymmetric since some Q_{ℓ_1} and Q_{ℓ_2} anticommute. To explain how to use this table, let us consider the following example. We wish to find the new logical state $(\tilde{\alpha}, \tilde{\beta})$ and new state of the gauge qubits (coefficients $\tilde{c}_{q_1 q_2 q_3 q_4}$), as well as the overall phase factor that the wavefunction $|\Psi_{Q_4}\rangle = Q_4 |\Psi_0\rangle$ acquires after applying error Z_2 (here, $|\Psi_0\rangle$ is an auxiliary code space wavefunction that only depends on α, β and coefficients $c_{q_1 q_2 q_3 q_4}$). The wavefunction after this error is $Z_2 |\Psi_{Q_4}\rangle = -Q_{15} Z_L Z_{24}^g \times Q_4 |\Psi_0\rangle$, where the sign factor comes from

TABLE IV. Multiplication table between error-subspace basis operators Q_ℓ . Note that this table is nonsymmetric.

\times	Q_0	Q_1	Q_2	Q_3	Q_4	Q_5	Q_6	Q_7	Q_8	Q_9	Q_{10}	Q_{11}	Q_{12}	Q_{13}	Q_{14}	Q_{15}
$Q_0 = \mathbb{1}$	$\mathbb{1}$	Q_1	Q_2	Q_3	Q_4	Q_5	Q_6	Q_7	Q_8	Q_9	Q_{10}	Q_{11}	Q_{12}	Q_{13}	Q_{14}	Q_{15}
Q_1	Q_1	$\mathbb{1}$	iQ_3	$-iQ_2$	Q_5	Q_4	iQ_7	$-iQ_6$	Q_9	Q_8	iQ_{11}	$-iQ_{10}$	Q_{13}	Q_{12}	iQ_{15}	$-iQ_{14}$
Q_2	Q_2	$-iQ_3$	$\mathbb{1}$	iQ_1	Q_6	$-iQ_7$	Q_4	iQ_5	Q_{10}	$-iQ_{11}$	Q_8	iQ_9	Q_{14}	$-iQ_{15}$	Q_{12}	iQ_{13}
Q_3	Q_3	iQ_2	$-iQ_1$	$\mathbb{1}$	Q_7	iQ_6	$-iQ_5$	Q_4	Q_{11}	iQ_{10}	$-iQ_9$	Q_8	Q_{15}	iQ_{14}	$-iQ_{13}$	Q_{12}
Q_4	Q_4	Q_5	Q_6	Q_7	$\mathbb{1}$	Q_1	Q_2	Q_3	iQ_{12}	iQ_{13}	iQ_{14}	iQ_{15}	$-iQ_8$	$-iQ_9$	$-iQ_{10}$	$-iQ_{11}$
Q_5	Q_5	Q_4	iQ_7	$-iQ_6$	Q_1	$\mathbb{1}$	iQ_3	$-iQ_2$	iQ_{13}	iQ_{12}	$-Q_{15}$	Q_{14}	$-iQ_9$	$-iQ_8$	Q_{11}	$-Q_{10}$
Q_6	Q_6	$-iQ_7$	Q_4	iQ_5	Q_2	$-iQ_3$	$\mathbb{1}$	iQ_1	iQ_{14}	Q_{15}	iQ_{12}	$-Q_{13}$	$-iQ_{10}$	$-Q_{11}$	$-iQ_8$	Q_9
Q_7	Q_7	iQ_6	$-iQ_5$	Q_4	Q_3	iQ_2	$-iQ_1$	$\mathbb{1}$	iQ_{15}	$-Q_{14}$	Q_{13}	iQ_{12}	$-iQ_{11}$	Q_{10}	$-Q_9$	$-iQ_8$
Q_8	Q_8	Q_9	Q_{10}	Q_{11}	$-iQ_{12}$	$-iQ_{13}$	$-iQ_{14}$	$-iQ_{15}$	$\mathbb{1}$	Q_1	Q_2	Q_3	iQ_4	iQ_5	iQ_6	iQ_7
Q_9	Q_9	Q_8	iQ_{11}	$-iQ_{10}$	$-iQ_{13}$	$-iQ_{12}$	Q_{15}	$-Q_{14}$	Q_1	$\mathbb{1}$	iQ_3	$-iQ_2$	iQ_5	iQ_4	$-Q_7$	Q_6
Q_{10}	Q_{10}	$-iQ_{11}$	Q_8	iQ_9	$-iQ_{14}$	$-Q_{15}$	$-iQ_{12}$	Q_{13}	Q_2	$-iQ_3$	$\mathbb{1}$	iQ_1	iQ_6	Q_7	iQ_4	$-Q_5$
Q_{11}	Q_{11}	iQ_{10}	$-iQ_9$	Q_8	$-iQ_{15}$	Q_{14}	$-Q_{13}$	$-iQ_{12}$	Q_3	iQ_2	$-iQ_1$	$\mathbb{1}$	iQ_7	$-Q_6$	Q_5	iQ_4
Q_{12}	Q_{12}	Q_{13}	Q_{14}	Q_{15}	iQ_8	iQ_9	iQ_{10}	iQ_{11}	$-iQ_4$	$-iQ_5$	$-iQ_6$	$-iQ_7$	$\mathbb{1}$	Q_1	Q_2	Q_3
Q_{13}	Q_{13}	Q_{12}	iQ_{15}	$-iQ_{14}$	iQ_9	iQ_8	$-Q_{11}$	Q_{10}	$-iQ_5$	$-iQ_4$	Q_7	$-Q_6$	Q_1	$\mathbb{1}$	iQ_3	$-iQ_2$
Q_{14}	Q_{14}	$-iQ_{15}$	Q_{12}	iQ_{13}	iQ_{10}	Q_{11}	iQ_8	$-Q_9$	$-iQ_6$	$-Q_7$	$-iQ_4$	Q_5	Q_2	$-iQ_3$	$\mathbb{1}$	iQ_1
Q_{15}	Q_{15}	iQ_{14}	$-iQ_{13}$	Q_{12}	iQ_{11}	$-Q_{10}$	Q_9	iQ_8	$-iQ_7$	Q_6	$-Q_5$	$-iQ_4$	Q_3	iQ_2	$-iQ_1$	$\mathbb{1}$

replacing Z_{123} by $-Z_L$ in Eq. (B2b), since Z_{123} anticommutes with $Q_4 = X_1$. Next, we use Table IV to obtain $Q_{15} \times Q_4 = iQ_{11}$, so $Z_2|\Psi_{Q_4}\rangle = -iZ_L Z_{24}^g Q_{11}|\Psi\rangle$. Thus, the wavefunction after the error is in the error subspace \mathcal{Q}_{11} with $\tilde{\alpha} = \alpha, \tilde{\beta} = -\beta, \tilde{c}_{0000} = c_{0000}, \tilde{c}_{0001} = -c_{0001}, \tilde{c}_{0010} = c_{0010}, \tilde{c}_{0011} = -c_{0011}, \tilde{c}_{0100} = -c_{0100}, \tilde{c}_{0101} = c_{0101}, \tilde{c}_{0110} = -c_{0110}, \tilde{c}_{0111} = c_{0111}, \tilde{c}_{1000} = c_{1000}, \tilde{c}_{1001} = -c_{1001}, \tilde{c}_{1010} = c_{1010}, \tilde{c}_{1011} = -c_{1011}, \tilde{c}_{1100} = -c_{1100}, \tilde{c}_{1101} = c_{1101}, \tilde{c}_{1110} = -c_{1110}, \tilde{c}_{1111} = c_{1111}$, and the overall phase factor is $-i$. Note that Z_L and Z_{14}^g act directly on the probability amplitudes, so they commute with any operator Q_ℓ , which acts on the basis vectors.

Note that if we ignore overall phase factors in the equivalence relations (B4)–(B6), we obtain the equivalence relations of Table II.

2. Harmful two-qubit errors in conventional operation of nine-qubit Bacon-Shor code

In this section we want to determine the harmful two error combinations (E_1 and E_2) that induce a logical error after an operation cycle. By definition, these two errors occur in the same operation cycle and, after application of the error correcting operation C_{op} at the end of the cycle, the logical state suffers from a logical operation (X_L, Y_L or Z_L). That is, the two errors satisfy

$$E_1 E_2 C_{\text{op}} \sim X_L, Y_L \text{ or } Z_L, \quad (\text{B7})$$

where “ \sim ” means equivalence modulo gauge operations, and we disregard overall phase factors in this section. We assume that the system state is initially in the code space; however, this assumption is not crucial. It is convenient in what follows to simplify the equivalence rela-

tions (B4)–(B6) by disregarding the gauge operations:

$$\begin{aligned}
X_7, X_8, X_9 &\sim Q_1, \\
Y_9 &\sim Q_2, \\
Z_3, Z_6, Z_9 &\sim Q_3, \\
X_1, X_2, X_3 &\sim Q_4, \\
X_4, X_5, X_6 &\sim Q_5 X_L, \\
Y_6 &\sim Q_6 X_L, \\
Y_3 &\sim Q_7, \\
Y_1 &\sim Q_8, \\
Y_4 &\sim Q_9 X_L, \\
Y_5 &\sim Q_{10} Y_L, \\
Y_2 &\sim Q_{11} Z_L, \\
Z_1, Z_4, Z_7 &\sim Q_{12}, \\
Y_7 &\sim Q_{13}, \\
Y_8 &\sim Q_{14} Z_L, \\
Z_2, Z_5, Z_8 &\sim Q_{15} Z_L.
\end{aligned} \quad (\text{B8})$$

Note that the left-hand sides of Eq. (B8) are the error correcting operations C_{op} given in Table I; this is due to the fact that Q_ℓ^2 is trivial (identity).

Let us assume that $E_1 \sim Q_{\ell_1} O_1$ and $E_2 \sim Q_{\ell_2} O_2$ so $E_1 E_2 \sim Q_\ell (O_1 O_2)$, where $Q_\ell = Q_{\ell_1} Q_{\ell_2}$, and O_1 and O_2 can be trivial (identity) or a logical operation (X_L, Y_L or Z_L). The fact that $E_1 E_2$ is “proportional” to Q_ℓ implies that such two-qubit error induces a jump from the code space to the error subspace \mathcal{Q}_ℓ . Since the error correcting operation must bring the system state back to the code space, it must also be “proportional” to Q_ℓ . To proceed, we fix Q_ℓ (in this way, C_{op} is also fixed up to gauge operations) and then use Table II to find all possible pairs Q_{ℓ_1} and Q_{ℓ_2} whose product is Q_ℓ ; we obtain:

$$\begin{aligned}
Q_1 &= \{Q_{23}, Q_{45} [X_L], Q_{67} [X_L], Q_{89} [X_L], Q_{1011} [X_L], Q_{1213}, Q_{1415}\}, \\
Q_2 &= \{Q_{13}, Q_{46} [X_L], Q_{57} [X_L], Q_{810} [Y_L], Q_{911} [Y_L], Q_{1214} [Z_L], Q_{1315} [Z_L]\}, \\
Q_3 &= \{Q_{12}, Q_{47}, Q_{56}, Q_{811} [Z_L], Q_{910} [Z_L], Q_{1215} [Z_L], Q_{1314} [Z_L]\}, \\
Q_4 &= \{Q_{15} [X_L], Q_{26} [X_L], Q_{37}, Q_{812}, Q_{913} [X_L], Q_{1014} [X_L], Q_{1115}\}, \\
Q_5 &= \{Q_{14} [X_L], Q_{27} [X_L], Q_{36}, Q_{813} [X_L], Q_{912}, Q_{1015}, Q_{1114} [X_L]\}, \\
Q_6 &= \{Q_{17} [X_L], Q_{24} [X_L], Q_{35}, Q_{814} [Y_L], Q_{915} [Z_L], Q_{1012} [Z_L], Q_{1113} [Y_L]\}, \\
Q_7 &= \{Q_{16} [X_L], Q_{25} [X_L], Q_{34}, Q_{815} [Z_L], Q_{914} [Y_L], Q_{1013} [Y_L], Q_{1112} [Z_L]\}, \\
Q_8 &= \{Q_{19} [X_L], Q_{210} [Y_L], Q_{311} [Z_L], Q_{412}, Q_{513} [X_L], Q_{614} [Y_L], Q_{715} [Z_L]\}, \\
Q_9 &= \{Q_{18}, Q_{211} [Y_L], Q_{310} [Z_L], Q_{413} [X_L], Q_{512}, Q_{615} [Z_L], Q_{714} [Y_L]\}, \\
Q_{10} &= \{Q_{111} [X_L], Q_{28} [Y_L], Q_{39} [Z_L], Q_{414} [X_L], Q_{515}, Q_{612} [Z_L], Q_{713} [Y_L]\}, \\
Q_{11} &= \{Q_{110} [X_L], Q_{29} [Y_L], Q_{38} [Z_L], Q_{415}, Q_{514} [X_L], Q_{613} [Y_L], Q_{712} [Z_L]\}, \\
Q_{12} &= \{Q_{113}, Q_{214} [Z_L], Q_{315} [Z_L], Q_{48}, Q_{59}, Q_{610} [Z_L], Q_{711} [Z_L]\}, \\
Q_{13} &= \{Q_{112}, Q_{215} [Z_L], Q_{314} [Z_L], Q_{49} [X_L], Q_{58} [X_L], Q_{611} [Y_L], Q_{710} [Y_L]\}, \\
Q_{14} &= \{Q_{115}, Q_{212} [Z_L], Q_{313} [Z_L], Q_{410} [X_L], Q_{511} [X_L], Q_{68} [Y_L], Q_{79} [Y_L]\}, \\
Q_{15} &= \{Q_{114}, Q_{213} [Z_L], Q_{312} [Z_L], Q_{411}, Q_{510}, Q_{69} [Z_L], Q_{78} [Z_L]\}, \tag{B9}
\end{aligned}$$

where $Q_{\ell_1 \ell_2} = Q_{\ell_1} Q_{\ell_2}$. Next, we use Eq. (B8) to find the (single-qubit) errors E_1 and E_2 that are “proportional” to Q_{ℓ_1} and Q_{ℓ_2} , respectively. Finally, for each Q_ℓ -line of Eq. (B9), we obtain the corresponding C_{op} from Table I and check the condition (B7) to determine whether $E_1 E_2$ induces a logical X , Y or Z error; the type of logical error is indicated inside the square brackets of Eq. (B9). The lists of harmful two-qubit errors that lead to logical errors are given in Eqs. (9)–(11).

3. Harmful two-qubit errors in continuous operation of nine-qubit Bacon-Shor code

It turns out that harmful two-qubit errors in the discrete operation are also harmful two-qubit errors in the continuous operation, assuming large time averaging parameter T_c (noiseless cross-correlators limit). To realize this let us consider realizations with only two errors; namely, first $E_1 \sim Q_{\ell_1} O_1$ and second $E_2 \sim Q_{\ell_2} O_2$ that occur at moments $t_{\text{err}}^{(1)}$ and $t_{\text{err}}^{(2)}$, respectively. Here, O_1 and O_2 can be trivial (identity) or logical operations (X_L , Y_L , or Z_L); let us also assume that $Q_{\ell_1} Q_{\ell_2} = Q_\ell$.

The actual error syndrome path $\mathcal{S}(t)$ exhibits two jumps: the first one from $\mathcal{S} = 0$ to $\mathcal{S} = \ell_1$ at the moment $t_{\text{err}}^{(1)}$, and the second one from $\mathcal{S} = \ell_1$ to $\mathcal{S} = \ell$ at

the moment $t_{\text{err}}^{(2)}$. In contrast, the monitored error syndrome path $\mathcal{S}_m(t)$ exhibits only one jump from $\mathcal{S}_m = 0$ to $\mathcal{S}_m = \ell$ if the errors occur close in time such that $t_{\text{err}}^{(2)} - t_{\text{err}}^{(1)} < \Delta t_{\text{cont}}$, where Δt_{cont} is given in Eq. (69). In this situation, the continuous QEC protocol assigns the single-qubit error $E_{\text{false}} = Q_\ell O_{\text{false}}$, where O_{false} can be trivial or a logical operation. The total logical operations from $\mathcal{S}(t)$ and $\mathcal{S}_m(t)$ are $\mathcal{O} = O_1 O_2$ and $\mathcal{O}_m = O_{\text{false}}$, respectively, and a logical error occurs if $\mathcal{O}_m \mathcal{O}$ is a logical operation— see discussion above Eq. (37). This condition for logical error in our continuous QEC protocol is equivalent to say that $E_1 E_2 E_{\text{false}} \sim X_L, Y_L$ or Z_L , which is the condition for harmful two-qubit errors in the conventional operation, cf. Eq. (B7), with E_{false} playing the role of C_{op} .

Appendix C: Logical error rates for discrete operation

In this section we present the formulas for the logical error rates of the nine-qubit Bacon-Shor code where the nine physical qubits are subject to X , Y and Z errors with occurrence rates $\Gamma_i^{(X)}$, $\Gamma_i^{(Y)}$ and $\Gamma_i^{(Z)}$. The logical X error rate is equal to

$$\begin{aligned}
\gamma_X^{\text{cont}} = \Delta t & \left[(\Gamma_1^{(X)} + \Gamma_2^{(X)} + \Gamma_3^{(X)}) (\Gamma_4^{(X)} + \Gamma_5^{(X)} + \Gamma_6^{(X)}) + \Gamma_3^{(Y)} \Gamma_6^{(Y)} + \Gamma_1^{(Y)} \Gamma_4^{(Y)} + \Gamma_2^{(Y)} \Gamma_5^{(Y)} + \right. \\
& (\Gamma_1^{(X)} + \Gamma_2^{(X)} + \Gamma_3^{(X)}) \Gamma_6^{(Y)} + (\Gamma_4^{(X)} + \Gamma_5^{(X)} + \Gamma_6^{(X)}) \Gamma_3^{(Y)} + \\
& (\Gamma_7^{(X)} + \Gamma_8^{(X)} + \Gamma_9^{(X)}) (\Gamma_4^{(X)} + \Gamma_5^{(X)} + \Gamma_6^{(X)}) + \Gamma_6^{(Y)} \Gamma_9^{(Y)} + \Gamma_4^{(Y)} \Gamma_7^{(Y)} + \Gamma_5^{(Y)} \Gamma_8^{(Y)} + \\
& (\Gamma_1^{(X)} + \Gamma_2^{(X)} + \Gamma_3^{(X)}) (\Gamma_7^{(X)} + \Gamma_8^{(X)} + \Gamma_9^{(X)}) + \Gamma_3^{(Y)} \Gamma_9^{(Y)} + \Gamma_1^{(Y)} \Gamma_7^{(Y)} + \Gamma_2^{(Y)} \Gamma_8^{(Y)} + \\
& \Gamma_3^{(Y)} (\Gamma_7^{(X)} + \Gamma_8^{(X)} + \Gamma_9^{(X)}) + \Gamma_9^{(Y)} (\Gamma_1^{(X)} + \Gamma_2^{(X)} + \Gamma_3^{(X)}) + \\
& \Gamma_6^{(Y)} (\Gamma_7^{(X)} + \Gamma_8^{(X)} + \Gamma_9^{(X)}) + \Gamma_9^{(Y)} (\Gamma_4^{(X)} + \Gamma_5^{(X)} + \Gamma_6^{(X)}) + \\
& \Gamma_4^{(Y)} (\Gamma_7^{(X)} + \Gamma_8^{(X)} + \Gamma_9^{(X)}) + \Gamma_7^{(Y)} (\Gamma_4^{(X)} + \Gamma_5^{(X)} + \Gamma_6^{(X)}) + \\
& \Gamma_1^{(Y)} (\Gamma_7^{(X)} + \Gamma_8^{(X)} + \Gamma_9^{(X)}) + \Gamma_7^{(Y)} (\Gamma_1^{(X)} + \Gamma_2^{(X)} + \Gamma_3^{(X)}) + \\
& \Gamma_2^{(Y)} (\Gamma_7^{(X)} + \Gamma_8^{(X)} + \Gamma_9^{(X)}) + \Gamma_8^{(Y)} (\Gamma_1^{(X)} + \Gamma_2^{(X)} + \Gamma_3^{(X)}) + \\
& \Gamma_5^{(Y)} (\Gamma_7^{(X)} + \Gamma_8^{(X)} + \Gamma_9^{(X)}) + \Gamma_8^{(Y)} (\Gamma_4^{(X)} + \Gamma_5^{(X)} + \Gamma_6^{(X)}) + \\
& \Gamma_4^{(Y)} (\Gamma_1^{(X)} + \Gamma_2^{(X)} + \Gamma_3^{(X)}) + \Gamma_1^{(Y)} (\Gamma_4^{(X)} + \Gamma_5^{(X)} + \Gamma_6^{(X)}) + \\
& \left. \Gamma_5^{(Y)} (\Gamma_1^{(X)} + \Gamma_2^{(X)} + \Gamma_3^{(X)}) + \Gamma_2^{(Y)} (\Gamma_4^{(X)} + \Gamma_5^{(X)} + \Gamma_6^{(X)}) \right], \tag{C1}
\end{aligned}$$

where the terms in the lines of formula (C1) correspond to the two-qubit errors in the lines of list (9). The formula for the logical Z error rate is obtained from Eq. (C1) with upper labels X and Z in $\Gamma_i^{(E)}$ exchanged and the qubit numbering subscripts $2 \leftrightarrow 4$, $3 \leftrightarrow 7$ and $6 \leftrightarrow 8$ also exchanged. The formula for the logical Y error rate reads as

$$\begin{aligned}
\gamma_Y^{\text{cont}} = \Delta t & \left[\Gamma_1^{(Y)} \Gamma_5^{(Y)} + \Gamma_2^{(Y)} \Gamma_4^{(Y)} + \right. \\
& \Gamma_1^{(Y)} \Gamma_8^{(Y)} + \Gamma_2^{(Y)} \Gamma_7^{(Y)} + \\
& \Gamma_4^{(Y)} \Gamma_8^{(Y)} + \Gamma_5^{(Y)} \Gamma_7^{(Y)} + \\
& \Gamma_9^{(Y)} \Gamma_5^{(Y)} + \Gamma_6^{(Y)} \Gamma_8^{(Y)} + \\
& \Gamma_2^{(Y)} \Gamma_9^{(Y)} + \Gamma_3^{(Y)} \Gamma_8^{(Y)} + \\
& \Gamma_1^{(Y)} \Gamma_9^{(Y)} + \Gamma_3^{(Y)} \Gamma_7^{(Y)} + \\
& \Gamma_4^{(Y)} \Gamma_9^{(Y)} + \Gamma_6^{(Y)} \Gamma_7^{(Y)} + \\
& \Gamma_2^{(Y)} \Gamma_6^{(Y)} + \Gamma_3^{(Y)} \Gamma_5^{(Y)} + \\
& \left. \Gamma_1^{(Y)} \Gamma_6^{(Y)} + \Gamma_3^{(Y)} \Gamma_4^{(Y)} \right]. \tag{C2}
\end{aligned}$$

Appendix D: Calculation of two-time correlator Eq. (63)

We discuss the calculation of the following correlator

$$\begin{aligned}
\langle \tilde{C}_x^{(1)}(t) \tilde{C}_x^{(1)}(0) \rangle &= \int_{-\infty}^t dt_1 \int_{-\infty}^t dt_2 \int_{-\infty}^t dt_3 \int_{-\infty}^0 dt'_1 \\
& \int_{-\infty}^0 dt'_2 \int_{-\infty}^0 dt'_3 K_6(t_1, t'_1, t_2, t'_2, t_3, t'_3) \\
& \times \frac{e^{-\frac{t-t_1}{\tau_c} - \frac{t-t_2}{\tau_c} - \frac{t-t_3}{\tau_c} + \frac{t'_1}{\tau_c} + \frac{t'_2}{\tau_c} + \frac{t'_3}{\tau_c}}}{\tau_c^6}, \tag{D1}
\end{aligned}$$

where

$$\begin{aligned}
K_6(t_1, t'_1, t_2, t'_2, t_3, t'_3) &= \\
\langle I_{X_3^g}(t_3) I_{X_3^g}(t'_3) I_{X_{13}^g}(t_2) I_{X_{13}^g}(t'_2) I_{X_1^g}(t_1) I_{X_1^g}(t'_1) \rangle & \tag{D2}
\end{aligned}$$

is a six-time correlator for the measurement signals $I_{X_1^g}(t)$, $I_{X_{13}^g}(t)$ and $I_{X_3^g}(t)$, which are defined in Eq. (26). We remind that the noises for such measurement signals are, respectively, denoted by $\xi_7(t)$, $\xi_8(t)$ and $\xi_9(t)$ —see Section III A.

To evaluate K_6 , we use formula (49). This formula, however, does not include singular contributions that arise when the times of two measurement signals (from the same detector) in K_6 coincide [61]. Specifically, such singular contributions occur when the pair of times in each group (t_1, t'_1) , (t_2, t'_2) or (t_3, t'_3) coincide. For example, if only t_3 and t'_3 coincide, $K_6 = (\tau_m/\delta t) \langle I_{X_{13}^g}(t_2) I_{X_{13}^g}(t'_2) I_{X_1^g}(t_1) I_{X_1^g}(t'_1) \rangle_{\text{nc.t.}}$ since we may approximately replace the product $I_{X_3^g}(t_3) I_{X_3^g}(t'_3)$ in Eq. (D2) by $\tau_m [\xi_9(t_3)]^2$, which is equal to $\tau_m/\delta t$ after averaging over the noise $\xi_9(t)$. Here, δt is an infinitesimal discretization timestep and the subscript “nc.t.” means “not coinciding times”; that is, the times of the output signals (from the same detector) inside the angular bracket $(\langle \cdot \rangle_{\text{nc.t.}})$ do not coincide. The remaining (non-singular) four-time correlator $\langle I_{X_{13}^g}(t_2) I_{X_{13}^g}(t'_2) I_{X_1^g}(t_1) I_{X_1^g}(t'_1) \rangle_{\text{nc.t.}}$ is evaluated using formula (49). Similarly, $K_6 = (\tau_m/\delta t)^2 \langle I_{X_1^g}(t_1) I_{X_1^g}(t'_1) \rangle_{\text{nc.t.}}$ if (t_2, t'_2) and (t_3, t'_3) are the only pairs of coinciding times, and $K_6 = (\tau_m/\delta t)^3$ if (t_1, t'_1) , (t_2, t'_2) and (t_3, t'_3) are all pairs of coinciding times. Note that each singular factor $(\tau_m/\delta t)$ replaces one of the integrals in Eq. (D1) by a factor τ_m ; for example, if only t_3 and t'_3 coincide, the integral over t'_3 is replaced by the factor τ_m , while the integral over t_3 becomes trivial and gives an additional factor equal to

$\int_{-\infty}^0 dt_3 \exp(2t_3/\tau_c) = \tau_c/2$. In other words, one may say that each singular factor ($\tau_m/\delta t$) due to pairs of co-

inciding times (t_n, t'_n) in Eq. (D2) effectively replaces the integrals over t_n and t'_n by the factor $\tau_m\tau_c/2$. Taking into account the considerations just described, the sought correlator (D1) can be written as

$$\begin{aligned}
\langle \tilde{\mathcal{C}}_x^{(1)}(t) \tilde{\mathcal{C}}_x^{(1)}(0) \rangle &= \int_{-\infty}^t dt_1 \int_{-\infty}^t dt_2 \int_{-\infty}^t dt_3 \int_{-\infty}^0 dt'_1 \int_{-\infty}^0 dt'_2 \int_{-\infty}^0 dt'_3 \langle I_{X_3^g}(t_3) I_{X_3^g}(t'_3) I_{X_{13}^g}(t_2) I_{X_{13}^g}(t'_2) I_{X_1^g}(t_1) \\
&\quad \times I_{X_1^g}(t'_1) \rangle_{\text{nc.t.}} \frac{e^{-\frac{t-t_1}{\tau_c} - \frac{t-t_2}{\tau_c} - \frac{t-t_3}{\tau_c} + \frac{t'_1}{\tau_c} + \frac{t'_2}{\tau_c} + \frac{t'_3}{\tau_c}}}{\tau_c^6} \\
&+ \frac{\tau_m\tau_c}{2} \int_{-\infty}^t dt_1 \int_{-\infty}^t dt_2 \int_{-\infty}^0 dt'_1 \int_{-\infty}^0 dt'_2 \langle I_{X_{13}^g}(t_2) I_{X_{13}^g}(t'_2) I_{X_1^g}(t_1) I_{X_1^g}(t'_1) \rangle_{\text{nc.t.}} \frac{e^{-\frac{t}{\tau_c} - \frac{t-t_1}{\tau_c} - \frac{t-t_2}{\tau_c} + \frac{t'_1}{\tau_c} + \frac{t'_2}{\tau_c}}}{\tau_c^6} \\
&+ \frac{\tau_m\tau_c}{2} \int_{-\infty}^t dt_3 \int_{-\infty}^t dt_2 \int_{-\infty}^0 dt'_3 \int_{-\infty}^0 dt'_2 \langle I_{X_{13}^g}(t_2) I_{X_{13}^g}(t'_2) I_{X_3^g}(t_3) I_{X_3^g}(t'_3) \rangle_{\text{nc.t.}} \frac{e^{-\frac{t}{\tau_c} - \frac{t-t_3}{\tau_c} - \frac{t-t_2}{\tau_c} + \frac{t'_3}{\tau_c} + \frac{t'_2}{\tau_c}}}{\tau_c^6} \\
&+ \frac{\tau_m\tau_c}{2} \int_{-\infty}^t dt_1 \int_{-\infty}^t dt_3 \int_{-\infty}^0 dt'_1 \int_{-\infty}^0 dt'_3 \langle I_{X_3^g}(t_3) I_{X_3^g}(t'_3) I_{X_1^g}(t_1) I_{X_1^g}(t'_1) \rangle_{\text{nc.t.}} \frac{e^{-\frac{t}{\tau_c} - \frac{t-t_1}{\tau_c} - \frac{t-t_3}{\tau_c} + \frac{t'_1}{\tau_c} + \frac{t'_3}{\tau_c}}}{\tau_c^6} \\
&+ \left(\frac{\tau_m\tau_c}{2}\right)^2 \int_{-\infty}^t dt_1 \int_{-\infty}^0 dt'_1 \langle I_{X_1^g}(t_1) I_{X_1^g}(t'_1) \rangle_{\text{nc.t.}} \frac{e^{-\frac{2t}{\tau_c} - \frac{t-t_1}{\tau_c} + \frac{t'_1}{\tau_c}}}{\tau_c^6} \\
&+ \left(\frac{\tau_m\tau_c}{2}\right)^2 \int_{-\infty}^t dt_3 \int_{-\infty}^0 dt'_3 \langle I_{X_3^g}(t_3) I_{X_3^g}(t'_3) \rangle_{\text{nc.t.}} \frac{e^{-\frac{2t}{\tau_c} - \frac{t-t_3}{\tau_c} + \frac{t'_3}{\tau_c}}}{\tau_c^6} \\
&+ \left(\frac{\tau_m\tau_c}{2}\right)^2 \int_{-\infty}^t dt_2 \int_{-\infty}^0 dt'_2 \langle I_{X_{13}^g}(t_2) I_{X_{13}^g}(t'_2) \rangle_{\text{nc.t.}} \frac{e^{-\frac{2t}{\tau_c} - \frac{t-t_2}{\tau_c} + \frac{t'_2}{\tau_c}}}{\tau_c^6} \\
&+ \left(\frac{\tau_m\tau_c}{2}\right)^3 \frac{e^{-\frac{3t}{\tau_c}}}{\tau_c^6}. \tag{D3}
\end{aligned}$$

The averages inside the integrands of Eq. (D3) are evaluated again using the result (49). The calculation of the first four lines in Eq. (D3) is particularly cumbersome since we have to divide the integration domains according to all possible time orderings of the integration variables since application of Eq. (49) requires time

ordering, as discussed in Section III C 1 for the calculation of the three-time correlator K_3 . Note that lines 2 and 3 in Eq. (D3) yield the same contribution in the case of symmetric measurement strengths for all detectors. We eventually find the result (65) with R_i given by (see Mathematica file at Supplemental Information [72])

$$\begin{aligned}
R_1 &= \frac{6s(s+1)^2(2s+1)}{D(s,\eta)} [(12(4\eta^2 + 8\eta + 5)s^{12} + 8(208\eta^2 + 234\eta + 135)s^{11} + 3(4748\eta^2 + 4756\eta + 2507)s^{10} \\
&\quad + (47680\eta^2 + 51468\eta + 23598)s^9 + (48220\eta^2 + 72963\eta + 18132)s^8 - 6(12824\eta^2 + 9657\eta + 14832)s^7 \\
&\quad - (198464\eta^2 + 302379\eta + 250755)s^6 - 18(5520\eta^2 + 14779\eta + 9321)s^5 + (36352\eta^2 + 61260\eta + 202458)s^4 \\
&\quad + 12(2080\eta^2 + 10858\eta + 27801)s^3 - 24(720\eta - 2741)s^2 - 720(40\eta + 141)s - 43200], \tag{D4a}
\end{aligned}$$

$$\begin{aligned}
R_2 &= -\frac{12s\eta(s-1)^2(s+2)^2}{D(s,\eta)} [8s^5 + 84s^4 + 278s^3 + 279s^2 - 70s - 75] [2(34\eta + 9)s^5 + (254\eta + 147)s^4 \\
&\quad + 18(16\eta + 23)s^3 + (96\eta + 531)s^2 + 318s + 72], \tag{D4b}
\end{aligned}$$

$$R_3 = \frac{6(s+1)^2}{D(s,\eta)} [8s^4 + 4s^3 - 42s^2 - s + 10] [4(28\eta^2 - 3)s^9 + 4(172\eta^2 - 27\eta - 54)s^8 - 3(96\eta^2 + 526\eta + 523)s^7 - 16(605\eta^2 + 552\eta + 366)s^6 - 6(3800\eta^2 + 4017\eta + 1925)s^5 - 12(1656\eta^2 + 2819\eta + 812)s^4 - 3(1920\eta^2 + 7664\eta - 1173)s^3 - 24(240\eta - 569)s^2 + 9612s + 2160], \quad (\text{D4c})$$

$$R_4 = \frac{6\eta s(s+1)^2}{D(s,\eta)} [8s^6 + 84s^5 + 226s^4 - 181s^3 - 1197s^2 - 590s + 600] [4(7\eta + 3)s^5 + 4(47\eta + 24)s^4 + 3(88\eta + 93)s^3 + (96\eta + 357)s^2 + 192s + 36], \quad (\text{D4d})$$

$$R_5 = -\frac{3(s-1)^2}{D(s,\eta)} [2s^5 + 17s^4 + 30s^3 - 53s^2 - 152s - 60] [12(2\eta + 1)^2s^8 + 8(76\eta^2 + 72\eta + 21)s^7 + (1876\eta^2 + 2676\eta + 981)s^6 + (2024\eta^2 + 6120\eta + 3138)s^5 + (672\eta^2 + 7236\eta + 6042)s^4 + 96(44\eta + 75)s^3 + 15(64\eta + 347)s^2 + 2094s + 360], \quad (\text{D4e})$$

where $s = 2\tau_c\tau_{\text{coll}}^{-1}$, $\tau_{\text{coll}} = \Gamma_m^{-1} = 2\tau_m\eta$, and the de-

nominator in Eqs. (D4) reads as

$$D(s,\eta) = 36s^2\eta^2(s-1)^2(s+1)^4(s-2)(s+2)^2(s+3)(s+4)(s+5)(2s-1)(2s+1)^2(2s+3)(2s+5). \quad (\text{D5})$$

-
- [1] P. W. Shor, Phys. Rev. A **52**, R2493 (1995).
[2] A. M. Steane, Phys. Rev. Lett. **77**, 793 (1996).
[3] D. Gottesman, Phys. Rev. A **54**, 1862 (1996); arXiv:quantph/9705052.
[4] D. Gottesman, Proc. Symp. Appl. Math. **68**, 13 (2010).
[5] M. A. Nielsen and I. L. Chuang, *Quantum Computation and Quantum Information* (Cambridge University Press, Cambridge, 2000).
[6] *Quantum Error Correction*, edited by Daniel A. Lidar and Todd A. Brun (Cambridge University Press, Cambridge, UK, 2013).
[7] D. G. Cory, M. D. Price, W. Maas, E. Knill, R. Laflamme, W. H. Zurek, T. F. Havel, and S. S. Somaro, Phys. Rev. Lett. **81**, 2152 (1998).
[8] J. Chiaverini, D. Leibfried, T. Schaetz, M. D. Barrett, R. B. Blakestad, J. Britton, W. M. Itano, J. D. Jost, E. Knill, C. Langer, R. Ozeri, and D. J. Wineland, Nature **432**, 602 (2004).
[9] P. Schindler, J. T. Barreiro, T. Monz, V. Nebendahl, D. Nigg, M. Chwalla, M. Hennrich, and R. Blatt, Science **332**, 1059 (2011).
[10] M. D. Reed, L. DiCarlo, S. E. Nigg, L. Sun, L. Frunzio, S. M. Girvin, and R. J. Schoelkopf, Nature **482**, 382 (2012).
[11] G. Waldherr, Y. Wang, S. Zaiser, M. Jamali, T. Schulte-Herbruggen, H. Abe, T. Ohshima, J. Isoya, J. F. Du, P. Neumann, and J. Wrachtrup, Nature **506**, 204 (2014).
[12] T. H. Taminiau, J. Cramer, T. van der Sar, V. V. Dobrovitski, and R. Hanson, Nat. Nanotechnol. **9**, 171 (2014).
[13] D. Nigg, M. Müller, E. A. Martinez, P. Schindler, M. Hennrich, T. Monz, M. A. Martin-Delgado, and R. Blatt, Science **345**, 302 (2014).
[14] J. Kelly, R. Barends, A. G. Fowler, A. Megrant, E. Jeffrey, T. C. White, D. Sank, J. Y. Mutus, B. Campbell, Yu Chen, Z. Chen, B. Chiaro, A. Dunsworth, I.-C. Hoi, C. Neill, P. J. J. O'Malley, C. Quintana, P. Roushan, A. Vainsencher, J. Wenner, A. N. Cleland, and John M. Martinis, Nature **519**, 66 (2015).
[15] D. Risté, S. Poletto, M.-Z. Huang, A. Bruno, V. Vesterinen, O.-P. Saira, and L. DiCarlo, Nat. Commun. **6**, 6983 (2015).
[16] J. M. Chow, J. M. Gambetta, E. Magesan, D. W. Abraham, A. W. Cross, B. R. Johnson, N. A. Masluk, C. A. Ryan, J. A. Smolin, S. J. Srinivasan, and M. Steffen, Nat. Commun. **5**, 4015 (2014).
[17] A. G. Fowler, M. Mariantoni, J. M. Martinis, and A. N. Cleland, Phys. Rev. A **86**, 032324 (2012).
[18] R. Raussendorf and J. Harrington, Phys. Rev. Lett. **98**, 190504 (2007).
[19] B. M. Terhal, Rev. Mod. Phys., **87**, 307 (2015).
[20] S. B. Bravyi and A. Yu. Kitaev, arXiv:quant-ph/9811052.
[21] D. Bacon, Phys. Rev. A **73**, 012340 (2006).
[22] P. Aliferis and A. W. Cross, Phys. Rev. Lett. **98**, 220502 (2007).
[23] D. Poulin, Phys. Rev. Lett. **95**, 230504 (2005).
[24] N. M. Linke, M. Gutierrez, K. A. Landsman, C. Figgatt, S. Debnath, K. R. Brown, and C. Monroe, Sci. Adv. **3**, e1701074 (2017).

- [25] J. P. Paz and W. H. Zurek, Proc. R. Soc. Lond. A **454**, 355 (1998).
- [26] C. Ahn, A. C. Doherty, and A. J. Landahl, Phys. Rev. A **65**, 042301 (2002).
- [27] C. Ahn, H. M. Wiseman, and G. J. Milburn, Phys. Rev. A **67**, 052310 (2003).
- [28] C. Ahn, H. M. Wiseman, and K. Jacobs, Phys. Rev. A **70**, 024302 (2004).
- [29] M. Sarovar, C. Ahn, K. Jacobs, and G. J. Milburn, Phys. Rev. A **69**, 052324 (2004).
- [30] M. Sarovar and G. J. Milburn, Phys. Rev. A **72**, 012306 (2005).
- [31] O. Oreshkov and T. A. Brun, Phys. Rev. A **76**, 022318 (2007).
- [32] B. A. Chase, A. J. Landahl, and J. M. Geremia, Phys. Rev. A **77**, 032304 (2008).
- [33] R. van Handel and H. Mabuchi, arXiv:quant-ph/0511221; H. Mabuchi, New J. Phys. **11**, 105044 (2009).
- [34] K. C. Hsu and T. A. Brun, Phys. Rev. A **93**, 022321 (2016).
- [35] R. Mohseninia, J. Yang, I. Siddiqi, A. N. Jordan, and J. Dressel, arXiv: 1907.08882 [quant-ph].
- [36] K. Kraus, A. Böhm, J. D. Dollard, and W. H. Wootters, *States, Effects, and Operations Fundamental Notions of Quantum Theory* (Springer, Berlin 1983).
- [37] L. Disi, Phys. Lett. A **129**, 419 (1988).
- [38] J. Dalibard and Y. Castin, and K. Mølmer, Phys. Rev. Lett. **68**, 580 (1992).
- [39] V. P. Belavkin, J. Multivariate Anal. **42**, 171 (1992).
- [40] H. J. Carmichael, *An Open Systems Approach to Quantum Optics* (Springer, Berlin, 1993).
- [41] H. M. Wiseman and G. J. Milburn, Phys. Rev. A **47**, 642 (1993).
- [42] A. N. Korotkov, Phys. Rev. B **60**, 5737 (1999).
- [43] J. Gambetta, A. Blais, M. Boissonneault, A. A. Houck, D. I. Schuster, and S. M. Girvin, Phys. Rev. A **77**, 012112 (2008).
- [44] A. N. Korotkov, arXiv:1111.4016.
- [45] A.N. Korotkov, Phys. Rev. A **94**, 042326 (2016).
- [46] J. Atalaya, M. Bahrami, L.P. Pryadko, and A.N. Korotkov, Phys. Rev. A **95**, 032317 (2017).
- [47] N. Katz, M. Ansmann, R. C. Bialczak, E. Lucero, R. McDermott, M. Neeley, M. Steffen, E. M. Weig, A. N. Cleland, J. M. Martinis, and A. N. Korotkov, Science **312**, 1498 (2006).
- [48] A. Palacios-Laloy, F. Mallet, F. Nguyen, P. Bertet, D. Vion, D. Esteve, and A. N. Korotkov, Nat. Phys. **6**, 442 (2010).
- [49] M. Hatridge, S. Shankar, M. Mirrahimi, F. Schackert, K. Geerlings, T. Brecht, K. M. Sliwa, B. Abdo, L. Frunzio, S. M. Girvin, R. J. Schoelkopf, and M. H. Devoret, Science **339**, 178 (2013).
- [50] K. W. Murch, S. J. Weber, C. Macklin, and I. Siddiqi, Nature (London) **502**, 211 (2013).
- [51] D. Risté, M. Dukalski, C. A. Watson, G. de Lange, M. J. Tiggelman, Ya. M. Blanter, K. W. Lehnert, R. N. Schouten, and L. DiCarlo, Nature (London) **502**, 350 (2013).
- [52] S. Hacoheh-Gourgy, L. S. Martin, E. Flurin, V. V. Ramasesh, K. B. Whaley, and I. Siddiqi, Nature (London) **538**, 491 (2016).
- [53] Q. Ficheux, S. Jezouin, Z. Leghtas, and B. Huard, Nat. Commun. **9**, 1926 (2018).
- [54] N. Roch, M.E. Schwartz, F. Motzoi, C. Macklin, R. Vijay, A.W. Eddins, A.N. Korotkov, K.B. Whaley, M. Sarovar, and I. Siddiqi, Phys. Rev. Lett. **112**, 170501 (2014).
- [55] R. Vijay, C. Macklin, D. H. Slichter, S. J. Weber, K. W. Murch, R. Naik, A. N. Korotkov, and I. Siddiqi, Nature (London) **490**, 77 (2012).
- [56] G. de Lange, D. Riste, M. J. Tiggelman, C. Eichler, L. Tornberg, G. Johansson, A. Wallraff, R. N. Schouten, and L. DiCarlo, Phys. Rev. Lett. **112**, 080501 (2014).
- [57] Z. Jiang and E. G. Rieffel, Quantum Information Processing **16**, 89 (2017).
- [58] R. Ruskov, A.N. Korotkov, and K. Molmer, Phys. Rev. Lett. **105**, 100506 (2010).
- [59] J. Atalaya, S. Hacoheh-Gourgy, L.S. Martin, I. Siddiqi, and A.N. Korotkov, npj Quantum Information **4**, 41 (2018).
- [60] A. Chantasri, J. Atalaya, S. Hacoheh-Gourgy, L.S. Martin, I. Siddiqi, and A.N. Jordan, Phys. Rev. A **97**, 012118 (2018).
- [61] J. Atalaya, S. Hacoheh-Gourgy, L.S. Martin, I. Siddiqi, and A.N. Korotkov, Phys. Rev. A **97**, 020104(R) (2018).
- [62] J. Preskill, Lecture Notes on Quantum Computation, <http://www.theory.caltech.edu/people/preskill/ph229/>.
- [63] H. Risken, *The Fokker-Planck Equation: Methods of Solution and Applications* (Springer, Berlin, 1989).
- [64] H. M. Wiseman and G. J. Milburn, *Quantum Measurement and Control* (Cambridge University Press, Cambridge, UK, 2009).
- [65] A.N. Korotkov, Phys. Rev. B **63**, 115403 (2001).
- [66] A. Tilloy, Phys. Rev. A **98**, 010104(R) (2018).
- [67] Yu Chen, D. Sank, P. O'Malley, T. White, R. Barends, B. Chiaro, J. Kelly, E. Lucero, M. Mariantoni, A. Megrant, C. Neill, A. Vainsencher, J. Wenner, Y. Yin, A. N. Cleland, and John M. Martinis, Appl. Phys. Lett. **101**, 182601 (2012).
- [68] M. Jerger, S. Poletto, P. Macha, Hübner, E. Ilichev, and A. V. Ustinov, Appl. Phys. Lett. **101**, 042604 (2012).
- [69] M. Takita, A. D. Córcoles, E. Magesan, B. Abdo, M. Brink, A. Cross, J. M. Chow, and J. M. Gambetta, Phys. Rev. Lett. **117**, 210505 (2016).
- [70] U. Vool, S. Shankar, S. O. Mundhada, N. Ofek, A. Narla, K. Sliwa, E. Zalys-Geller, Y. Liu, L. Frunzio, R. J. Schoelkopf, S. M. Girvin, and M. H. Devoret, Phys. Rev. Lett. **117**, 133601 (2016).
- [71] M. Kjaergaard, M. E. Schwartz, J. Braumüller, P. Krantz, J. I-Jan Wang, S. Gustavsson, and W. D. Oliver, Annual Reviews of Condensed Matter Physics **11**, 369-395 (2020).
- [72] Mathematica file that calculates the integrals of Eq. (D3).